Ab-initio Molecular Dynamics of Hydrogen Bonded Systems

Dissertation

in order to obtain the academic degree

Doctor rerum naturalium (Dr. rer. nat.)

of the Faculty of Natural Sciences II
of the Martin-Luther-Universität
Halle-Wittenberg

by
Christoph Allolio

born August 1, 1983 in Köln am Rhein

1. Reviewer: Prof. Dr. Daniel Sebastiani

2. Reviewer: Prof. Dr. Petra Imhof

Day of the defense: 16. 4. 2014

To my father, Bruno Allolio

Acknowledgements

I would like to acknowledge my advisor Prof. Daniel Sebastiani, who consistently supported me and has patiently answered my questions as well as contributed key advice with great clarity. I want to also thank him for his trust and his friendship. I would also like to thank my collaborators Prof. Nikolaus Ernsting and Dr. Michael Ryan Hansen for their interesting experiments and conceptual contributions. Many thanks are also due to Prof. Petra Imhof for helpful discussions. Furthermore, I would like to thank the other (ex-)members of Sebastiani group for their help and criticism. In no particular order Dr. Hossam Elgabarty, Ole Schütt, Dr. Christoph Wehmeyer, Gül Bekçioğlu, Tobias Watermann, Guo Xiangyang and Arne Scherrer. Also I would like to thank Nora Illanes for contributing calculations during her master thesis and Dr. Mohsen Sajadi for explaining his Stokes shift experiment. Special thanks go out to Dr. Thomas Michael for last minute advice.

Apart from my scientific colleagues, I would like to thank my wife Jinsouk, who has stood by me patiently for many years. I also thank my family, especially my father, who has always followed my scientific progress with great interest and practical advice and my mother who just is a great mother.

Publications

During the thesis I have co-authored a number of scientific papers. In the following, the individual responsibilities and contributions of the different authors are listed specifically for each work:

[1] C. Allolio and D. Sebastiani

Approaches to the solvation of the molecular probe N-methyl-6-quinolone in its excited state

Phys. Chem. Chem. Phys. **13**, 16395-16403, 2011

In this project, I prepared the computational setup of the molecular systems and performed all numerical quantum chemical calculations. In addition, I summarized the results and wrote the major part of the manuscript. D. Sebastiani acted as the supervisor the project, he coordinated the work and contributed to the redaction of the manuscript.

[2] X. Guo, T. Watermann, S. Keane, C. Allolio , D. Sebastiani

First Principles Calculations of NMR chemical shifts of Liquid Water at an Amorphous Silica Interface

Z. Phys. Chem. **226**, 1415-1424, 2012

For this publication, I prepared the computational setup of the amorphous silica surface, and a Bachelor student (S. Keane) performed the computational work under my supervision. The analysis was done partly by X. Guo, a first-year PhD student, under my supervision, and by myself. The manuscript of the article was prepared by X. Guo and T. Watermann and revised by myself. D. Sebastiani acted as the supervisor the project, he coordinated the work and contributed to the redaction of the manuscript.

[3] C. Allolio, D. Sebastiani

From Solvation to Spectroscopy - Electronic Structure Calculations as Virtual Experiments

Bunsen Magazin **15**, 4-11, 2013

For this review paper, I summarized the methodology and concepts of DFT molecular dynamics together with some current examples. D. Sebastiani coordinated the work and contributed to the redaction of the manuscript.

[4] C. Allolio, M. Sajadi, N. P. Ernsting, D. Sebastiani

An Ab Initio Microscope: Molecular Contributions to the Femtosecond Time-Dependent Fluorescence Shift of a Reichardt-Type Dye

Angew. Chem. Int. Ed. **52**, 1813-1816, 2013

In this project, I prepared the setup of the solvated molecule and performed all numerical molecular dynamics simulations. In addition, I performed the analysis of the numerical results and wrote the major part of the manuscript. Experimental data was provided by M. Sajadi (PhD student) who was working under the supervision of N. Ernsting. D. Sebastiani acted as the supervisor the project, he coordinated the work and contributed to the redaction of the manuscript.

[5] C. Allolio, N. Illanes, Y. S. Deshmukh, M.R. Hansen, D. Sebastiani

Hydrogen Bonding in Highly Concentrated Salt Solutions: The Case of LiI

J. Phys. Chem. B **117**, 9939-9946, 2013

In this project, I prepared the setup of the solvated ions and performed a major part of the numerical molecular dynamics simulations. Some of the molecular dynamics simulations were conducted by N. Illanes, a MSc student working under my supervision. In addition, I analyzed the trajectories and evaluated the results, and wrote the major part of the manuscript. Experimental data was provided by Y. S. Deshmukh (PhD student), who was working under the supervision of M.R. Hansen. D. Sebastiani acted as the supervisor the project, he coordinated the work and contributed to the redaction of the manuscript.

The contribution (3) contains a review of the methodological and conceptual parts of the present thesis work.

Contents

1

Introduction

During the last decades, electronic structure calculations have become an established part of the research process in chemistry and chemical physics. While in physics, theory and experiment have coexisted on an almost equal footing for a long time, theoretical chemistry got emancipated as an independent discipline only within the most recent scientific generation.

Nowadays, ready-to-use quantum chemistry software packages allow the exploration of supramolecular structures, molecular dynamics and spectroscopic properties without the need for highly specialized knowledge from the user. Such quantum chemical calculations can often be carried out on standard PC-workstations, which established them as routine tool for the interpretation of experiments, widely used in experimentally oriented groups of physical chemists or chemical physicists. A particular flavor of computational chemistry is represented by first-principles molecular dynamics simulations, which are the quantum chemical analogue of force-field-based molecular dynamics simulations and allow a realistic sampling of the phase space that is accessible to a system at a given temperature.

By this combination of the molecular dynamics technique with electronic structure theory, it has become possible to create an accurate and balanced atomistic representation of many experiments without relying on adjusted parameters. The scope of these

This introduction and the following chapters are intended to give an overview of the methodological foundations and as well as the most important practical aspects of this thesis work. Hence, several parts closely follow my review paper.(3)

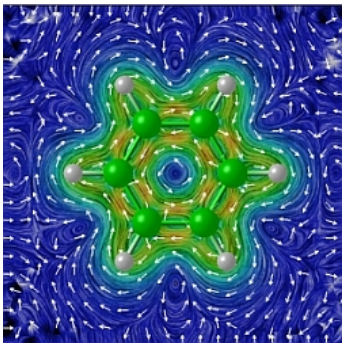

Figure 1.1: Electronic currents inside a benzene ring, induced by an external magnetic field. Image by D.Sebastiani, taken from the STM4 Gallery(22)

calculations covers the routine simulation of several hundred independent atoms (6, 7), up to a million on special occasions(8).

There is a wide variety of problems accessible by ab-initio molecular dynamics simulations. Among these are the dynamics of liquids and solvation, hydrogen bonding and diffusion. In this context, a particular strength of the ab-initio description of liquids is the accurate description of polarization, which is of crucial importance in hydrogen bonding liquids like water. One of the key properties that can be extracted is the hydrogen bonding network.(9, 10) A hydrogen bond leads to an electronic charge redistribution due to the proximity of two water molecules. Such electronic charge rearrangements are genuine quantum effects, and an approximation by means of force fields or semi-empirical calculations rarely lead to the same quantitative accuracy that a regular electronic structure calculation provides.

This has direct effects for more complex properties such as spectroscopic parameters, which react very sensitively to small geometric changes. Common spectroscopic observables include vibrational frequencies (for IR and Raman spectroscopy) (11, 12), electronic excitation energies (for UV/vis spectroscopy) (13) and magnetic fields induced by electronic ring currents caused by an external magnetic field (for NMR and EPR spectroscopy) (14, 15, 16). The structure and dynamics of water in particular have been a focus of research in the ab-initio MD community, so that the degree of reliability of the simulations is exceptionally well known.(17, 18, 19, 20, 21)

Figure 1.1 illustrates the ring currents that are induced inside a benzene molecule when an external field is applied. The plot shows the color-coded current density in

the molecular plane; interestingly, the current *inside* the molecule has the opposite orientation as the current *outside* the hexagon. Again, this phenomenon has a purely quantum nature and gives rise to subtle side-effects, such as the switch from aromatic to anti-aromatic behavior upon ionization of a molecule(23) or as a function of the symmetry of a fullerene-type molecule(24). Besides the insights into aromaticity, the computation of the response to external magnetic fields also allows the simulation of NMR spectra. The ultimate combination of electronic structure calculations and molecular dynamics simulations with the calculation of spectroscopic parameters on top of this opens a unique way for obtaining insight into otherwise inaccessible systems in the condensed phase.(25, 26)

While it has to be noted that such spectroscopic observables do *not* provide three-dimensional coordinates of atoms nor explicit information about their dynamics, they provide an indirect access to these quantities which can readily be compared to the corresponding experimental data. Molecular dynamics can then be used to map the experimental data to an atomistic description of the underlying structure and dynamics. In contrast to other methods it will also describe nonequilibrium dynamics with little additional effort. Ab-initio molecular dynamics may in addition deliver information about the electronic structure, as a form of many-body wavefunction is computed on the fly. This allows for special insight into excited state dynamics. One example is the picosecond timescale dynamic Stokes shift of a probe molecule. Experimentally the evolution of the emission wavelength of a fluorescent dye is used to monitor solvation dynamics. Ab-initio MD can simultaneously provide solute/solvent dynamics in the electronically excited state(27, 28, 29, 30), and provide the fluorescence wavelength via TD-DFT calculations. Again AIMD is unique in being able to provide the electronic strucuture and dynamical behavior of an electronically excited state. Also it is an example, where the timescale of ab-initio MD directly corresponds to experiment.

The aim of this thesis is to use first principles molecular dynamics in order to gain insight in the atomistic structure and dynamics of H-bonded systems. The systems chosen for this purpose are (solvation) water around a chromophore, aqueous solutions of lithium iodide and water confined at a hydrophilic interface. A wide array of structure and dynamics based observables was computed to present a coherent picture of the response of water to local changes in polarization, interfaces and strongly interacting solutes and provide interpretation.

1. INTRODUCTION

The thesis consists of five chapters. The first chapter is this introduction. In the next two chapters a summary of molecular dynamics and electronic structure theory is presented, with an emphasis on the key methodology used in this thesis. The fourth chapter consists of a overview over the thesis papers and a perspective on questions of wider interest. The last chapter consists of reprints of original research articles, which represent the scientific content of this cumulative dissertation.

2

Introduction to Molecular Dynamics Simulations

The classical many body problem, i.e. the motion of several interacting bodies in a potential can only be solved analytically for special cases. To simulate the time evolution of such a system, numerical methods have to be used. One of the most straightforward ways to do this is numerical integration of the (classical) equations of motion. Such an approach applied to molecules is called molecular dynamics (MD). MD simulations can be considered virtual experiments, provided that the trajectories are representative of the experimental situation. As a molecular dynamics simulation may never cover the complete phase space, one has to assume that the region in phase space, that is being sampled is representative of the whole. If this is the case, the probability distributions of observables will correspond to those obtained from statistical thermodynamics, and therefore to experiment. The exposition in this section follows the book by Tuckerman(31) while simplifying as much as possible.

2.1 Equations of motion

The best known formulation of classical mechanics are Newton's equation of motion. Newton's second law can be written in terms of an external potential $\mathbf{V}$, so that the force $\mathbf{F}_i$ on each particle i is

$$\mathbf{F}_i(t) = -\nabla_i \mathbf{V}(\{\mathbf{R}_i(t)\}) \tag{2.1}$$

Here it is assumed that the potential does not depend on the velocities of the particles, as would be the case when treating magnetic fields and induction properly. This allows for the following scheme to compute the dynamics: Beginning with a Taylor expansion of the position in time, one obtains

$$\mathbf{R}_i(t+\Delta t) \approx \mathbf{R}_i(t) + \Delta t\dot{\mathbf{R}}_i + \frac{1}{2}\Delta t^2\ddot{\mathbf{R}}_i \tag{2.2}$$

Inserting eq. 2.1 and using $\mathbf{v}_i$ for the particle velocity this becomes

$$\mathbf{R}_i(t+\Delta t) \approx \mathbf{R}_i(t) + \Delta t\mathbf{v}_i + \frac{1}{2m_i}\Delta t^2\mathbf{F}_i(t) \tag{2.3}$$

Expanding backwards in time, the equation becomes

$$\mathbf{R}_i(t-\Delta t) \approx \mathbf{R}_i(t) - \Delta t\mathbf{v}_i + \frac{1}{2m_i}\Delta t^2\mathbf{F}_i(t) \tag{2.4}$$

which allows to eliminate the velocities to obtain

$$\mathbf{R}_i(t+\Delta t) \approx 2\mathbf{R}_i(t) - \mathbf{R}_i(t-\Delta t) + \frac{1}{2m_i}\Delta t^2\mathbf{F}_i(t) \tag{2.5}$$

This is the classical Verlet algorithm(32), which has been known for about 250 years but has been periodically rediscovered since then. It incorporates the velocities implicitly by a centered difference. This also allows to compute them lateron. Eliminating the first derivative also has favorable implications on the error which scales as $\mathcal{O}(\Delta t^4)$. Starting the algorithm seems difficult at first, as at least two positions in time have to be known. But in practice for the first step one may use eq. 2.3 and take initial velocities, sampled from a Maxwell-Boltzmann distribution. The MD-codes in this work use a variety of the Verlet algorithm known as the Velocity-Verlet.(33) It is equivalent to the Verlet algorithm, but also computes velocities explicitly. The velocities are propagated as

$$\mathbf{v}_i(t+\Delta t) \approx 2\mathbf{v}_i(t) - \frac{\Delta t}{2m_i}[\mathbf{F}_i(t) + \mathbf{F}_i(t+\Delta t)] \tag{2.6}$$

This allows to use 2.3 to propagate the trajectory. The verlet integrators fulfill a number of important properties, which make them well suited for the numerical propagation of the classical equations of motion. These are

1. Good error scaling with the timestep (local scaling, $\mathcal{O}(\Delta t^4)$, integrated $\mathcal{O}(t_N^2\Delta t^2)$)

2. Time reversibility

3. Conservation of a shadow Hamiltonian

The conservation of an approximate, "shadow" Hamiltonian, which approaches the true Hamiltonian as $\Delta t \to 0$ results in improved momentum and energy conservation.

2.2 Temperature coupling

To make experiments reproducible, they are conducted at specific conditions, e.g. fixed temperature and pressure. A defined temperature is imposed by exchange with a heat bath. The same has to be done for molecular dynamics simulations, where this situation corresponds to the so called canonical ensemble. While the correct temperature and distribution can be imposed a priori on the kinetic energy of the system, this is not easily possible for the distribution of the potential energy, which depends on the positions in the system in a nontrivial way. Also, the fluctuations in a sufficiently small system depend on whether energy exchange with the environment is permitted or not. If no exchange is permitted, the system is in the microcanonical ensemble. Its dynamics are described by the following Hamiltonian:

$$\mathcal{H} = \sum_i \frac{\mathbf{p_i^2}}{2m_i} + \mathbf{V}(\{\mathbf{R}_i(t)\}) \tag{2.7}$$

Energy exchange with the environment cannot be easily integrated into a Hamiltonian formalism, as the energy of the system is no longer conserved due to the interactions with the heat bath. In the Nosé approach(34), the system's Hamiltonian is extended by a fictitious degree of freedom, which is included into the kinetic energy of all other degrees of freedom, in order to scale them to the appropriate temperature. This fictitious degree s and its momentum p_s, plus coupling parameter Q (the dimension of Q is energy x time^2) are introduced in the system Hamiltonian as follows:

$$\mathcal{H}_{Nose} = \sum_i \frac{\mathbf{p_i^2}}{2m_i s^2} + \mathbf{V}(\{\mathbf{R}_i(t)\}) + \frac{p_s^2}{2Q} + gkT \ln s \tag{2.8}$$

Here g is equal the number of spatial degrees of freedom in the system ($3N$) plus one for s. The parameters k and T are the Boltzmann constant and the temperature. Note that $3NkT$ is the average kinetic energy for a system of N particles in the canonical

ensemble. It can be shown(31), that fluctuations in the microcanonical ensemble of the Nosé Hamiltonian become equivalent to those of the canonical ensemble of the original system. In this fashion canonical sampling can be accomplished in a deterministic way. From the Hamiltonian one obtains the Nosé equations of motion:

$$\dot{\mathbf{p}}_i = \mathbf{F}_i \tag{2.9}$$

$$\dot{\mathbf{R}}_i = \frac{\mathbf{p}_i}{m_i s^2} \tag{2.10}$$

$$\dot{s} = \frac{p_s}{Q} \tag{2.11}$$

$$\dot{p}_s = \sum_i \frac{\mathbf{p}_i}{m_i s^3} - \frac{gkT}{s} \tag{2.12}$$

Introducing the following noncanonical change of variables transforms the system into a non-Hamiltonian one.(35)

$$\mathbf{p}'_i = \frac{\mathbf{p}_i}{s} \tag{2.13}$$

$$dt' = \frac{dt}{s} \tag{2.14}$$

$$\frac{1}{s}\frac{ds}{dt'} = \frac{\eta}{dt'} \tag{2.15}$$

$$p_s = p_\eta \tag{2.16}$$

Applying these substitutions, changing the definition of g to be dN (the dimension d times the number of nuclei N) and rederiving the equations of motion, one obtains

$$\dot{\mathbf{R}}_i = \frac{\mathbf{p}_i}{m_i} \tag{2.17}$$

$$\dot{\mathbf{p}}_i = \mathbf{F}_i - \frac{p_\eta}{Q}\mathbf{p}_i \tag{2.18}$$

$$\dot{\eta} = \frac{p_\eta}{Q} \tag{2.19}$$

$$\dot{p_\eta} = \sum_i \frac{\mathbf{p}_i^2}{m_i} - gkT \tag{2.20}$$

Writing the Nosé-Hoover equation this way allows important intuitive insight. Looking at eq. 2.18 one sees that the acceleration is modified by a friction term depending on p_η. The definition in eq. 2.20 shows, that this friction evolves with the difference of the kinetic energy and its canonical average. So it becomes clear how the friction term in all momenta "thermostats" the system to a given temparature and also controls its fluctuations. It is well known that a single Nosé-Hoover degree of freedom may lead to nonergodic behavior, as the conservation law introduces restrictions on the phase space. This can be especially severe for a small system, such as a single harmonic oscillator.(36) More degrees of freedom have to be reintroduced, this is usually done by a chain of Nosé-Hoover thermostats. This means coupling the variable p_η to another Nosé-Hoover thermostat, and coupling this thermostat's p_η again to obtain a chain of thermostats. In practice a chain length of five is usually sufficient. For an in depth discussion of statistical thermodynamics and ensembles in the context of molecular dynamics, see the excellent book by Tuckerman.(31)

3

Concepts of Electronic Structure Theory

3.1 Preliminaries

All equations are given in atomic units, except where denoted otherwise. Letters in bold denote vector quantities. Variables in curly brackets represent an ensemble of particles. Specifically, $\mathbf{r}$ is used for electronic coordinates and $\mathbf{R}$ is used for nuclear coordinates. The three dimensional electron density is denoted ρ. A one-particle wavefunction is represented by φ and any basis function by χ. The many-body time-dependent wave function including the nuclear degrees of freedom is called Φ and the many-body electronic wavefunctions are called Ψ.

3.2 The Schrödinger equation

The equation of motion for a nonrelativistic quantum mechanical system may be written as the time-dependent Schrödinger equation

$$i\frac{\partial}{\partial t}\Phi(\{\mathbf{r_i}\},\{\mathbf{R_I}\},t) = \hat{H}\Phi(\{\mathbf{r_i}\},\{\mathbf{R_I}\},t) \tag{3.1}$$

The systems of interest to theoretical chemistry are usually molecular systems consisting of nuclei and electrons. We distinguish between the set of core coordinates $\{\mathbf{R}_I\}$ and the set of electron coordinates $\{\mathbf{r}_i\}$. Following this nomenclature the Hamilton operator $\hat{H}$ is written as

$$\hat{H} = -\sum_I \frac{1}{2M_I}\nabla_I{}^2 - \underbrace{\sum_i \frac{1}{2}\nabla_i{}^2 + \sum_{i<j}\frac{1}{|\mathbf{r}_i - \mathbf{r}_j|} + \sum_{i,I}\frac{Z_I}{|\mathbf{R}_I - \mathbf{r}_i|} + \sum_{I<J}\frac{Z_I Z_J}{|\mathbf{R}_I - \mathbf{R}_J|}}_{\hat{H}_e} \quad (3.2)$$

This includes only the Coulomb interactions of electrons and nuclei, and thus uses a classical electric field. Without the atomic core kinetic energy it is the electronic Hamiltonian $\hat{H}_e$. The next important approximation is to separate electronic and nuclear degrees of freedom.

3.3 The Born-Oppenheimer approximation

This section follows the treatment in the corresponding chapter in the book by Marx and Hutter.(37) Let us begin by assuming that for each possible set of positions of the nuclei, the stationary problem has been solved;

$$\hat{H}_e(\{\mathbf{r}_i\};\{\mathbf{R}_I\})\Psi_k(\{\mathbf{r}_i\};\{\mathbf{R}_I\}) = E_k(\{\mathbf{R}_I\})\Psi_k(\{\mathbf{r}_i\};\{\mathbf{R}_I\}) \quad (3.3)$$

which has the fixed positions $\{\mathbf{R}_I\}$ parametrically included in the electronic Hamiltonian $\hat{H}_e$, see eq. 3.2. The above equation is called the electronic Schrödinger equation. The spectrum of $\hat{H}_e$ is taken to be discrete and its eigenfunctions Ψ_k are orthonormalized. The total wavefunction can then be expanded as

$$\Phi(\{\mathbf{r_i}\},\{\mathbf{R_I}\};t) = \sum_{l=0}^{\infty}\Psi_l(\{\mathbf{r_i}\};\{\mathbf{R_I}\})\chi_l(\{\mathbf{R_I}\};t) \quad (3.4)$$

Inserting this into the time-dependent Schrödinger equation, multiplying from the left by $\Psi_k(\{\mathbf{r_i}\};\{\mathbf{R_I}\})$ and integrating over all electronic coordinates leads to a set of coupled differential equations, so that for each $\mathbf{r}$ from $\{\mathbf{r}_i\}$:

$$\Big[-\sum_I \frac{1}{2M_I}\nabla_I^2 + E_k(\{\mathbf{R_I}\})\Big]\chi_k + \sum_l \mathcal{C}_{kl}\chi_l = i\frac{\partial}{\partial t}\chi_k \quad (3.5)$$

Where $\mathcal{C}_{kl}$ is the nonadiabatic coupling operator, its definition is

$$\mathcal{C}_{kl} = \int \Psi_k^*\Big[-\sum_I \frac{1}{2M_I}\nabla_I^2\Big]\Psi_l d\mathbf{r} + \frac{1}{M_I}\sum_I\Big(\int \Psi_k^*[-i\nabla_I]\Psi_l d\mathbf{r}\Big)[-i\nabla_I] \quad (3.6)$$

Nonadiabatic coupling is the coupling between different eigenstates Ψ_k of the electronic Hamiltonian, induced by nuclear motion. The second part of eq. 3.6 is dependent on the nuclear momentum, in the case of a real wavefunction it will vanish. If one takes only the diagonal terms $\mathcal{C}_{kk}$ of the problem into account, the adiabatic approximation is obtained. Within the adiabatic approximation eq. 3.5 is decoupled, this corresponds to the exclusion of switching quantum states during the time evolution of electronic state k. Correspondingly, if the complete wave function of the system Φ contains only one electronic eigenstate, it may be written as a direct product of an electronic and a nuclear function.

$$\Phi(\{\mathbf{r}_i\},\{\mathbf{R}_I\},t) \approx \Psi_k(\{\mathbf{r}_i\};\{\mathbf{R}_I\})\chi_k(\{\mathbf{R}_I\},t) \tag{3.7}$$

This approximation is widely used in electronic structure theory and becomes problematic when treating excited states in particular, as in excited state dynamics electronic states can become quite close at certain sets of coordinates $\{\mathbf{R}_I\}$ and thus coupling cannot be neglected anymore. Such a situation is commonly referred to as a conical intersection. However, also the diagonal coupling term is often neglected, thus:

$$\Big[-\sum_I \frac{1}{2M_I}\nabla_I^2 + E_k(\{\mathbf{R}_I\})\Big]\chi_k = i\frac{\partial}{\partial t}\chi_k \tag{3.8}$$

Which constitutes the "Born-Oppenheimer approximation", as opposed to the full adiabatic approximation defined above, eq. 3.7. Regarding the electronic wavefunction Ψ_k as decoupled from the nuclear wavefunction can also be empirically motivated, because the (dielectric) spectra of molecular systems have regions where electronic degrees of freedom are dominant in the response as well as regions, which correspond to almost purely nuclear motion, so there is often a sufficient separation of energies to justify the decoupling. The origin for the lack of coupling is the mass difference of electrons and nuclei and its effect on the inertia. In this discussion spin was neglected.

3.4 The Hartree-Fock method

The electronic structure problem is the solution of the stationary Schrödinger equation 3.3 for one set of coordinates $\{\mathbf{R}_I\}$. It will now be rewritten in the Dirac notation, while omitting this parametric dependency on the nuclei for clarity.

$$\hat{H}_e(\{\mathbf{r}_i\})|\Psi_k(\{\mathbf{r}_i\})\rangle = E_k|\Psi_k(\{\mathbf{r}_i\})\rangle \tag{3.9}$$

In principle, this expression represents a regular eigenvalue problem for the wavefunction with a known Hamiltonian $\hat{H}_e$. However, the interaction of the individual electrons leads to an intrinsic complexity of this equation that is so large that a straightforward numerical solution exceeds any computational ressources available today and in the foreseeable future. An easy way to see this is to remember that even a real, spinless Ψ_k on a cartesian grid of 100 points in $\mathbf{r}_i$ is an object of dimension 100^{3n}, n being the number of electrons. Just storing it in this form would exceed the capabilities of modern computers for but the most simple systems. A large part of the theoretical chemistry community is thus developing efficient and accurate approaches that lead to useful results for the electronic wavefunction. The majority of existing methods starts with the approximation that every electron can be seen as mainly independent from all the others, yielding a description by a set of individual single-electron orbitals φ_i. This approximation is introduced by writing Ψ_k as an antisymmetrized product - or a Slater determinant, which is the solution of eq. 3.9 for a system of noninteracting electrons, i.e. a system without the electron-electron terms in $\hat{H}_e$:

$$\Psi_k(\{\mathbf{r}_i\}) = \frac{1}{\sqrt{n!}} \begin{vmatrix} \varphi_1(\mathbf{r}_1, s_1) & \varphi_2(\mathbf{r}_1, s_1) & \dots & \varphi_n(\mathbf{r}_1, s_1) \\ \varphi_1(\mathbf{r}_2, s_2) & \varphi_2(\mathbf{r}_2, s_2) & \dots & \varphi_n(\mathbf{r}_2, s_2) \\ \dots & \dots & & \dots \\ \varphi_1(\mathbf{r}_n, s_n) & \varphi_2(\mathbf{r}_n, s_n) & \dots & \varphi_n(\mathbf{r}_n, s_n) \end{vmatrix} \tag{3.10}$$

By this approach also the dimensionality is drastically reduced, as Ψ_k reduces to an antisymmetrized product of one particle functions. One would thus have to only store only $n \cdot 100^3$ spatial points. The coordinates s_n are spin coordinates, reflecting the spin states of the electrons. These single-particle functions are comparably easy to obtain numerically: If one uses a 3.10 type ansatz for the full electronic structure problem and applies the variational principle under an orthonormality constraint for the different φ_i, one obtains the Hartree-Fock equations, which allow to determine φ_i with relative ease. Through the ansatz and a follow on unitary transformation the electronic structure problem becomes a set of one-particle Schrödinger equations

$$\hat{f}\varphi_i = \epsilon_i \varphi_i \tag{3.11}$$

With $\hat{f}$ as the one particle Fock-operator and φ_i as canonical orbitals.

$$\hat{f}\varphi_i = \big(\underbrace{-\frac{1}{2}\nabla^2 + \nu_{ext}}_{\hat{h}} + \hat{j} - \hat{k}\big)\varphi_i \tag{3.12}$$

These one particle equations describe the interactions of the electrons via an averaged interaction with the other φ_i. The corresponding operators of this interaction are $\hat{j}$ and $\hat{k}$ respectively. In order to simplify the exposition, only the closed shell case is presented here. The closed shell case is distinguished by an even number of electrons, two of which are of opposite spin and occupy one spatial orbital. The spin component in the φ_i may then be eliminated, so that the functions of interest are now $\varphi_i(\mathbf{r})$. The definition of $\hat{j}$ and $\hat{k}$ then becomes

$$\hat{j}(\mathbf{r})\varphi_i(\mathbf{r}) = 2\sum_{k=1}^{n/2}\int \varphi_k^*(\mathbf{r}')\varphi_k(\mathbf{r}')\frac{1}{|\mathbf{r}-\mathbf{r}'|}\varphi_i(\mathbf{r})d\mathbf{r}' \tag{3.13}$$

where the summation over the orbitals goes up to half the number of electrons. One can immediately see the classical analogue by recognizing $\varphi_k^*(\mathbf{r}')\varphi_k(\mathbf{r}')$ as the one particle density $\rho_k(\mathbf{r}')$ of $\varphi_k(\mathbf{r}')$. This allows to write the operator as a potential operator, the so called Hartree potential $\nu_H(\mathbf{r})$. The Hartree potential represents the classical electrostatic interaction of the electronic densities, i.e. the mean-field.

$$\hat{k}(\mathbf{r})\varphi_i(\mathbf{r}) = \sum_{k=1}^{n/2}\int \varphi_k^*(\mathbf{r}')\varphi_i(\mathbf{r}')\frac{1}{|\mathbf{r}-\mathbf{r}'|}\varphi_k(\mathbf{r})d\mathbf{r}' \tag{3.14}$$

The exchange operator $\hat{k}$ is marked by the exchange of a coordinate in eq. 3.14 and can not be written as a sum of one particle densities. It arises due to the antisymmetrized nature of the ansatz 3.10. The full Hartree-Fock energy of Ψ_k is not equal to simply the (twice) the sum of ϵ_i, the "orbital energies" of the previously defined one particle operator, due to the double counting of mean field interactions. Instead, the energy of the full HF wavefunction Ψ_{HF} can be written as

$$E_{HF} = 2\sum_{k=1}^{n/2} H_k + \sum_{k=1,l=1}^{n/2} 2J_{kl} - K_{kl} \tag{3.15}$$

Its components in terms of the orbitals are defined as

$$H_k = 2\sum_{k=1}^{n/2}\langle\varphi_k|\hat{h}(\mathbf{r}_k)|\varphi_k\rangle \tag{3.16}$$

which is a sum of the one kinetic and external potential energy parts of eq. 3.12

$$J_{kl} = \langle\varphi_k\varphi_l|\frac{1}{|\mathbf{r}_k - \mathbf{r}_l|}|\varphi_l\varphi_k\rangle \tag{3.17}$$

which is the classical electrostatic density interaction between ρ_k and ρ_l obtained by integration over space, a so-called Coulomb integral. The exchange analogue, i.e. the exchange integral has permutated coordinates and can be written as

$$K_{kl} = \langle\varphi_k\varphi_l|\frac{1}{|\mathbf{r}_k - \mathbf{r}_l|}|\varphi_k\varphi_l\rangle \tag{3.18}$$

The difference of the Hartree-Fock energy to the true energy is defined as the correlation energy. It contains the neglected part of the physically correct interaction. It has to be re-introduced later on by means of specific methods. In classical quantum chemistry it is introduced by a step-wise procedure (Møller-Plesset perturbation theory or configuration-interaction/coupled-cluster approaches, see reviews (38, 39)). In practice these theories rely on an expansion of Ψ_k in several determinants of the form 3.10. An elegant approach to circumvent these expansions and the associated numerical heavy lifting is density functional theory. Both these principles lead to an accurate description of the ensemble of electronic properties for molecules, liquids and solids; their theoretical details are discussed in numerous review articles and books (6, 40, 41, 42, 43, 44, 45, 46, 47).

3.5 Density functional theory

Density functional theory (DFT), is in principle an exact theory. In practice an effective potential (the exchange-correlation potential) is optimized such as to represent the actual many-electron interactions as good as possible. This section gives an introduction to the fundamentals of DFT.

3.5.1 The Hohenberg-Kohn theorems

Hohenberg and Kohn were able to prove that instead of finding the solution for the 3N dimensional electronic Schrödinger equation, it is equally sufficient to determine the correct electron density ρ.(48) They proved the following theorem:

> **HK I**: For systems with a nondegenerate ground state, the ground state wave function $\Psi_0(\{\mathbf{r_i}\})$ and thus all properties that are based on the electronic structure are uniquely determined by the ground state electronic density $\rho_0(\mathbf{r})$.

To proof begins with the energy of the ground state $|\Psi_0\rangle$.

$$E = \langle\Psi_0|\hat{H}|\Psi_0\rangle = \int \nu(\mathbf{r})\rho_0(\mathbf{r})d\mathbf{r} + \langle\Psi_0|\hat{T} + \hat{V}_{ee}|\Psi_0\rangle \tag{3.19}$$

The potential $\nu(\mathbf{r})$ is an external potential, such as the potential of the nuclei in eq. 3.12. The operators $\hat{T}$ and $\hat{V}_{ee}$ correspond to the (electron) kinetic energy and electron-electron interaction operators as defined in eq. 3.2. The form of these latter operators depends only on the number of electrons in the system. This number is also defined as the integral of the density over all of space. The proof of **HK I** depends on showing, that for two different $\nu(\mathbf{r}) \neq \nu'(\mathbf{r})[+const]$ a different $\rho_0(\mathbf{r})$ is necessarily obtained. The potential $\nu'(\mathbf{r})$ has a different ground state wavefunction $\Psi_0'(\{\mathbf{r_i}\})$. Assuming it has the same density as $\Psi_0(\{\mathbf{r_i}\})$ its energy expectation value is:

$$E' = \langle\Psi_0'|\hat{H}'|\Psi_0'\rangle = \int \nu'(\mathbf{r})\rho_0(\mathbf{r})d\mathbf{r} + \langle\Psi_0'|\hat{T} + \hat{V}_{ee}|\Psi_0'\rangle \tag{3.20}$$

According to the variational principle, the nondegenerate energy expectation value is always above the one of the corresponding ground state wavefunction.

$$E < \langle\Psi_0'|\hat{H}|\Psi_0'\rangle = E' + \int [\nu(\mathbf{r}) - \nu'(\mathbf{r})]\rho_0(\mathbf{r})d\mathbf{r} \tag{3.21}$$

Equation 3.21 may also be written for Ψ_0:

$$E' < \langle\Psi_0|\hat{H}'|\Psi_0\rangle = E + \int [\nu'(\mathbf{r}) - \nu(\mathbf{r})]\rho_0(\mathbf{r})d\mathbf{r} \tag{3.22}$$

If eq. 3.21 and eq. 3.22 are added, the following contradiction appears:

$$E' + E < E' + E \tag{3.23}$$

Thus proving **HK I** by reductio ad absurdum. □

The density of the electronic ground state can therefore be mapped to the ground state wavefunction; energy and all other ground state electronic properties may be accordingly obtained from it. The ground state electron density itself may in turn be obtained variationally, i.e. by finding the density corresponding to the lowest energy, as is contained in the second Hohenberg-Kohn theorem.

HK II: For each trial density ρ' which satisfies
$\int \rho'(\mathbf{r})d\mathbf{r} = n$ and
$\rho'(\mathbf{r}) \geq 0$ for all $\mathbf{r}$ the following equality holds

$$E_0 = E_\nu[\rho_0] \leq E_\nu[\rho']$$

It is therefore sufficient to find a way to map the density, a three dimensional function, to the energy E_ν , which is a scalar. This is what is called a density functional. The proof of **HK II** relies on the variational principle and **HK I**. We define a trial wavefunction Ψ'_0, associated to a trial density ρ' and its corresponding potential ν'. Its energy

$$\langle \Psi'_0 | \hat{H} | \Psi'_0 \rangle \geq E_0 = E_\nu[\rho] \tag{3.24}$$

is larger than the energy corresponding to the ground state density ρ_0 of ν. □

An important limitation of the trial densities ρ' is already apparent. They have to be associated to a potential ν' (v-representability). However, it is possible to circumvent this need by using the Levy-Lieb constrained search formalism.(49, 50) The real density must also be representable by an antisymmetrized wavefunction function (n-representability), which can also be assured. In order to apply density functional theory, it is now necessary to find a way of mapping energies to densities, preferably without any recourse to a wavefunction. This is a very challenging task, as to maintain the exactness of the theory the density functional $E_\nu[\rho]$ has to account for the full many-body interactions.

3.5.2 The Kohn-Sham formalism

Nevertheless, in the Kohn-Sham approach(51), as a starting point for this functional, one begins with a fictitious noninteracting system, introducing HF-like orbitals to generate the density and compute the kinetic energy. The orbitals are reintroduced, because it is not clear how to compute the kinetic energy of a density, as it depends on the Laplacian of the wavefunction. The density functional $E[\rho]$ is therefore decomposed to

$$E[\rho] = T_s[\{\varphi_i\}] + J[\rho] + E_{XC}[\rho] + V_{ext}[\rho] \tag{3.25}$$

Hence, it consists of the kinetic energy of the noninteracting system T_s, the (classical electrostatic) Hartree energy J, the exchange-correlation energy E_{XC}, and the energy due to the potential of the nuclei V_{ext}. The exchange-correlation (XC) functional $E_{XC}[\rho]$ is defined to contain the energy difference to the fully interacting, correlated system. The XC functional is written in terms of a potential for a single-electron.

$$\nu_{XC} \equiv \frac{\delta E_{XC}[\rho]}{\delta \rho} \tag{3.26}$$

Where the right part of the equation is a functional derivative of E_{XC} with respect to ρ. This leads to the Kohn-Sham equations. In analogy to eq. 3.12, a set of single particle equations is obtained. However, with a slightly different Hamilton operator:

$$\hat{h} = -\frac{1}{2}\nabla^2 + \nu_{ext}(\mathbf{r}) + \nu_H(\mathbf{r}) + \nu_{XC}(\mathbf{r}) \tag{3.27}$$

Where the Hartree potential ν_H is equal to the Coulomb operator $\hat{j}$ as defined as in eq. 3.13. The exchange operator $\hat{k}$ is defined to be included in ν_{XC}. The single electron XC-potential thus turns a mean-field, HF-type calculation into an exact one. In fact computational effort is reduced to a mere Hartree approximation as the energetic effect of anti-symmetry, i.e. exchange is also included in the multiplicative operator ν_{XC}. So far the theory is still exact, the only price paid is the replacement of the true Ψ_0 with a fictitious noninteracting system. The true wavefunction of the system is not directly available anymore. This change leads to some further changes which are not at first evident from the formalism.

As the fictitious noninteracting system does not deliver the true wavefunction, only the properties of Ψ_{KS} depending on ρ alone (i.e.) J and the physical external potential can be taken directly from the φ_i. Specifically,

$$T[\rho] \neq T_s[\rho] \tag{3.28}$$

The exchange-correlation functional therefore does not only include the exchange energy and electron correlation as derived from the HF picture, but also a correction to the kinetic energy of the noninteracting system $T_s[\rho]$. It can therefore be written approximately as

$$E_{XC}[\rho] = T[\rho] - T_s[\rho] + V_{ee}[\rho] - J[\rho] \tag{3.29}$$

Where V_{ee} is the full electronic interaction energy. Furthermore, the background density used in evaluating $J[\rho]$ also includes $\rho[\varphi_i]$, i.e. for $k = i$ in eq. 3.13. In HF-calculations this poses no problem as this is offset by subtraction of the self exchange in eq. 3.14. However, in KS-DFT this also has to be accounted for in $E_{XC}[\rho]$. This phenomenon is called self interaction.
A direct way to calculate $E_{XC}[\rho]$, without first solving the Schrödinger equation is unknown - finding it is equivalent to solving the quantum many-body problem for the ground state.

3.5.3 Density functionals for exchange and correlation energy

Looking for approximations to the XC-functional, Kohn and Sham turned to the the homogeneous electron gas (HEG). The HEG is a system of uniform electron density with corresponding uniform background charge. The idea to use the homogeneous electron gas to compute energies goes back to Thomas and Fermi.(52, 53) As HEGs of arbitary densities can be constructed, they are very useful for DFT approximations.

Local density approximation

The most straightforward way to incorporate the HEG into the Kohn-Sham model, is to assume that the contribution of the density $\rho(\mathbf{r})$ to $E_{XC}[\rho]$ on some volume slice $\mathbf{r_0} + d\mathbf{r}$ with density ρ_0 corresponds to the the same quantity of an HEG of density ρ_0. As it takes into account only the local density and not the variation in its environment, it is called the local density approximation (LDA). This makes it possible to write

$$E_{XC}^{LDA}[\rho] = \int \rho(\mathbf{r}) \epsilon_{XC}^{hom}(\rho(\mathbf{r})) d\mathbf{r} \tag{3.30}$$

In order to obtain $\nu_{XC}^{LDA}(\mathbf{r})$ from it, the functional derivative of $E_{XC}^{LDA}[\rho]$ as in eq. 3.26 is used, so that

$$\nu_{XC}^{LDA}(\mathbf{r}) = \epsilon_{XC}^{hom}(\rho(\mathbf{r})) + \rho(\mathbf{r})\frac{\delta\epsilon_{XC}^{hom}(\rho(\mathbf{r}))}{\delta\rho(\mathbf{r})} \tag{3.31}$$

It can be shown that it is possible to separate ϵ_{XC} into exchange and correlation dependent parts.

$$\epsilon_{XC}(\rho(\mathbf{r})) = \epsilon_X(\rho(\mathbf{r})) + \epsilon_C(\rho(\mathbf{r})) \tag{3.32}$$

The exchange energy of a HEG of density $\rho(\mathbf{r})$ is known analytically.(54)

$$E_X[\rho] = \int \rho(\mathbf{r})\epsilon_X^{hom}(\rho(\mathbf{r}))d\mathbf{r} = -\frac{3}{4}(\frac{3}{\pi})^{1/3}\int \rho(\mathbf{r})^{4/3}d\mathbf{r} \tag{3.33}$$

where

$$\epsilon_X^{hom}(\rho(\mathbf{r})) = -\frac{3}{4}(\frac{3}{\pi})^{1/3}\int \rho(\mathbf{r})^{4/3}d\mathbf{r} \tag{3.34}$$

is the exchange energy density. One can numerically compute and interpolate the correlation energy of the HEG as a function of its density.(55, 56)

In principle the result should be far from exact, as the exchange and correlation energies of a real system do not necessarily correspond to those assembled from densities of the HEG model system. The change in kinetic energy due to correlation ΔT_s is not accounted for, neither is the self interaction problem. One would expect that this method only gives good results for systems of slowly varying electronic density. However it turns out, that it actually works reasonably well for a large number of molecular systems.(57) Some problems inherent to the LDA may be assessed by looking at the exchange (eq. 3.34) of an exponentially decaying density, in this case

$$\rho(\mathbf{r}) \propto e^{-\alpha r} \rightarrow \nu_X^{LDA}(\mathbf{r}) \propto e^{-\alpha r/3} \tag{3.35}$$

However, the exact exchange potential derived from the HF exchange energy may be shown to asymptotically behave as

$$\nu_X^{exact}(\mathbf{r}) \rightarrow -\frac{e^2}{|\mathbf{r}|} \tag{3.36}$$

In a finite system, such as an atom, this wrong asymptotic behavior leads to a flawed description of states with Coulombic ($\frac{1}{r}$) behavior. One consequence is that atomic negative ions are predicted to be unbound. This also does not bode well for eventual descriptions of excited states.

(Generalized) gradient approximation

To improve the description for more rapidly varying densities (as present in most molecular systems), it is desirable to find an approximate exchange-correlation functional which also includes variations in the densities (local) environment. By including the gradient of the electron density into ϵ_{XC} one may write

$$E_{XC}[\rho] = \int \epsilon_{XC}(\rho(\mathbf{r}), \nabla\rho(\mathbf{r}))d\mathbf{r} \tag{3.37}$$

To introduce gradient information on may expand the energy in a gradient expansion and include $\nabla\rho^2$ terms. Charge conservation of the so called exchange-correlation hole then becomes an issue. For further information, see (40, 47, 57). Realizing this and ensuring proper behavior of the XC-hole brought about the generalized gradient approximation (GGA).(58) In contrast to LDA, there have been many different approaches to the GGA exchange functional. For example the commonly used Becke88(59) exchange functional has been parametrized using a test set. Another widespread functional is the Lee-Yang-Parr (LYP) correlation functional.(60) Combinations of exchange and correlation functionals in the literature have been expressed by combining the abbreviations for exchange and correlation functionals, e.g. BLYP or BP86(61).

More sophisticated approaches

As a logical next step from the GGA, the Laplacian of the density can also be taken into account (MGGA).(62) One may also compute an exchange energy from the KS orbitals (EXX) and only take the correlation energy from the local density. Approaches may be combined, taking e.g. a fraction of HF-exchange, some LDA and some GGA exchange and correlation energies, as in so called hybrid functionals.(63) The commonly used B3LYP functional is a result of such a combination parametrized against a test set. In addition to this one may correct for the self interaction error (SIC)(64), kinetic energy density and other problems according to the task at hand. One especially active

research area has been dispersion corrections to DFT.(65, 66) While no single method "just works" in any chemical environment, some variant of DFT has been successfully applied in nearly all areas of chemistry and chemical physics.(40) For a more in depth introduction, see e.g. the second half of the book by Koch and Holthausen.(57)

3.6 Basis sets

Wavefunction based methods, such as the HF theory, do need to express this many-body wavefunction in some basis. In Kohn-Sham DFT, the electron density is generated from orbital densities. Instead of simply optimizing a free form function on a spatial grid, i.e. using the position basis, the orbitals are built from linear combinations of specially adapted functions.

$$\varphi_i(\mathbf{r}) = \sum_{\mu} C_{\mu i} \chi_{\mu i}(\mathbf{r}) \tag{3.38}$$

These basis functions χ may be derived from atomic orbitals, obtained e.g. by solving the Schrödinger equation for the hydrogen atom. Hence, a so called Slater Type Orbital (STO) has the form

$$\chi(r, \theta, \phi) = A r^{n-1} e^{-\zeta r} Y_{lm}(\theta, \phi) \tag{3.39}$$

The radial part of the solutions for the hydrogen atom contains an exponentially decaying part as well as a polynomial.

3.6.1 Gaussian type orbitals

The exponential part is inconvenient from a numerical point of view, as integrals e.g of the type in eq. 3.13 are not easily evaluated. Therefore, typically Gaussian type functions (GTFs), also abbreviated as GTOs (Gaussian type orbitals) are chosen for this purpose, as integrals over products of differently centered Gaussians may be easily evaluated using the Gaussian product rule. A single Gaussian does not accurately reproduce the sharp cusp at the center of an exponential, neither does it have the correct asymptotic decay. However, using linear combinations of Gaussians one may approximate atomic orbitals. Linear combinations of Gaussian functions with fixed

coefficients may be used as one atomic orbital type basis function. This is referred to as a contracted GTO (CGTO). In this case

$$\chi(r,\theta,\phi) = Y_{lm}(\theta,\phi)r^l \sum_i \alpha_i A_i(l,\alpha)e^{-\zeta_i r^2} \tag{3.40}$$

Where the coefficients c_i and the exponents ζ_i predetermined in order to optimally fit atomic orbitals. Instead of spherical coordinates, the GTOs may also be expressed in cartesian coordinates. Atomic orbital type basis functions, such as GTOs have localized centers in real space.

3.6.2 Plane waves

Another basis especially suited for periodic systems are plane waves. These are by nature periodic and localized in reciprocal space.

$$\chi_G(\mathbf{r}) = Ae^{i\mathbf{G}\cdot\mathbf{r}} \tag{3.41}$$

The normalization factor A is given by $\frac{1}{\sqrt{\Omega}}$ with Ω as the volume of the unit cell. In a three dimensional lattice, $\mathbf{G}$ contains the reciprocal lattice vectors. The periodicity of the plane waves is especially advantageous in the domain of solid state physics, where crystal periodicity enforces periodic wavefunctions. According to the Bloch theorem(67), the wavefunctions of a particle in a periodic potential will have the form of

$$\psi_{n\mathbf{k}}(\mathbf{r}) = e^{[i\mathbf{k}\cdot\mathbf{r}]}\mathbf{u}_{n\mathbf{k}}(\mathbf{r}) \tag{3.42}$$

Where $\mathbf{u}$ has the same periodicity as the potential, e.g. the crystal unit cell. The different wavevectors $\mathbf{k}$ are quantum numbers with discrete energy levels ϵ_k. They correspond to a wavefunction phase factor with a different periodicity than the unit cell itself, e.g. several multiples of a unit cell. Finding all $\mathbf{k}$ in the first Brillouin zone of the crystal will give the band structure. In the case of a metallic system these conduction bands have nonzero occupation, hence an electron can move freely over several unit cells. When treating insulators, as is the case in this thesis, it is sufficient to consider the electronic 0 K ground state at $\mathbf{k} = 0$. This is called the Γ-point approximation. In the following sections, the $\mathbf{k}$ dependency will be omitted for the sake of simplicity.

The plane waves (PW) form a complete basis - the momentum basis for a particular periodic system. As they are not localized in real but in reciprocal space, they avoid some problems of atom centered basis sets (see below). The Kohn-Sham orbitals are expressed in PW as follows

$$\varphi_i(\mathbf{r}) = \frac{1}{\sqrt{\Omega}} \sum_{\mathbf{G}} C_{i,\mathbf{G}} e^{[i\mathbf{G}\cdot\mathbf{r}]} \tag{3.43}$$

As in practice the basis set expansion is cut off at some point, the basis is incomplete which leads to certain systematic errors. When using GTOs, errors arise from the position dependence of the basis functions, leading to effects dependent on the relative positions of nuclei to each other. One example for this is the basis set superposition error (BSSE). Another are the Pulay forces. The use of plane waves avoids these problems, as the basis is dependent on the unit cell $\mathbf{G}$ and not the atomic positions. However, the energy may instead unphysically depend on the position of a molecule in the periodic box because of the finite grid resolution. When using PW, the basis set cutoff is usually given in terms of the kinetic energy. This kinetic energy corresponds to the energy of the free particle whose wavefunction is χ_G, e.g. 280 Ry. As the reciprocal unit cell $\mathbf{G}$ is three dimensional, this energy cutoff E_c is expressed in terms of a sphere

$$\frac{1}{2}|\mathbf{G}|^2 \leq E_c \tag{3.44}$$

Another natural advantage of plane waves is the ease of computing the Hartree potential (i.e. mean field classical electrostatic potential defined in eq. 3.13). In real space, the Hartree potential ν_H is written as

$$\nu_H(\mathbf{r}) = \int \frac{\rho(\mathbf{r}')}{|\mathbf{r} - \mathbf{r}'|} d\mathbf{r}' \tag{3.45}$$

In absence of nuclear charge density, in reciprocal space the equation becomes

$$\nu_H(\mathbf{G}) = \frac{4\pi\rho(\mathbf{G})}{\mathbf{G^2}} \tag{3.46}$$

and accordingly the classical electrostatic energy is

$$J[\rho] = 2\pi\Omega \sum_{\mathbf{G}<G_C} \frac{\rho^*(\mathbf{G})\rho(\mathbf{G})}{\mathbf{G^2}} \tag{3.47}$$

Where the Fourier component of the potential for $\mathbf{G} = 0$ is not included. It corresponds to an average, which will result only in a shift. In the case of a charged periodic cell, the potential diverges. In such a situation, a neutralizing charge has to be introduced, e.g. included in the $\mathbf{G} = 0$ background. The external potential due to the nuclei can also be computed in reciprocal space in a similar manner, by adding the nuclear charge density to the density. In practice short-range interactions are often treated differently, in a local representation. The density $\rho(\mathbf{r})$ can be accumulated in real space by summing the plane waves on a real space grid.

$$\rho(\mathbf{r}) = \frac{2}{\Omega} \sum_{i}^{n/2} \sum_{\mathbf{G}} C^*_{i,\mathbf{G}} C_{i,\mathbf{G}} e^{i\mathbf{G}\mathbf{r}} \tag{3.48}$$

In order to obtain $\rho(\mathbf{G})$ from $\rho(\mathbf{r})$, a Fast Fourier Transform (FFT) may be used, yielding $\nu_H(\mathbf{G})$ from the real space density with a scaling of $\mathcal{O}(N \log N)$. Plane waves are by nature orthogonal to each other and their kinetic energy expectation value is trivial to compute. Another advantage is the very good representation of diffuse electron densities. However, the electron density near the atomic centers varies rapidly, so that a very high number of plane waves would be necessary to represent it. This problem is especially important for elements with high electronegativity and even worse for the KS-orbitals of core electrons. This is why pseudopotentials are used in most practical plane wave based computations - they are explained in the next section.

3.7 Pseudopotentials

The computational effort for the electronic structure problem increases greatly with the number of electrons. The electrons in the region around the nuclei are especially problematic from a computational point of view - often without actually affecting the chemistry of the respective atom. The reason why the orbitals of these electrons are difficult to deal with is the 1/r dependency of the Coulomb potential with its singularity at the core. In combination with the orthogonality condition, this leads to a strongly oscillatory behavior in this region ("core-wiggles"). This is difficult to describe with a small basis set, and even more so with a limited set of plane waves, which additionally suffer from the convergence problems described above. Therefore, pseudopotentials are introduced to represent an effective core screened by the core electrons.

The idea is to remove the "inert" core electrons and simultaneously replace the nuclear Coulomb potential with a potential that is smooth and generates the same properties beyond a cutoff distance R_C. Hellmann was the first to introduce the pseudopotential approximation.(68, 69) Numerous advances over the last decades have established pseudopotentials whose effect can be evaluated efficiently and which even include relativistic effects of the core electrons.(70, 71, 72, 73) A good pseudopotential (PSP) must be transferable to different chemical situations and generate a potential as smooth as possible. In this thesis, Norm Conserving Pseudo Potentials (NCPP) as introduced by Hamann et al.(74) are used. If one inserts such a pseudopotential instead of the true Coulomb potential into the Kohn-Sham Hamiltonian one obtains an orthonormalized set of "pseudofunctions" $\varphi_i^{PS}(\mathbf{r})$. These functions are normalized and their decay outside the core mimicks the true wavefunction. Inside the core zone they are smoother than the φ_i of the full Hamiltonian. This smoothness arises also due to the fact that they do not have to be orthogonal to lower states (which have been removed), and thus have less nodes. The cutoff radius R_C can be understood as a quality criterion. The smaller it is, the smaller is the region in space, in which the pseudofunction is allowed to deviate from the all-electron wavefunction. Norm conservation means that inside the cutoff radius R_C, the integrated charge of a valence orbital is equal to that of the pseudofunction

$$\int_0^{R_C} \varphi_i^*(\mathbf{r})\varphi_i(\mathbf{r})d\mathbf{r} = \int_0^{R_C} \varphi_i^{*,PS}(\mathbf{r})\varphi_i^{PS}(\mathbf{r})d\mathbf{r} \tag{3.49}$$

Alltogether the NCPP should fulfill the following criteria

- The eigenvalues of the valence orbitals have to be the same as in the all electron calculation
- $\varphi_i^{PS}(\mathbf{r}) = \varphi_i(\mathbf{r})$ for $R > R_C$
- Norm-conservation (see above)

The criterion of norm-conservation also implies that the logarithmic derivative of the all electron wavefunction

$$D_l = r\frac{d}{dr}\ln\psi_l(\epsilon, r) \tag{3.50}$$

agrees with the pseudofunction at R_C. More interestingly this also implies that the first energy derivative $dD_l/d\epsilon$ agrees at R_C, see (74). This ensures a certain degree of transferability. Transferability may be enhanced further by using a small R_C, which of course also cancels part of the smoothing effect. In order to build accurate pseudopotentials one has to go beyond substituting the nuclear core charge with an effective potential only in $\mathbf{r}$, the potential needs to depend also on the angular momentum of the electrons - in analogy with nondegenerate atomic orbitals. Such a semilocal pseudopotential may be written as

$$\hat{\mathbf{V}}_{SL} = \mathbf{V}(\mathbf{r}) + \sum_{lm} |Y_{lm}\rangle \mathbf{V}_l(\mathbf{r}) \langle Y_{lm}| \tag{3.51}$$

Where the notion of semilocality refers to $\mathbf{V}_l(\mathbf{r})$ being only a function of $\mathbf{r}$. The semilocal pseudopotential gives a good impression on how these potentials act on the valence orbitals: the spherical harmonics project the wavefunction into "seeing " the potential corresponding to the angular momentum dependent atomic orbital of the target valence state. However, projecting planewaves on a localized basis of angular momentum eigenfunctions is very expensive numerically, as can be seen from the expectation value for $\hat{\mathbf{V}}_{SL}$, whose computation necessitates the evaluation of a double radial integral. Kleinman and Bylander(72) could show that it is possible to approximate such a semilocal PSP by a nonlocal one, with a set of localized projectors.

$$\hat{\mathbf{V}}_{NL} = \mathbf{V}(\mathbf{r}) + \sum_{lm} \frac{|\varphi_{lm}^{PS} \mathbf{V}_l(\mathbf{r})\rangle \langle \varphi_{lm}^{PS} \mathbf{V}_l(\mathbf{r}')|}{\langle \varphi_{lm}^{PS} | \mathbf{V}_l(\mathbf{r}) | \varphi_{lm}^{PS} \rangle} \tag{3.52}$$

This construction leads to a $\hat{\mathbf{V}}_{NL}(\mathbf{r}, \mathbf{r}')$ which is fully nonlocal. To understand this consider $\langle \varphi_{lm}^{PS} \mathbf{V}_l(\mathbf{r})|$, which is a projector for the angular momentum dependent part of the pseudopotential. It is localized, because

$$\langle \varphi_{lm}^{PS} \mathbf{V}_l(\mathbf{r}) | \varphi_i(\mathbf{r}) \rangle = \int d\mathbf{r} \mathbf{V}_l(\mathbf{r}) \varphi_{lm}^{PS}(\mathbf{r}) \varphi_i(\mathbf{r}) \text{ is zero outside } R_C \tag{3.53}$$

These projectors are built using the pseudofunctions of the atom, introducing a further approximation, but they allow for efficient numerical calculation of the pseudopotential interaction, because the matrix elements

$$\langle \varphi_i | \hat{\mathbf{V}}_{NL}(\mathbf{r}) | \varphi_j \rangle \tag{3.54}$$

now just require a product of projection operators instead of the double spatial integration of the full semilocal PSP. In order to further improve performance and simplicity, one may choose Gaussian shaped projectors. This is the Goedecker-Teter-Hutter (GTH) approach to pseudopotentials.(73) The GTH pseudopotentials can be written as a sum of a local and a nonlocal part, the local part being

$$\mathbf{V_{loc}^{PP}}(\mathbf{r}) = -\frac{Z}{\mathbf{r}} erf\big(\frac{\mathbf{r}}{\sqrt{2}r_{loc}}\big) \sum_{i=1}^{4} C_i^{PP} \big(\frac{\mathbf{r}}{r_{loc}}\big)^{2i-2} e^{-(\frac{1}{2}\frac{\mathbf{r}}{r_{loc}})^2} \tag{3.55}$$

and the nonlocal part

$$\mathbf{V_{nloc}^{PP}}(\mathbf{r},\mathbf{r}') = \sum_{lm}\sum_{ij} \underbrace{N_i^l Y_{lm} r^{l+2i-2} e^{-\frac{1}{2}(\frac{\mathbf{r}}{r_{loc}})^2}}_{|rp_{lm}^i\rangle} h_{ij}^l \langle r' p_{lm}^j| \tag{3.56}$$

Where C_i, h_{ij} and r_{loc} are parameters and N_i is a normalization factor. As can be seen the projectors p_{lm} are Gaussian in real space - and thus also Gaussian in Fourier space. This allows for analytical integrals. In this work the GTH potentials and the Troullier Martin(75) potentials have been used. For a summary on different methods to generate pseudopotentials see (70).

3.8 Combination of Gaussians, planewaves and pseudopotentials

Plane waves and Gaussians may be combined to improve computational performance and accuracy or even to do away with the need for pseudopotentials.

3.8.1 The GPW method

The Gaussians and plane waves (GPW) approach(76) uses Gaussians for the Kohn-Sham orbitals, but expands these in plane waves for the density dependent Hartree energy, combining the numerical advantages of both methods.

In order to make use of the numerical advantages of both methods, a way to express $\rho(\mathbf{r})$ in Gaussians as well as in plane waves is needed. The density in any basis can be written using its density matrix $\mathbf{P}$, in the closed shell case

$$\rho(\mathbf{r}) = 2\sum_{i}^{n/2} \varphi_i^*(\mathbf{r})\varphi_i(\mathbf{r}) = 2\sum_{i}^{n/2}\sum_{\mu} C_{\mu i}^* \chi_\mu^*(\mathbf{r}) \sum_{\nu} C_{\nu i}\chi_\nu(\mathbf{r}) \tag{3.57}$$

this expression can be simplyfied

$$\rho(\mathbf{r}) = \sum_{\mu}\sum_{\nu} \underbrace{[2\sum_{i}^{n/2} C_{\mu i}^* C_{\nu i}]}_{P_{\mu\nu}} \chi_\nu(\mathbf{r})\chi_\mu^*(\mathbf{r}) \tag{3.58}$$

$$\rho(\mathbf{r}) = \sum_{\mu\nu} P_{\mu\nu}\chi_\mu^*(\mathbf{r})\chi_\nu(\mathbf{r}) \tag{3.59}$$

Where the Matrix of the $P_{\mu\nu}$ is the density matrix. In the PW basis the closed shell density is

$$\rho(\mathbf{r}) = \frac{1}{\Omega} 2\sum_{i}^{n/2}\sum_{\mathbf{G}} C_{i,\mathbf{G}}^* C_{i,\mathbf{G}} e^{i\mathbf{G}\mathbf{r}} \tag{3.60}$$

The Fourier coefficents of the density in the PW basis may be obtained by FFT of $\rho(\mathbf{r})$ on a grid. The density is expanded in a plane wave "auxiliary" basis set. This is advantageous, not only because the Hartree energy can be computed by FFT; the density also varies more smoothly than the orbitals, decreasing the size of the necessary basis. The idea of using a more convenient basis set for the density was first applied to pure Gaussian basis sets where it is known as the resolution of identity (RI) method.(77) Nevertheless, pseudopotentials still have to be used in practice, to allow converging the electrostatic part of the computation. For the kinetic energy, Gaussians may be used efficiently, because in the Gaussian basis the expression

$$\int P_{\mu\nu}\chi_\mu(\mathbf{r})\frac{1}{2}\nabla^2\chi_\nu(\mathbf{r})d\mathbf{r} \tag{3.61}$$

can be solved analytically. The Gaussian basis set is better suited to compute the orbital Laplacians, as it can easily reproduce orbital "spikes". As the Gaussian basis functions on different centers are not orthogonal, the calculation of overlap integrals is also necessary (see section 3.9). As the kinetic energy and overlap integrals are integrals over all of space, the periodic boundary conditions have to be respected. The Gaussian basis set is therefore expanded to also include the periodic images, multiples of the cell vector $\mathbf{l}$.

$$\chi_\mu = \sum_i \chi_\mu(\mathbf{r} - \mathbf{l}_i) \tag{3.62}$$

Of course there are in principle infinitely many mirror images in any dimension. However, as the product of the localized Gaussians in eq. 3.61 rapidly goes to zero, the integral vanishes. A cutoff to the product of the Gaussian functions is therefore employed to truncate the summation. The exchange-correlation energy also depends only on the local density in real space, or its gradient in the case of GGA. Therefore it may also be efficiently computed using the Gaussian basis set.

Summarizing, the GPW method uses GTOs for all computations besides the Hartree energy. It thereby exploits the properties of plane waves for periodic electrostatic computations while keeping the convergence and numerical advantages of Gaussians for the other properties. As the Hartree term is usually the most expensive part of the calculation scaling with a formal scaling of N^4 in a GTO basis set, the scaling properties are also improved. However, the necessity to keep densities in both representations equal limits the accuracy, because the soft properies of PW densities as well as the good behavior of atomic centers cannot be fully harnessed.

3.8.2 The GAPW method

Using an appropriate projection, it is possible to decompose the density and the KS orbitals in the core region into slowly varying smooth functions (expanded in plane waves) and a rapidly varying part, typically a predetermined frozen core. This is the idea behind the projector augmented wave (PAW) method.(78) If one instead uses flexible Gaussian orbitals in the core region, it becomes the GAPW method.(79) The first step is to decompose the density into three parts

$$\rho = \widetilde{\rho} - \widetilde{\rho}^1 + \rho^1 \tag{3.63}$$

The soft density $\widetilde{\rho}$ is smooth and distributed over all space. Centered at the atomic cores A there is a hard and a soft one center density ρ^1 and $\widetilde{\rho}^1$.

$$\rho^1 = \sum_A \rho_A^1 \text{ and } \widetilde{\rho}^1 = \sum_A \widetilde{\rho}_A^1 \tag{3.64}$$

Outside the core region, these densities are constructed to be equal and thus cancel out. The spherical region around the atomic cores is defined as the environment U_A. The space outside the core region is the insterstitial region I. The aim is to have a well defined soft density also in U_A, which can be well separated from the atom centered hard density. For this, the following conditions have to be met:

$$\rho(\mathbf{r}) - \widetilde{\rho}(\mathbf{r}) = 0 \text{ for } \mathbf{r} \in I \tag{3.65}$$

$$\rho(\mathbf{r})^1_A - \widetilde{\rho}(\mathbf{r})^1_A = 0 \text{ for } \mathbf{r} \in I \tag{3.66}$$

$$\widetilde{\rho}(\mathbf{r}) - \widetilde{\rho}(\mathbf{r})^1_A = 0 \text{ for } \mathbf{r} \in U_A \tag{3.67}$$

$$\rho(\mathbf{r}) - \rho(\mathbf{r})^1_A = 0 \text{ for } \mathbf{r} \in U_A \tag{3.68}$$

The purpose of this separation is the possibility to use a plane wave expansion for the soft density, while using Gaussians for the atomic environment U_A. As, contrary to the GPW method, the global density does not have to be equal in both basis sets, the different convergence properties may be used. The diffuse part rapidly converges in plane waves, while the part near the atomic cores is much better suited to treatment with Gaussians. The difficulty is to construct projections, so that the separation criteria in eq. 3.65 ff. hold. The soft density $\widetilde{\rho}$ may be expanded in smooth Gaussians $\widetilde{\chi}_\mu(\mathbf{r})$, by removing the Gaussians with an exponent above a critical value from the basis set. It can then be written as

$$\widetilde{\rho}(\mathbf{r}) = \sum_{\mu\nu} P_{\mu\nu} \widetilde{\chi}_\mu(\mathbf{r}) \widetilde{\chi}_\mu(\mathbf{r}) \tag{3.69}$$

However, a planewave expansion is also possible - and in the intention of the decomposition. In order to construct ρ^1 and $\widetilde{\rho}^1$, for the contributions centered on any atom A, a separation by exponent in "hard" and "soft" Gaussians is sufficient. However, as the atom centered density on A is computed only from Gaussians centered on A in order to also treat contributions, which are not centered on the same atom, a Gaussian projector basis $\{p_j\}$ has to be introduced, which projects contributions from other atoms on the atom center at A. The primitive gaussians of these other atoms are denoted as g_b. The projection leads to a new set of coefficients

$$\langle p_a | \varphi_\mu \rangle = \sum_{b \neg @ A} C^A_{b\mu} \langle p_a | g_b \rangle \tag{3.70}$$

The coefficients $C^A_{b\mu}$ can be obtained by the inversion of the overlap matrix defined by the above equation. ρ^1_A can be shown to be

$$\rho^1_A = \sum_{a,b@A} \sum_{\mu,\nu} C^A_{a\mu} P_{\mu\nu} C^A_{b\nu} g_a g_b \tag{3.71}$$

$\widetilde{\rho}^1$ can be obtained from the same expression after removing the coefficients corresponding to the "hard" Gaussians. The total density can now be separated according to eq. 3.63. As there is a double and equivalent representation of the densities into a soft and the hard part, the corresponding XC-energies may also be written to cancel out in the following way:

$$E_{XC}[\rho] = E_{XC}[\widetilde{\rho}] - E_{XC}[\widetilde{\rho}^1] + E_{XC}[\rho^1] \tag{3.72}$$

This decomposition may easily be computed for all local quantities. However, the nonlocal Hartree energy is introduces further complications. In contrast to the GPW method, it can not simply be computed from a plane wave density. Instead, hard and soft screening densities ρ^0 are introduced using a multipole expansion at the centers A.

$$\rho^0 = \sum_A \rho^A_1 = \sum_{ml} Q^{lm}_A g^{lm}_A \tag{3.73}$$

The screening densities are expanded in sets of hard and soft Gaussian functions g^{lm}_A respectively, the soft part is

$$\widetilde{\rho}^0 = \sum_A \widetilde{\rho}^1_A = \sum_{ml} Q^{lm}_A \widetilde{g}^{lm}_A \tag{3.74}$$

The Q^{ml}_A are defined as

$$Q^{ml}_A = N q^{ml}_A [\rho^1 - \widetilde{\rho}^1 + \rho^Z_A] \tag{3.75}$$

Where q^{lm}_A is the multipole moment operator and ρ^Z_A is the core charge density. The screening densities cancel the electrostatic multipole moments of the one center densities. The Hartree energy can then be decomposed into different parts. The global soft density's J can be computed using the plane wave representation and the screening densities are atom centered and may be computed by Ewald summation, the short range part of the localized densities are computed using the Gaussian representation.

The use of Gaussians in fully periodic calculations together with the plane-wave soft basis allows to forego the use of pseudopotentials and to do efficient and accurate all-electron calculations in periodic systems. This reflects the state of the art as implemented in the CP2K program(80).

3.9 Self consistent solution of the Kohn-Sham equations

After showing the construction of the Kohn-Sham orbitals and their associated electron density, and discussion of the numerical evaluation of the energy as function of these quantities, one important aspect has not been discussed yet. Taking a look at the Kohn-Sham equations, we find that the energy minimized by the KS-orbitals depends on these orbitals themselves. The Kohn-Sham equations are therefore nonlinear, as are the Hartree-Fock equations. A solution has to be *self-consistent*, such that applying the variational principle to a set of orbitals does not change the background potential any further. For this reason, Hartree-Fock is also known as the self-consistent-field (SCF) method. Evaluating the KS-or Fock operator in any single basis gives for $\varphi_i(\mathbf{r})$

$$\sum_{\mu} C_{\mu i} \hat{f}(\mathbf{r}) \chi_{\mu}(\mathbf{r}) = \epsilon_i \sum_{\mu} C_{\mu i} \chi_{\mu i}(\mathbf{r}) \tag{3.76}$$

Multiplying on the right with the basis functions $\chi^*_{\nu}(\mathbf{r})$ and integrating over $\mathbf{r}$ yields a matrix equation

$$\sum_{\mu i} C_{\mu i} \int d\mathbf{r} \chi^*_{\nu}(\mathbf{r}) \hat{f}(\mathbf{r}) \chi_{\mu}(\mathbf{r}) = \epsilon_i \sum_{\mu} C_{\mu i} \int d\mathbf{r} \chi^*_{\nu}(\mathbf{r}) \chi_{\mu}(\mathbf{r}) \tag{3.77}$$

The Matrix equation can be abbreviated by defining a number of matrices, the first being the overlap matrix $\mathbf{S}$

$$S_{\nu\mu} = \int d\mathbf{r} \chi^*_{\nu}(\mathbf{r}) \chi_{\mu}(\mathbf{r}) \tag{3.78}$$

The second being the Kohn-Sham or Fock matrix $\mathbf{F}$.

$$F_{\nu\mu} = \chi^*_{\nu}(\mathbf{r}) \hat{f}(\mathbf{r}) \chi_{\mu}(\mathbf{r}) \tag{3.79}$$

One may now rewrite eq. 3.77 as

$$\sum_{\mu} F_{\nu\mu} C_{\mu i} = \epsilon_i \sum_{\mu} S_{\mu\nu} C_{\mu i} \tag{3.80}$$

After defining the coefficient matrix $\mathbf{C}$ for $C_{\mu i}$, the entire problem in all i can be written in terms of a matrix equation.

$$\mathbf{FC} = \mathbf{SC}\epsilon \tag{3.81}$$

This formulation (also known as Roothaan-Hall equation), allows to apply standard matrix algebra algorithms to be used for obtaining the orbitals. In the case of orthogonal orbitals, i.e. $S = \mathbf{I}$

$$\mathbf{FC} = \mathbf{C}\epsilon \tag{3.82}$$

To solve this eigenvalue type problem, one would have to merely diagonalize $\mathbf{F}$. Therefore, the solution of the KS-equations generally begins with a diagonalization of $\mathbf{S}$. Note that in a plane-wave basis, this problem vanishes. The Fock matrix may in turn be expressed in terms of the density matrix, which depends on the coefficients, therefore

$$\mathbf{F}(\mathbf{C})\mathbf{C} = \mathbf{SC}\epsilon \tag{3.83}$$

This means the equation is still nonlinear. In order to achieve self-consistency, the potential is optimized iteratively, departing from an initial guess for the density matrix $\mathbf{P}(\mathbf{C})$, see eq. 3.59. A typical way to obtain an initial guess is to depart from a superposition of the atomic (pseudo)wavefunctions in a minimal localized basis and then expand in the full basis set. Coefficients have different ranges, it is therefore advantageous to precondition the SCF problem, leading to the introduction of further transformation matrices. Once the coefficent matrix for a "trial" Fock operator is found, a new density matrix will be computed from it and the Fock operator will be evaluated again. When this procedure does not change the coefficients anymore, self-consistency has been achieved.

There are two basically different approaches to efficicently solving the SCF problem, one being the direct minimization techniques the, other being fix-point methods. The

most common direct minimization algorithm in the field of SCF theory is called *direct inversion of the iterative subspace* (DIIS).(81)

The DIIS procedure produces nonorthogonal orbitals. This leads to the need of a reorthogonalization step, by e.g. Gram-Schmidt or Löwdin orthonormalization techniques.

3.10 Response and second order properties

3.10.1 Density functional perturbation theory

Kohn-Sham DFT is based on variational minimization of the energy. Many properties of interest, such as polarizabilities, NMR chemical shifts and IR-spectra based on analytical second derivatives require knowledge of states above the variational minimum. This is because they are "second" order, i.e. they contain second derivatives of the energy. This means they cannot be obtained by the Hellmann-Feynman theorem directly. The approach taken to their calculation is based on perturbation theory. In standard quantum mechanics, the Hamiltonian of the system is rewritten as a combination of the original Hamiltonian $\hat{H}_0$ and the perturbation Hamiltonian $\hat{H}_1$, which is scaled by the perturbation parameter λ. For clarity, the discussion of degenerate states is omitted. The section follows the description in (82).

$$\hat{H} = \hat{H}_0 + \lambda \hat{H}_1 \tag{3.84}$$

The wavefunction and energies can be written as a power series in λ

$$E = E^{(0)} + \lambda E^{(1)} + \lambda^2 E^{(2)} + \cdots + \lambda^n E^{(n)} \tag{3.85}$$

$$|\psi\rangle = |\psi^{(0)}\rangle + \lambda|\psi^{(1)}\rangle + \lambda^2|\psi^{(2)}\rangle + \cdots + \lambda^n|\psi^{(n)}\rangle \tag{3.86}$$

If the perturbation is sufficiently small, the series should converge quickly in low orders of λ. Linear response means only considering terms first order in λ. Not only energy and wavefunction, but any property X (e.g. the density) may thus be written in a power series, where each order obeys

$$X^{(n)} = \frac{1}{n!}\frac{d^n X}{d\lambda^n} \tag{3.87}$$

Within the framework of density functional perturbation theory (DFPT)(83), this wavefunction based theory is rewritten in terms of the total energy functional E_{KS}. This allows perturbations which are not expressible with a Hamiltonian to be computed.

$$E_{KS}^{tot}[\{\varphi_i\}] = E_{KS}^{(0)}[\{\varphi_i\}] + \lambda E_{KS}^{pert}[\{\varphi_i\}] \tag{3.88}$$

With $E_{KS}^{(0)}$ as the unperturbed Kohn-Sham energy and thus the orbitals φ consitute a variational minimum. Minimizing the total expression for a sufficiently small perturbation E_{KS}^{pert} seems like a straightforward approach. This finite difference method is however relatively expensive and has numerical stability problems. Instead the analytical derivative is taken. To do this, the KS wavefunction is expanded in a power series, analogous to eq. 3.86, so that

$$E_{KS}^{(tot)}[\{\varphi_i^{(0)} + \lambda\varphi_i^{(1)} \dots\}] = E^{(0)} + \lambda E^{(1)} + \lambda^2 E^{(2)} \dots \tag{3.89}$$

Here the expression is truncated after second order in the energy. The energy term which is linear in λ vanishes because of the stationarity of the $\varphi_i^{(0)}$, see eq. 3.87. It can be shown that the first nonvanishing term is the second order energy.

This leads to the stationarity condition

$$\frac{\delta E^{(tot)}}{\delta\varphi_i^{(1)}} = 0 \tag{3.90}$$

In order to allow a variational scheme on the perturbative expansion in $\varphi_i^{(1)}$, it is helpful to restrict the space in which the response orbitals are being constructed by introducing a so called parallel transport gauge. Restricting ourselves to linear order in φ_i, this gauge can be written as

$$\langle\varphi_i^{(1)}|\varphi_{i'}^{(0)}\rangle = 0; \forall i, i' \tag{3.91}$$

This ensures the manifold of response orbitals to be orthogonal to the ground state orbitals. The parallel transport gauge is enforced via Lagrange multipliers. The resulting system of equations is of the Sternheimer type:

$$-\mathbf{P}_e(\hat{H}_{KS}^{(0)} - \epsilon_i^{(0)})\mathbf{P}_e|\varphi_i^{(1)}\rangle = \mathbf{P}_e\left[\int d^3\mathbf{r}' f_{HXC}(\mathbf{r},\mathbf{r}')\rho^{(1)}(\mathbf{r}')|\varphi_i^{(0)}\rangle + \frac{\delta E_{KS}^{pert}}{\delta\langle\varphi_i^{(0)}|}\right] \tag{3.92}$$

The derivation of eq. 3.92 is given in the literature(83, 84, 85), constituting terms will be discussed on a qualitative basis.

$$f_{HXC}(\mathbf{r}, \mathbf{r}') = \frac{\delta^2(E_H + E_{XC})}{\delta\rho(\mathbf{r})\delta\rho(\mathbf{r}')} \tag{3.93}$$

f_{HXC} is the Hartree and exchange-correlation kernel. This is the most important quantity involved in computing the response as it handles the electronic interactions, i.e. describes the response of the electron-electron interactions to a change in the density via the change in Hartree and XC-potentials. It reappears in further detail in the description of TD-DFT, where it is defined and discussed as a frequency dependent quantity (see the corresponding sections). In static DFPT one operates within the zero frequency limit. The projection operator $\mathbf{P}_e$ projects on the manifold of unoccupied orbitals, it is written as

$$\mathbf{P}_e = \sum_i 1 - |\varphi_i\rangle\langle\varphi_i| \tag{3.94}$$

The Sternheimer equation 3.92 is solved self-consistently, using direct minimization algorithms such as conjugate gradients. As the nature of the perturbation E^{pert} has not been defined the approach may be used for a wide variety of properties.

3.10.2 Calculation of NMR shifts

The property being considered in this work are chemical shifts, accessible by NMR spectroscopy. When a homogeneous, external magnetic field is applied to the system the nuclear magnetic moment becomes dependent on the spin quantum number m. Given in standard SI units:

$$E = -\gamma m \hbar B^{tot} \tag{3.95}$$

The total magnetic field $\mathbf{B}^{tot}$ is a sum of external and induced magnetic field

$$\mathbf{B}^{tot} = \mathbf{B}^{ext} + \mathbf{B}^{ind} \tag{3.96}$$

The nuclear shielding tensor of a nucleus K is defined as

$$\sigma_{ij}(\mathbf{R_k}) = -\frac{\partial B_i^{ind.}(\mathbf{R_k})}{\partial B_j^{ext}} \tag{3.97}$$

The isotropic chemical shifts may be obtained from the nuclear shielding tensor by taking the trace

$$\sigma_{iso} = \frac{1}{3} Tr \underline{\sigma} \tag{3.98}$$

It may then be referenced to a standard - in the case of protons this is usually the absolute shielding of the tetramethylsilane (TMS) protons.

$$\delta \equiv \sigma_{ref} - \sigma_{iso} \tag{3.99}$$

In order to obtain the experimental chemical shielding δ, one has to compute a reference shielding tensor on the same level of theory. For the shielding tensor, the computation of the induced field is done via the law of Biot-Savart:

$$\mathbf{B}^{ind}(\mathbf{r}) = \frac{1}{c} \int d^3\mathbf{r}' \mathbf{j}_{el}(\mathbf{r}') \times \frac{(\mathbf{r} - \mathbf{r}')}{|\mathbf{r} - \mathbf{r}'|^3} \tag{3.100}$$

The integral over the current density $\mathbf{j}_{el}$ necessitates the computation of the current induced by the external magnetic field. The external magnetic field is introduced into the DFPT perturbation scheme via its vector potential $\mathbf{A}(\mathbf{r})$

$$\mathbf{B}^{ext} = \nabla \times \mathbf{A}(\mathbf{r}) \tag{3.101}$$

The perturbation is thus a static magnetic field. To include it into the Hamiltonian, the single particle momentum operator $\hat{\mathbf{p}}$ has to be replaced by the canonical momentum operator $\hat{\pi} = \hat{\mathbf{p}} - q/c\mathbf{A}(\mathbf{r})$. Accordingly, the one particle Hamiltonians transform to

$$\hat{h} = \frac{1}{2}(\hat{\mathbf{p}} - \frac{q}{c}\mathbf{A}(\mathbf{r}))^2 + \nu(\mathbf{r}) \tag{3.102}$$

$$\hat{h} = \frac{1}{2}\hat{\mathbf{p}}^2 - \frac{q}{2c}(\hat{\mathbf{p}}\mathbf{A}(\mathbf{r}) + \mathbf{A}(\mathbf{r})\hat{\mathbf{p}}) + \nu(\mathbf{r}) + \frac{q^2}{2c^2}A^2 \tag{3.103}$$

At first order in the perturbation parameter (here: the strength of the external magnetic field), the perturbation Hamiltonian is identified as

$$\hat{H}_1 = -\mathbf{p} \cdot \mathbf{A}(\mathbf{r}) \tag{3.104}$$

The vector potential $\mathbf{A}(\mathbf{r})$ has a gauge origin, as is well known from classical electrodynamics. In the classical Coulomb gauge it can be chosen as

$$\mathbf{A}(\mathbf{r}) = -\frac{1}{2}\mathbf{r} \times \mathbf{B}^{ext} \rightarrow \hat{H}_1 = \mathbf{p} \times \frac{1}{2}\mathbf{r} \cdot \mathbf{B}^{ext} \tag{3.105}$$

where the angular momentum operator is part of the perturbation. Putting this perturbation into eq. 3.92, one obtains the Sternheimer equations

$$-\mathbf{P}_e(\hat{H}^{(0)}_{KS} - \epsilon^{(0)}_i)\mathbf{P_e}|\varphi^{(1)}_i\rangle = \mathbf{P}_e[\mathbf{r} \times \hat{\mathbf{p}}|\varphi^{(0)}_i\rangle] \tag{3.106}$$

Here the perturbation parameter λ is the external magnetic field $\mathbf{B}^{ext}$, so that the perturbation has to be evaluated separately in all directions. Eq. 3.106 is simplified because the change in the KS orbitals is purely imaginary. As $\rho^{(1)} = 0$ analytically, this makes the self-consistent evaluation of the density response via f_{HXC} unnecessary. From the response orbitals it is possible to compute $\mathbf{j}_{el}(\mathbf{r})$ needed for the computation of the induced magnetic field $\mathbf{B}^{ind}(\mathbf{r})$ in eq. 3.100.

$$\mathbf{j}_{el}(\mathbf{r}) = \frac{1}{2}\sum_i f_i \Re[\varphi^{(1)*}_i \nabla \varphi^{(0)}_i + \varphi^{(0)*}_i \nabla \varphi^{(1)}_i] + \rho(\mathbf{r})\mathbf{A}(\mathbf{r}) \tag{3.107}$$

Which has to be done separately for the different components of the external magnetic field. Thus, the computation of chemical shifts is performed via DFPT. Some practical problems in the computation of the chemical shifts have not been discussed so far. Aside from the gauge origin problem, there are connected problems which arise from the periodicity of the position operator and the ensuing complications for the angular momentum operator in periodic boundary conditions. These problems can be circumvented by localization(86) and adjustment of the gauge-origin, see below.

The gauge origin problem

Returning to the derivation of the magnetic fields $\mathbf{B}(\mathbf{r})$ of the vector potential $\mathbf{A}(\mathbf{r})$

$$\mathbf{B}(\mathbf{r}) = \nabla \times \mathbf{A}(\mathbf{r}) \tag{3.108}$$

This vector potential is not unique, because the magnetic field may be derived from an infinite number of vector potentials. These potentials are related by the following gauge transformation

$$\mathbf{A}(\mathbf{r}) \rightarrow \mathbf{A}'(\mathbf{r}) = \mathbf{A}(\mathbf{r}) + \nabla\phi(\mathbf{r}) \tag{3.109}$$

Where $\phi(\mathbf{r})$ is an arbitrary scalar function. This gauge freedom does not change the physical magnetic field $\mathbf{B}$. In a real NMR calculation, one can choose for example

$$\phi(\mathbf{r}) = \mathbf{r} + \mathbf{R_0} \tag{3.110}$$

Where $\mathbf{R_0}$ is an arbitrary point in space, called the gauge origin. In a numerical calculation, instead, the results can depend strongly on the choice of the gauge origin. The reason for this is that the numerical evaluation relies on a cancellation of two large terms in the diagmagnetic and the paramagnetic current density.

$$\mathbf{j}_{el}(\mathbf{r}) = \underbrace{\frac{1}{2}\sum_o f_o[\varphi_o^{(1)*}\nabla\varphi_o^{(0)} + \varphi_o^{(0)*}\nabla\varphi_o^{(1)}]}_{\mathbf{j_{para}}} + \underbrace{\rho(\mathbf{r})\mathbf{A}(\mathbf{r})}_{\mathbf{j_{dia}}} \tag{3.111}$$

Each individual term is not gauge invariant. In practice

$$\mathbf{j}_{dia}(\mathbf{r}') \propto R_0^2 \tag{3.112}$$

Solving this problem therefore relies on keeping the largest part of the induced current for a given core coordinate close to the gauge origin. Approaches include

- The Gauge Including Atomic Orbitals (GIAO) $\rightarrow$ position of each atom R_K as gauge origin R_0 for all their orbitals.(87)
- Individual Gauges for Localized Orbitals (IGLO) $\rightarrow$ center of charge of the molecular orbitals as origin.(88)
- Continuous Set of Gauge Transformations (CSGT) $\rightarrow$ sets the gauge origin to each point where the current is evaluated.(89) This removes the diamagnetic term.

In this work an implementation by Weber and others(90) has been used, which is based on IGAIM(91). IGAIM is a variation on IGLO, where the Atoms in molecules approach is used to determine the adjacent nuclear center which is then used as the gauge origin.

3.11 Time-dependent density functional theory

The following introduction closely follows relevant sections the introductory chapter by Gross and Maitra in (92).

3.11.1 The Runge-Gross theorem

The Hohenberg-Kohn theorems only concern ground state wavefunctions and energies. The ground state density determines also the stationary excited states, as it uniquely identifies the Hamiltonian via the external potential. However, there are several ν_{ext} which may lead to the same excited state density.(93) This precludes a straightforward extension to an excited state energy functional. The rigorous extension of DFT to solving time-dependent problems and finding excited states was accomplished by the Runge-Gross theorem.(94) The resulting theory is called time-dependent DFT (TD-DFT). The Runge-Gross (RG) theorem states that there exists a unique mapping between the time-dependent potential $\nu_{ext}(\mathbf{r}, t)$ and the density $\rho(\mathbf{r}, t)$, given an initial state at t_0. This means that (with some limitations) even the time-dependent problem can be solved knowing only the density. One limitation is that the proof requires the time-dependent potential to be Taylor expandable. The proof of the RG-theorem, departs from the current density $\mathbf{j}(\mathbf{r}, t)$. The time evolution of the expectation value of any operator $\hat{Q}(t)$ can be obtained from the following Heisenberg equation of motion:

$$\frac{\partial}{\partial t}\langle\Psi(t)|\hat{Q}(t)|\Psi(t)\rangle = \langle\Psi(t)|\frac{\partial\hat{Q}(t)}{\partial t} - i[\hat{Q}(t), \hat{H}(t)]|\Psi(t)\rangle \tag{3.113}$$

If the current density $\mathbf{j}(\mathbf{r}, t)$ and its operator $\hat{\mathbf{j}}(\mathbf{r})$ are used, the equation becomes

$$\frac{\partial}{\partial t}\mathbf{j}(\mathbf{r}, t) = \langle\Psi(t)|(-i[\hat{\mathbf{j}}(\mathbf{r}), \hat{H}(t)])|\Psi(t)\rangle \tag{3.114}$$

Changing the Hamilton operator $\hat{H}(t)$ in the external potential $\nu_{ext}(\mathbf{r}, t) \rightarrow \nu'_{ext}(\mathbf{r}, t)$ to become $\hat{H}'(t)$. (Note that the potential has to be different by more than just a time-dependent function, otherwise physical observables will be equal, as this represents a gauge freedom.) The resulting current density $\mathbf{j}'(\mathbf{r}, t)$ is

$$\frac{\partial}{\partial t}\mathbf{j}'(\mathbf{r}, t) = \langle\Psi(t)|(-i[\hat{\mathbf{j}}(\mathbf{r}), \hat{H}'(t)])|\Psi(t)\rangle \tag{3.115}$$

If there are two equal current densities originating from different external potentials and the same time zero state $\Psi(t = 0) = \Psi_0$ for a noninfinitesimal amount of time after $t = 0$, this would break the mapping of the density evolution to the potential. For such a mapping to exist, the difference

$$\frac{\partial}{\partial t}[\mathbf{j}(\mathbf{r},t)-\mathbf{j}'(\mathbf{r},t)]\bigg|_{t=0}=-\rho_0(\mathbf{r})\nabla[\nu_{ext}(\mathbf{r},0)-\nu'_{ext}(\mathbf{r},0)] \tag{3.116}$$

must not vanish. In order to show this, the potentials $\nu_{ext}(\mathbf{r},t)$ must be expandable in a power series.

$$\nu_{ext}(\mathbf{r},t)=\sum_{k=0}^{\infty}\frac{1}{k!}\nu_{ext,k}(\mathbf{r})t^k \tag{3.117}$$

This can also be done for the difference of the potential, then in the Taylor expansion there has to be a smallest integer k so that

$$\nu_{ext,k}(\mathbf{r})-\nu'_{ext,k}(\mathbf{r})=\frac{\partial^k}{\partial t^k}[\nu_{ext,k}(\mathbf{r},t)-\nu'_{ext,k}(\mathbf{r},t)]\neq const. \tag{3.118}$$

The general operator $\hat{Q}(t)$ in eq. 3.113 is now constructed by recursively substituting $\hat{\mathbf{j}}(\mathbf{r})$ by its commutator with $\hat{H}(t)$ until k nested commutators are obtained:

$$\hat{Q}(t)=(-i)^k[[\ldots[\hat{\mathbf{j}}(\mathbf{r}),\hat{H}(t)],\hat{H}(t)],\ldots\hat{H}(t)]_k \tag{3.119}$$

This leads to

$$\left(\frac{\partial}{\partial t}\right)^{k+1}[\mathbf{j}(\mathbf{r},t)-\mathbf{j}'(\mathbf{r},t)]\bigg|_{t=0}=-\rho_0(\mathbf{r})\nabla\left(\frac{\partial}{\partial t}\right)^{k}[\nu_{ext}(\mathbf{r},t=0)-\nu'_{ext}(\mathbf{r},t=0)]\neq 0 \tag{3.120}$$

Again this equation has to be nonzero, because in the order k the potential difference is not constant. This proves

$$\mathbf{j}(\mathbf{r},t)\neq\mathbf{j}'(\mathbf{r},t) \tag{3.121}$$

Having shown that a current density mapping exists, it now has to be led back to the density. The starting point is the continuity equation:

$$\frac{\partial\rho(\mathbf{r},t)}{\partial t}=\nabla\cdot\mathbf{j}(\mathbf{r},t) \tag{3.122}$$

For the expansion in k, this yields

$$\left(\frac{\partial}{\partial t}\right)^{k+2}[\rho(\mathbf{r},t)-\rho'(\mathbf{r},t)]\bigg|_{t=0}=-\nabla\cdot\rho_0(\mathbf{r})\nabla\left(\frac{\partial}{\partial t}\right)^{k}[\nu_{ext}(\mathbf{r},0)-\nu'_{ext}(\mathbf{r},0)] \tag{3.123}$$

The proof is complete if the right hand side can be shown not to be rendered zero over all of space by the divergence operator. To show this with full rigor is beyond the scope of this thesis - It should be intuitive that this is the case for all physically reasonable potentials from the close analogy with the Poisson equation. For a detailed discussion see the book by Gross.(95) The RG theorem establishes a one-to-one correspondence between initial state Ψ_0 and potential on one side and the density on the other.

$$\Psi_0 : \nu_{ext} \leftrightarrow \rho. \tag{3.124}$$

This provides a rigorous foundation for treating any time-dependent problems with DFT. The theorem goes far beyond stationary excited states and even beyond fermions, as no specific assumption has been made on the particle particle interactions. However, it is still lacking a method to apply it. A universal way to apply it seems difficult due to the lack of a variational principle or stationary condition for the density.

3.11.2 Time dependent Kohn-Sham formalism

For the same reasons as in ground state DFT, the TD-DFT is usually cast in the frame of a Kohn-Sham noninteracting particle ansatz. Now as the RG theorem is very general with respect to the form of the Hamiltonian, it also covers the noninteracting system. Thus, the correspondence exists for $\nu_{XC} = 0$. Far more important is the question, whether a $\nu_{XC}(\mathbf{r}, t)$ potential exists to give a noninteracting particle's system the density of the interacting one. Especially in view of the multireference nature, i.e. qualitative failure of the one Slater-Determinant approach found for many excited states in the quantum chemistry community. The problems of v and n-representability arise again. Assuming that an exact $\nu_{KS}(\mathbf{r}, t)$ exists, we can write a time-dependent Kohn-Sham equation.

$$i\frac{\partial}{\partial t}\varphi_i(\mathbf{r}, t) = \left[-\frac{1}{2}\nabla^2 + \nu_{KS}[\rho, \Psi_0](\mathbf{r}, t)\right]\varphi_i(\mathbf{r}, t) \tag{3.125}$$

The Kohn-Sham potential is decomposed in the same way, as in ground state DFT, in a time-dependent external, Hartree and exchange-correlation potential.

$$\nu_{KS}[\rho, \Psi_0](\mathbf{r}, t) = \nu_{ext}(\mathbf{r}, t) + \int d^3\mathbf{r}' \frac{\rho'(\mathbf{r}', t)}{|\mathbf{r}' - \mathbf{r}|}\nu_{ext}[\rho, \Psi_0, \Psi_{0,KS}](\mathbf{r}, t) \tag{3.126}$$

The exchange-correlation potential depends on the initial Kohn-Sham state $\Psi_{0,KS}$ in addition to the initial quantum state. This is a new complication inherent in time dependent Kohn-Sham DFT. The initial Kohn-Sham state may be chosen because there is an infinitely large number of Slater determinants to produce a given density - and we do not possess a variational criterion. This greatly complicates the search for approximations to the time-dependent XC functional.

Most calculations on molecular systems are not interested in the true time-dependent behavior of the electrons, focussing either on static structures or the evolution of the adiabatically separated nuclear degrees of freedom. Excited states are most important where they are stationary and correspond to easily accessible UV/Vis data. It is therefore highly desirable to have a frequency dependent version of TD-DFT where the inital state is always the electronic ground state.

3.11.3 Linear response TD-DFT

A frequency dependent approximation to full TD-DFT is provided by linear response TD-DFT. The linear response formalism is based on the same concepts as encountered in the previous sections. The external potential in this case may be due to an electromagnetic wave, allowing the computation of optical excitation spectra. The first order change in the density $\rho^{(1)}(\mathbf{r},t)$ this time is obtained by a time-dependent linear response equation. For an introduction using such a function in classical thermodynamics and the connection to QM, see the book by Tuckerman.(31)

$$\rho^{(1)}(\mathbf{r},t) = \int_0^\infty dt' \int d^3\mathbf{r}' \chi(\mathbf{r}t,\mathbf{r}'t')\delta\nu_{ext}(\mathbf{r},t) \tag{3.127}$$

The response function $\chi(\mathbf{r}t,\mathbf{r}'t')$ can be written as

$$\chi(\mathbf{r}t,\mathbf{r}'t') = \left.\frac{\delta\rho(\mathbf{r},t)}{\delta\nu_{ext}(\mathbf{r}',t')}\right|_{\nu_{ext},0} \tag{3.128}$$

This time-dependent polarizability now has to be calculated using DFT. Writing the response in terms of Kohn-Sham noninteracting system and the change in the Kohn-Sham potential, one obtains

$$\rho^{(1)}(\mathbf{r},t) = \int_0^\infty dt' \int d^3\mathbf{r}' \chi_{KS}(\mathbf{r}t,\mathbf{r}'t')\delta\nu_{KS}(\mathbf{r},t) \tag{3.129}$$

The noninteracting Kohn-Sham system's linear response function χ_{KS} is written in the sum-over-states representation as

$$\chi_{KS}(\mathbf{r},\mathbf{r}',\omega) = \lim_{\eta\to 0^+}\sum_{k,j}(f_k - f_j)\delta_{\sigma_k\sigma_j}\frac{\varphi_k^{(0)*}(\mathbf{r})\varphi_j^{(0)}(\mathbf{r})\varphi_j^{(0)*}(\mathbf{r}')\varphi_k^{(0)}(\mathbf{r}')}{\omega-(\epsilon_j-\epsilon_k)+i\eta} \tag{3.130}$$

This result is obtained from time-dependent perturbation theory of the noninteracting many-body system. The response function has poles in the KS-eigenvalues. This corresponds to a frozen orbital approximation. This means that the change in the electrostatic and exchange-correlation potentials due to the density change is not taken into account. The true excitation energies have to account for this, so the integral in eq. 3.129 is to $\delta\nu_{KS}(\mathbf{r},t)$ instead of only the external potential. Let us begin by defining the response function of the exchange-correlation potential to a density change in linear order:

$$f_{XC}(\mathbf{r}t,\mathbf{r}'t') = \left.\frac{\delta\nu_{XC}(\mathbf{r},t)}{\delta\rho(\mathbf{r}',t')}\right|_{\rho=\rho^{(0)}} \tag{3.131}$$

Now the change in the KS potential may be written as

$$\delta\nu_{KS}(\mathbf{r},t) = \delta\nu_{ext}(\mathbf{r},t) + \int d^3\mathbf{r}'\frac{\rho^{(1)}(\mathbf{r}',t')}{|\mathbf{r}-\mathbf{r}'|} + \int dt'\int d^3\mathbf{r}' f_{XC}(\mathbf{r}t,\mathbf{r}'t')\rho^{(1)}(\mathbf{r}',t') \tag{3.132}$$

Expressing this in terms of the response functions themselves as well as setting eq. 3.127 and eq. 3.129 equal and substituting eq. 3.129 for $\rho^{(1)}$ one obtains after some algebra the Dyson equation of TD-DFT.

$$\begin{aligned}\chi(\mathbf{r}t,\mathbf{r}'t') = \chi_{KS}(\mathbf{r}t,\mathbf{r}'t') + \int dt_1\int d^3\mathbf{r_1}\int dt_2\int d^3\mathbf{r_2}\chi_{KS}(\mathbf{r}t,\mathbf{r}_1t_1)\\ \underbrace{\left[\frac{\delta(t_1-t_2)}{|\mathbf{r_1}-\mathbf{r_2}|}+f_{XC}(\mathbf{r}_2t_2,\mathbf{r}_1t_1)\right]}_{f_{HXC}}\chi_{KS}(\mathbf{r}t,\mathbf{r}'t')\end{aligned} \tag{3.133}$$

Note that the Hartree-exchange-correlation term depends only on Δt, allowing a formulation in terms of frequency ω. The equation may be expressed in the frequency domain as

$$\chi(\omega) = \chi_{KS}(\omega) + \chi_{KS}(\omega) * f_{HXC}(\omega) * \chi(\omega) \tag{3.134}$$

Where the stars denote convolution integrals and the position dependencies have been omitted. This equation allows the computation of the excitation energies. For the discrete spectrum, only the poles in ω have to be found (for a continuous response spectrum the full Dyson equation is necessary).(96) To allow practical computations, it is first recast into an eigenvalue equation, where the eigenvalues $\lambda(\omega)$ have to be one at the poles:

$$\chi_{KS}(\omega) * f_{HXC}(\omega) * \epsilon(\omega) = \lambda(\omega)\epsilon(\omega) \tag{3.135}$$

For a transition q, there exists a transition density Φ_q and a Kohn-Sham energy difference ω_q (compare eq. 3.130)

$$\Phi_q = \varphi_j^*(\mathbf{r})\varphi_k(\mathbf{r});\ \omega_q = \epsilon_k - \epsilon_j \tag{3.136}$$

Having introduced these quantities and writing eq. 3.135 in terms of orbitals it may be rewritten as a matrix eigenvalue equation, the famous Casida equation.(97)

$$\mathbf{R}\mathbf{F}_I = \Omega_I^2\mathbf{F}_I \tag{3.137}$$

Here the $\mathbf{F}_I$ are eigenvectors, which can also be used to compute the oscillator strength, Ω_I the excitation energies and the matrix elements of $\mathbf{R}$ are

$$R_{qq'} = \omega_q\delta_{qq'} + 4\sqrt{\omega_q\omega_q'}\int d^3\mathbf{r}\int d^3\mathbf{r}'\Phi_q(\mathbf{r})f_{HXC}(\mathbf{r},\mathbf{r}',\Omega_I)\Phi_q'(\mathbf{r}') \tag{3.138}$$

It is now possible to compute molecular excitation spectra using matrix-eigenvalue solving algorithms such as Lanczos and Davidson diagonalization routines. The well known Tamm-Dancoff approximation consists of setting to zero the backward transitions, found in the $\mathbf{R}$ matrix at $q' = -q$. It is often more numerically stable than ordinary TD-DFT, because triplet instabilities and the like have a smaller impact.(98) However, the oscillator strengths can be shown not to follow the sum rule, as is the case with full linear response TD-DFT.

Approximations - ALDA, AGGA

Having described the exact linear response scheme for TD-DFT, we should now take a second look at f_{XC}, the response function of the exchange-correlation potential. As a time-dependent response function in principle it incorporates its own time evolution

(written above in terms of the frequency). This is almost always neglected in practice. Instead simple ground state functionals are being used, in a so called "adiabatic" approximation. In this approximation the XC-functional is not time-dependent but simply the same as the ground state functional applied to the time-dependent density.

$$\nu_{XC}^{adia}[\rho](\mathbf{r},t) = \nu_{XC}^{GS}[\rho(t)](\mathbf{r}) \tag{3.139}$$

The usual ground state DFT functionals (LDA, GGA, etc.) may now be used without any further adaptions. For the response function this means

$$f_{XC}^{adia}[\rho_0](\mathbf{r}t,\mathbf{r}'t) = \delta(t-t')\frac{\delta^2 E_{XC}[\rho]}{\delta\rho(\mathbf{r})\delta\rho(\mathbf{r}')}\bigg|_{\rho_0} \tag{3.140}$$

This is a highly questionable approximation, because it implies a zero frequency limit. It is not clear that the excited state density and wavefunction can be represented by a system in the ground state. Nevertheless it often works well in practice. One major reason are various boundary conditions which are trivially fulfilled in the adiabatic limit. The pure KS-orbital energies are often already a reasonable approximation, so that the success of the adiabatic local density approximation (ALDA) methods is put in perspective. In the adiabatic limit the response Kernel used in DFPT is recovered. The second functional derivative of E_{XC} is normally evaluated by finite difference methods, especially in the case of more complex functionals.

3.12 Ab-initio molecular dynamics

Molecular dynamics using DFT is challenging, because within the Born-Oppenheimer approximation the Kohn-Sham wavefunction Ψ parametrically depends on the nuclei, therefore one has to solve the electronic structure problem in every step. On the other hand gradients are readily available by the Hellmann-Feynman theorem, so that a converged KS-wavefunction provides the forces to propagate the system:

$$\mathbf{F}_k = -\langle\Psi_0 \mid \frac{\partial\hat{H}}{\partial\mathbf{R}_k} \mid \Psi_0\rangle \tag{3.141}$$

This setup, where the force $\mathbf{F}_k$ on the nucleus k is computed from the ground state orbitals is known as Born-Oppenheimer MD (BOMD). The first computationally efficient scheme for DFT-molecular dynamics was developed by Car and Parrinello

(CPMD).(99) Via an extended Lagrangian approach, they introduced a fictitious dynamic of the orbitals, treating them as particles with large masses. This allows to propagate them simultaneously with the system, without a SCF calculation. Very good energy conservation can be achieved, provided the timestep is small enough to keep the orbitals near the BO minimum. The need to keep the timestep small has lead to a resurgence of interest in BOMD, where the timestep may be chosen larger, provided the SCF is tightly converged. The renewed interest in BOMD simulations stems from the use of improved SCF schemes, as well as special predictors that will extrapolate the wavefunction in the next MD step from previous steps. In the very efficent CP2K code(80) various SCF schemes are possible, most notably the orbital transform method(100, 101) Instead of propagating the orbitals by a fictitious dynamic, their evolution is predicted by e.g. the Always-Stable-Predictor-Corrector (ASPC) method, where information from past steps is used to predict the new orbital coefficients in a polynomial expansion.(102, 103) The increased timestep possible for BO calculations now compensates the "lost" time for SCF convergence. For a detailed discussion of the two approaches see.(104) In an ab-initio MD simulation of water, the liquid is represented by means of a simulation box which is periodically repeated in every direction (periodic boundary conditions) and which contains between 50 and 500 independent water molecules. During an ab-initio molecular dynamics simulation, all orbitals of all molecules are recomputed at each step in the trajectory.

4

Overview over the published papers

Since the beginnings of physical chemistry, water has been a focus of experimental as well as theoretical research. Its abundance and importance to life are not the only reasons for this continuing interest. Water has also a rich set of anomalies, which set it apart from most other solvents. The best known example is perhaps the density anomaly of ice vs. liquid water. At the heart of many of the special properties of water lies cooperative hydrogen bonding and the tetrahedral structure that results from it.(11, 105) When this structure is perturbed or the hydrogen bond network cannot fully form, e.g. due to confinement, water can drastically change its properties.(106, 107, 108) As these influences on water are present in the cell and in fact are ubiquitous on earth, they play a role in a wide variety of phenomena from protein folding to chemical reactivity.(109, 110, 111, 112) The papers of this cumulative thesis all deal with aqueous solvation. However, two fundamentally different approaches have been taken. In the first project the focus is on a probe molecule, which allows to monitor its local environment indirectly. The second project directly investigates the effect of interfaces and ions on the water structure and H-bond dynamics.

4.1 Excited state solvation of a probe molecule

Using ab-initio methods to describe the nonequilibrium excited state solvation dynamics of a probe molecule in aqueous solution was a main goal of this thesis. These solvation

dynamics are experimentally available through the time-dependent Stokes shift (TDSS), as measured by femtosecond pump-probe fluorescence spectroscopy.(113, 114) At room temperature, the relaxation process takes merely a few picoseconds - making this a fortunate case, where the timescale of ab-initio MD and experiment coincide. The probe molecule used in this work is *N*-methyl-6-oxyquinolinium betaine (MQ).

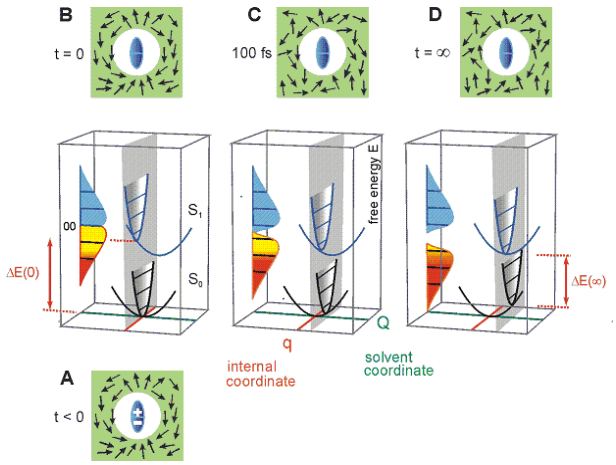

Figure 4.1: Image taken from ref. (114). Reprinted with permission from Wiley. Schematic illustration of the excited state solvation of MQ, solvent disorder increases after the chromophore dipole moment is reduced by electronic excitation. The time-dependent solvation can be monitored by the Stokes shift.

As can be seen in Fig 4.1, electronic excitation leads to a decrease in the dipole moment of the chromophore, which induces a change in the averaged solvent conformation. This solvent response to a change in the electric field can be modeled by a reaction field, which represents the solvent as a polarized dielectric continuum. The theory is described in more detail in e.g. the book by Nitzan(115). It is known, that for a suitable chromophore, the time-dependent fluorescence can be connected with the experimental permittivity spectrum of water via this reaction field approach.(116) Continuum solvation was also successully used by Ernsting and coworkers to model MQ's TDSS data.(114, 117, 118) MQ's experimental time-dependent Stokes shift therefore gives access to the local permittivity spectrum in the THz range. This is why the chromophore may be considered a local spectrometer.

While the dielectric solvation model is very useful, there are several problems associated with it in practice: Its simplest version will work only for a medium which is

isotropic, and for which MQ is solvated in a sufficiently "nonspecific" way, so that the continuum response to a change in the chromophore dipole satisfactorily describes the solvation dynamics. In order to obtain localized information in more complex environments the solvation dynamics have to be described in a more general framework, which is able to describe solvation on an atomistic level. Ideally such an approach should include electronic polarizability and should be parameter free. One possible example for its application would be a protein, into which MQ might be inserted to replace e.g. the indole moiety of tryptophane.

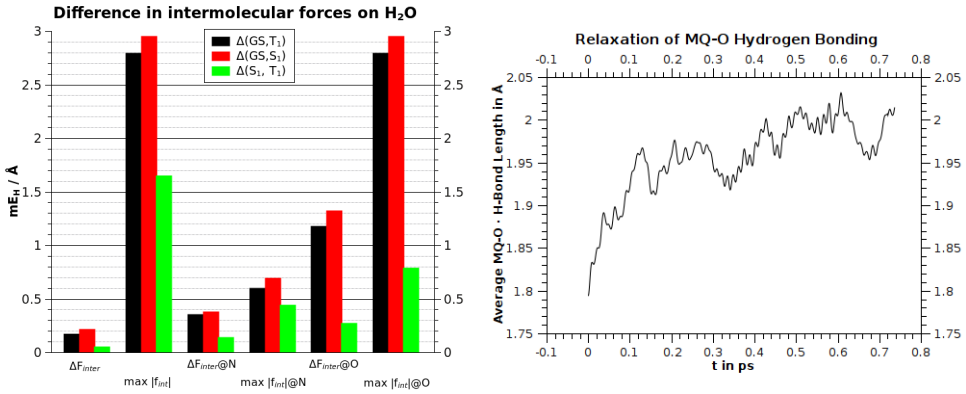

Figure 4.2: Left: Comparison of average intermolecular force and maximum force around MQ for all H_2O, at the nitrogen ΔF_{inter}@N and oxygen atom ΔF_{inter}@O of MQ, comparing the ground state (GS) with TD-DFT S_1 and the triplet model of the excited state.(1) Right: Time evolution of the average MQ - H_2O H-bond length in the T_1 state after excitation at t=0.(4)

To obtain a viable approach to excited state solvation, the interactions of the chromophore with the environment have to be accurately represented in ground and fluorescent excited state. As the MQ $S_0 \rightarrow S_1$ excitation has a charge-transfer character, this is nontrivial. The first step in this project, was therefore to apply a range of DFT functionals and benchmark quantum chemical methods to check whether specific interactions, such as changes in H-bonding to MQ and the change in the dipole moment can be described in an efficient and accurate way. It was found that H-bonding at the MQ-oxygen terminus is weakened by electronic excitation and that the change in the dipole moment of MQ is considerable even in the gas phase.(1) Interestingly, it was possible to accurately describe this using the DFT T_1 state in place of a high-level S_1 state. On the

left side of Fig. 4.2, the effective forces on H_2O molecules in the condensed phase are compared between TD-DFT S_1 and the T_1 state, showing their similarity. In both cases a large change of forces at the H_2O molecules hydrogen bonded to the MQ-oxygen is triggered by the excitation. Simulating the relaxation, the effect on H-bonding was also apparent in the H-bond length (Fig. 4.2, right). The time-dependent fluorescence was then computed on an ensemble of T_1 trajectories. For the simulation of the fluorescence experiment, TD-DFT was used to compute the $S_0 \rightarrow S_1$ transition energies. As can be seen in Fig. 4.3, the simulation resulted in good agreement with experiment. The dynamic fluorescence could be accurately modeled, only the equilibrium fluorescence wavelength had to be adjusted, which was attributed to the difference between S_1 and T_1 chromophore equilibrium geometries.

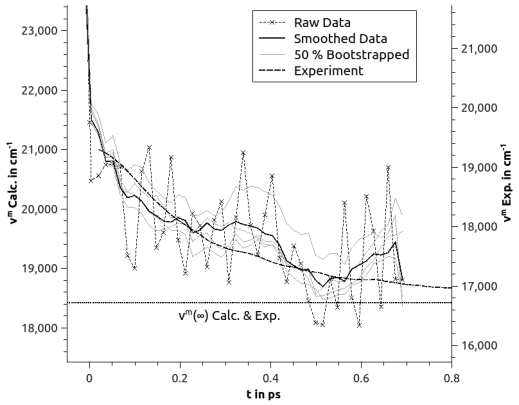

Figure 4.3: Dynamics of the Stokes shift as obtained from averaging ten trajectories and smoothed by 10 pt moving window averaging (black, left axis), Stokes shift after removal of 5 random trajectories (grey, left axis), experimental data(119) (dashed line,right axis) data is referenced to $\nu(t = \infty)$ in both cases (dotted line).(4)

The experimental Stokes shift could then be decomposed into molecular components. No significant contribution to the fluorescence relaxation behavior by the chromophore itself was found. This allowed to rewrite the contribution in terms of the solvation energy difference. The environment around MQ was then decomposed into different parts (see Fig. 4.4).

It was found that the water molecules which interact strongly with the dipole field of MQ have a significant contribution to the relaxation, in agreement with dipolar relaxation models (see Fig. 4.4). The effect of the reduction of the solvent dipole could

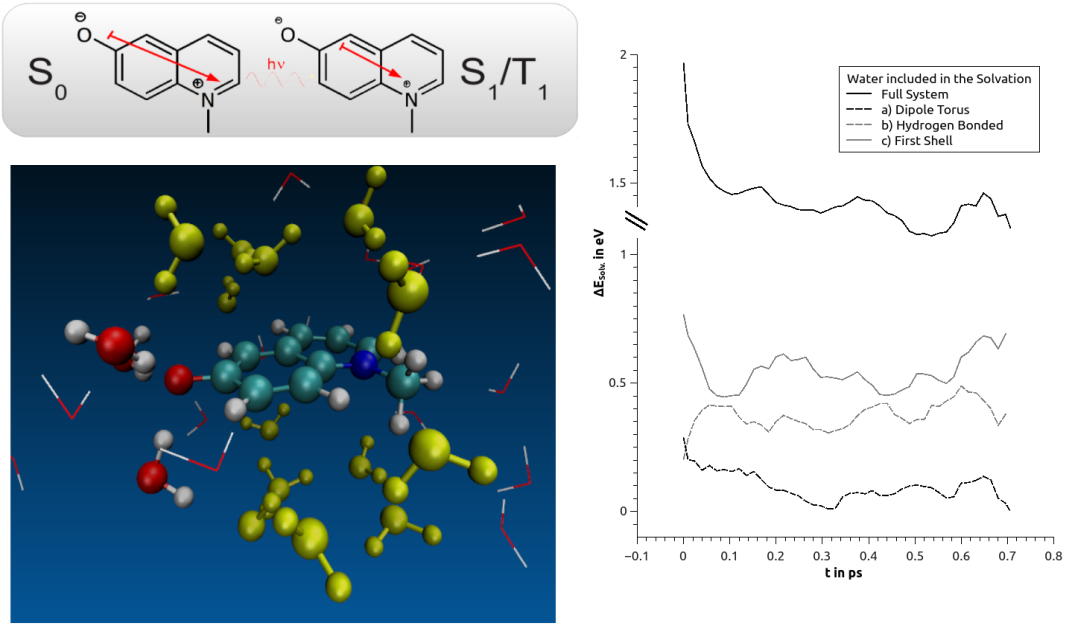

Figure 4.4: Left: The first solvation shell of MQ and its components: Water molecules in torus around N-O (yellow beads,a), H_2O molecules hydrogen bonded to the MQ-oxygen terminus (beads,b), and entire first solvation shell (sticks,c). Right: Computed time evolution of the solvation energy $\Delta E_{Solv}(t)$ for the three clusters around MQ, for the subsystems extracted from the fully solvated MQ trajectory.(4)

also be quantified with the help of an order parameter. No significant contribution to the relaxation was obtained from the H-bonded H_2O molecules, as is also shown in Fig. 4.4. In addition it was found, that in order to obtain the full solvation energy, at least 8 Å of water have to be included in the simulation box. The probe molecule therefore is influenced by more than the first solvation shell, thus giving experimentalists information about the range and region of their measurements. Summarizing, the time-dependent excited state solvation properties of MQ could be well reproduced and could be decomposed into to regional and molecular contributions. The approach used was ab-initio in the sense that it does not require to introduce any parameters. Therefore, it is easily transferable and may be used in the future to help interpreting Stokes-shift experiments in complex environments. The use of ab-initio water and TD-DFT excitations instead of electrostatic solvation energy differences complements the more

empirical approaches known in the literature.(113, 120)

4.2 Effects of ions and interfaces on hydrogen bonding

The equilibrium properties of water have long been a focus of ab-initio molecular dynamics studies.(9, 17, 20, 121, 122) In order to understand why, the systems studied in these work are instructive examples. The first group of systems are aqueous solutions of LiI. Nonpolarizable classical forcefields have been shown to give flawed descriptions of aqueous salt solutions in many cases, leading to unphysical clustering of the ions.(123, 124) New results from THz spectroscopy, as well as time-dependent infrared spectroscopy reraise the question how far the hydrogen bonding network of the bulk solution is affected by the presence of ions.(125, 126, 127, 128) For the description of the interaction between the hydrogen bonding network and ions, therefore ab-initio methods are necessary to give an accurate description. As can be seen from the left side of Fig. 4.5, the formation of a tetrahedral coordination shell at Li^+ as well as hydrogen bonding to I^- occurs spontaneously in the simulation. Another system considered was water confined between two silica interfaces. Water in amorphous silica confinement is widely known to have significantly different properties from bulk water.(129, 130) Previously experimentally inaccessible metastable phases of water(131) have been reported to exist in this type of confinement.(132, 133) Changes to the hydrogen bond network at the interface are crucial to give an accurate representation of the changes in structure and dynamics that accompany strong confinement.

As polarizability is included in the DFT description, also indirect effects on hydrogen bonding, such as reinforcement by polarization of coordinated water molecules e.g. in a Li^+ shell could be quantified.(5) This effect is accessible experimentally from NMR chemical shift measurements. A strong relation between instantaneous ^1H chemical shifts and the hydrogen bond length exists, and may be used to verify that a correct description of the hydrogen bond network has been obtained. Therefore, NMR shifts have been a main tool in this work's investigations into equilibrium solvation. While insight from NMR experiments are typically constrained by the timescale of measurement, the availability of the electronic structure allows to compute the instantaneous NMR chemical shifts. These were computed from snapshots of the trajectory and can be used to decompose the experimental NMR proton chemical shift spectrum. The

simulation of a LiI solution shows, how iodine and lithium influence proton NMR shifts in their immediate vicinity (see Fig. 4.5, right). Experimentally, only the bulk value is accessible - and can be reconstructed from the averages. As in experiment, it was found that increasing the concentration of LiI decreases the bulk chemical shift. The decomposition allowed to localize this effect at the immediate vicinity of the ions. The size of the I^- ions ensured that at high concentration, there are several ions in close vicinity of a given H_2O, which have a combined effect.(5)

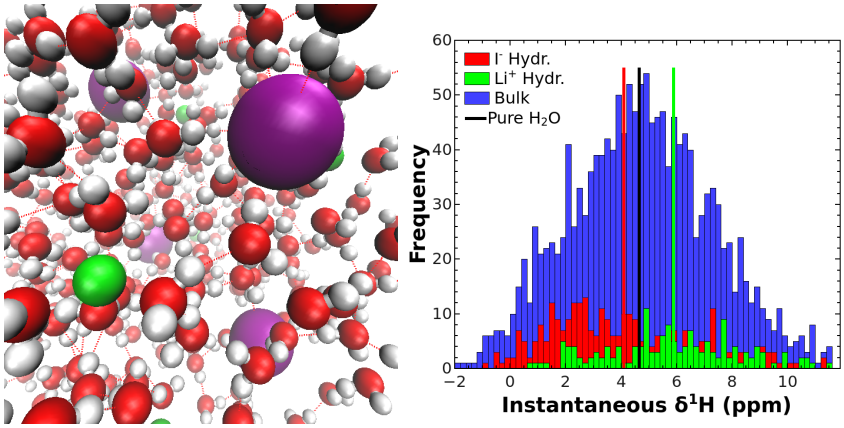

Figure 4.5: Left: Snapshot from a simulation of an 1M aqueous solution on LiI. Li^+ ions are colored green, I^- ions are colored red, characteristic solvation shells are visible.(3) Right: Chemical shift distribution for hydrating water and bulk water in the LiI 1M solution. The average for pure water is marked with a black line, while the chemical shift average of lithium and iodine hydration water is marked with the red and green line, respectively.(5)

Another system in which this approach has been used was water at a silica interface. The silica interface was modeled by silicic acid groups embedded in a reflective potential (see Fig. 4.6, left). This system served as a model for water confined in mesoporous silica of the type of e.g. MCM-41. The H-bonding at the model interface has been investigated by ^1H chemical shift calculations. The shifts show a drastic weakening of water H-bonding near the interface, while in the middle of the pore normal bulk H-bonding is recovered. Results show that the effect on H-bonding of this silica wall becomes very small after 4 Å (see Fig. 4.6, right). Besides chemical shifts, also more sophisticated NMR experiments can be reproduced and analyzed using ab-initio methods. One example is the computation of T_1 relaxation times(134), another

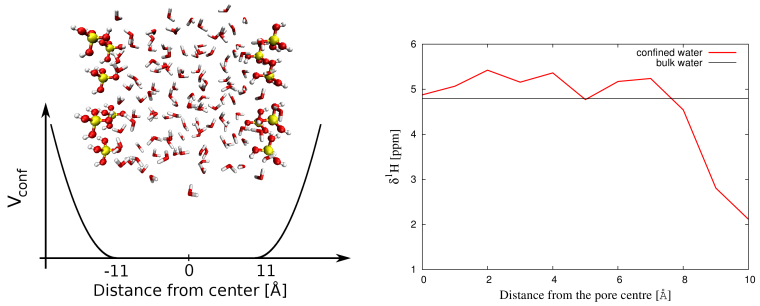

Figure 4.6: Left: Model silica interface consisting of silicic acid groups with constrained oxygens and a quadratic reflective potential. Right: ^{1}H chemical shift averages as a function of the distance from the interface.(2)

is the simulation of solid state NMR lineshapes.(135) NMR parameters obtained from ab-initio simulations are highly accurate and have been helpful in the elucidation of e.g. supramolecular structures.(136, 137, 138) Computing spectroscopic observables is an important tool to establish the correspondence with experiment. However, the MD trajectories contain structural and dynamical information beyond what has been measured by the spectroscopic experiment. In the case of the LiI solutions, the trajectories revealed a form of clustering in the 9 M solution (see Fig. 4.7, right). At this concentration Li^+ ions were found to be linked by water bridges, resulting the formation of clusters and in a deformation of the individual Li^+ solvation shells. The occurrence of water bridging had been proposed already from diffraction experiments and similar structures are present in the cristalline trihydrate.(139, 140) The length distribution and structure of the clusters found at 9 M concentration was also quantified by the MD-simulations in this work.

Furthermore, through a decomposition of the H-bond network it was possible to quantify how the presence of ions affects the relative stability of H-bonds in the network. In order to achieve this, the H-bond network was represented as a graph. Via a suitable autocorrelation function, the decay of the H-bond network was analyzed. It was found, that iodide has a destabilizing effect across several H-bonds in the H-bond network graph, while Li^+ has a competing, stabilizing effect (see Fig. 4.7, left). For a detailed description, see paper (5). Similar interactions between ions in aqueous solutions on the dynamics have already been observed by IR-spectroscopy.(126)

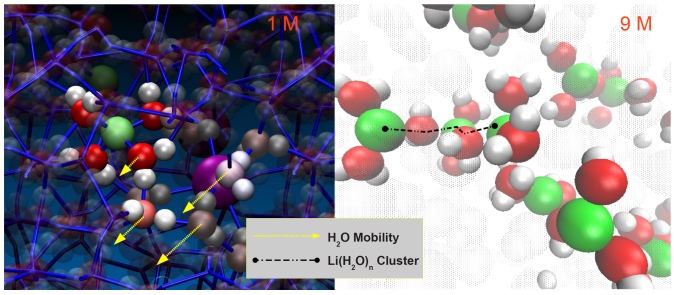

Figure 4.7: Schematic illustration of the structural and dynamics effects in LiI solutions. Left: At intermediate concentration H-bond stability is affected in opposing ways by cation and anion. Right: Lithium iodide displays clustering at high concentration.(5)

5

Thesis Papers

5.1 Paper I

PCCP

Cite this: *Phys. Chem. Chem. Phys.*, 2011, **13**, 16395–16403

www.rsc.org/pccp

PAPER

Approaches to the solvation of the molecular probe *N*-methyl-6-quinolone in its excited state

Christoph Allolio and Daniel Sebastiani*

Received 8th April 2011, Accepted 25th July 2011
DOI: 10.1039/c1cp21110b

The molecular probe *N*-methyl-6-quinolone (MQ) gives experimental access to its local chemical environment, *e.g.* inside a biomolecule. Using *ab initio* molecular dynamics (MD), it is possible to simulate the time evolution of the Stokes shift as a function of the actual atomistic coupling to the surrounding hydrogen bond network and thus obtain a comprehensive view of the local environment. In contrast to ground state *ab initio* MD simulations, the choice of a method for excited state MD is nontrivial. Here, we develop a simple and accurate model for the solvation dynamics of MQ in its first excited state.

1 Introduction

Water is essential to all life on this planet. Its abundancy and its remarkable properties have ensured that it is also the most thoroughly examined liquid.[1–11] Despite all efforts, its biophysical properties have not yet been understood completely. Specifically, spectroscopic experiments have shown that a geometric confinement has a drastic effect on several of its properties making it different from water in the bulk phase (see reviews[12–14]). A particular case in point are biological confinements: the functionality of many proteins depends on these changed, local properties of water.[15–18] In order to understand protein folding[19] or even the stability of DNA,[20] it is necessary to understand the local structure and dynamics of water, especially as a solvent and beyond its standard state.[21,22] There are numerous experimental and computational methods which are able to characterize structural and dynamical properties of hydrogen bonded liquids and networks,[21,23–33] but most of them work on timescales that are considerably longer than those of the typical molecular motion of individual water molecules.

Terahertz spectroscopy is a useful tool to measure the fluctuations of the hydrogen bonding network *via* its dielectric response.[34,35] On the experimental side in order to yield site specific local data, this approach can be combined with the use of a molecular probe, typically a fluorescent dye.[36–38] *N*-Methyl-6-quinolone (MQ) has been used as such a probe for the local terahertz spectrum of water and other polar solvents.[39,40] Recent results have extended its application to biochemical environments.[41] It is especially attractive for this purpose, because of its small size, which allows an insertion into DNA or proteins (replacing tryptophan or nucleic acids). Spectroscopically, MQ is interesting because it has no net charge and is a rigid molecule. It will therefore not interfere with the relevant vibrational modes of water.[39] In order to obtain the local THz spectrum the time dependent Stokes shift (TDSS) is measured by femtosecond spectroscopy, using a pump–supercontinuum probe setup. On the theoretical level the experimentally obtained TDSS data have only been discussed in terms of continuum dipolar relaxation theory.[39–41]

Ideally, it should be possible to extract information about the local structure and dynamics around the molecular probe in atomistic detail. *Ab initio* molecular dynamics (MD) allows us to simulate the full experiment without preadjusted parameters, and obtain a comprehensive view of the local environment.[42] In particular the interplay of the molecular structure, dynamic aqueous solvation and the effect of electronic excitation can be modeled consistently within a common first-principles based theory.[24,43–47] However, excited state electronic structure calculations are less numerically reliable and involve higher computational cost than the corresponding ground state calculations. In contrast to the ground state *ab initio* MD simulations, the choice of a method is therefore nontrivial. There exist two main problems: first the need for a correct description of the excited state surface within the Born–Oppenheimer approximation. For this purpose very accurate approaches exist: Full-CI, CASPT2, GW and Coupled Cluster descriptions can be considered reliable reference methods. Their high accuracy comes at the expense of computational effort and drastically limits the system size. More affordable methods for treating the excited state range from perturbation theory inspired methods like time dependent (TD)-DFT,[48] *via* empirical DFT approaches like ROKS[49] or ROSS,[50] to semi-empirical CI.[51] Especially TD-DFT is now widely used,[52–55] despite the known problems when treating charge transfer states.[56–58]

The other main problem with excited state MD arises when potential surfaces approach at so called conical intersections: the adiabatic approximation fails and semiclassical molecular

Physics Department, Freie Universität Berlin, Arnimallee 14, 14195 Berlin, Germany. E-mail: daniel.sebastiani@fu-berlin.de; Fax: +49 (0)30 838 51355

dynamics is not sufficient anymore. Different ways to solve this problem have been proposed (for a recent review see ref. 59). One possibility for example is to introduce explicit time dependency for the nuclei into the CASSCF framework.[60] All these methods share a high computational cost further limiting the system size and simulation time. We aim to find a model for the excited state, which is capable of providing insights into complex hydrogen bonding dynamics. As the relaxation of the hydrogen bonding network occurs on a picosecond timescale, a computationally affordable method is required. However, the more approximate a method, the more it has to be validated for the particular system in view. Here this is ensured by comparison of different approaches to the excited state with accurate correlated methods. We aim to show that reasonable accuracy of the excited state PES can be achieved with approximate methods.

2 Computational details

2.1 MQ and its molecular clusters

We have computed vertical excitation energies of the free and hydrated MQ molecule, considering clusters of one MQ with zero, one and four water molecules. We chose the well-known BLYP[61,62] GGA DFT functional, with and without dispersion correction,[63] and the Hartree–Fock (HF) exchange corrected hybrid functional PBE0.[64] Hybrid DFT was used successfully in a previous study to calculate MQ ground state geometries and NMR shifts,[65] which is why we use hybrid DFT reference geometries. The PBE0 functional specifically is known to give accurate uncorrected excitation energies in comparison with most of other hybrid DFT functionals for a wide variety of organic dyes.[66] Additionally, we compare the results of the post-HF methods such as configuration interaction (CIS), perturbation theory (MP2) and coupled cluster (CCSD, CCSD(T)). Excited states were calculated using TD-DFT, CIS and the ROKS functional. The excited state (ES) reference method was equations of motion coupled cluster theory (EOM-CCSD, reviewed in ref. 67), the ground state (GS) reference method was CCSD(T). For the localized basis set methods a triple-ζ Pople 6-311G**[68] basis set was employed. Additionally the basis set was augmented with standard diffuse functions on both the heavy and the hydrogen atoms (a) or only on heavy atoms (b). All post-HF calculations as well as PBE0-TD-DFT were done using frozen atomic core orbitals, unless mentioned otherwise. The BLYP-D TD-DFT results also make use of the Tamm–Dancoff approximation (TDA). For the ROKS calculations the modified Goedecker–Umrigar[69] algorithm was employed.[70] Plane wave calculations were done using Troullier–Martins pseudopotentials,[71] single point calculations always had a plane wave cutoff of 140 Ry, results obtained with this method are marked with (c). The computer codes used for the calculations were: Gaussian09,[72] Gaussian03,[73] NWChem 6.0,[74] CPMD 3.13,[75] CP2K,[76] MOPAC,[77] Molpro 2006.1[78] and Orca 2.7.[79]

2.2 Molecular dynamics of MQ

In order to extend the scope of this study to conformations beyond the equilibrium geometries, we have performed a short Car–Parrinello molecular dynamics simulation of a fully hydrated MQ molecule. To this purpose CPMD simulations were done with a cutoff of 70 Ry, a fictitious electron mass of 800 a.u. and a time step of 5 a.u. They were conducted in an NVT ensemble using a Nosé–Hoover thermostat with a coupling constant of 2500 cm^{-1}, at a temperature of 298.15 K, to closely emulate experimental conditions.[40] The molecular dynamics were done in a cubic, periodic box with a side length of about 16.06 Å. The MQ molecule was inserted by calculating the molecular volume of the overlapping Van der Waals radii of its atoms and removing the equivalent volume of water molecules calculated in the same way. This approach results in a box with MQ and 130 H_2O at a density of $d = 1.00$ g cm^{-3}. MQ concentration is still 80 times higher than a typical experimental concentration of 5×10^{-3} M.[40] Molecular dynamics was conducted for a total duration of 10 ps.

3 Results and discussion

3.1 MQ vertical electronic excitation and Stokes shift of isolated MQ

3.1.1 Vertical electronic excitation of isolated MQ. As a first step we compare excitation energies and dipole moments of isolated MQ. A decrease in dipole moment from the ground to excited states (see Fig. 1) is experimentally known to be the determining factor in excited state solvation dynamics.[39] This decrease in dipole moment will lead to increased disorder of the solvation shell. The resulting relaxation dynamics form the basis of the THz spectroscopic measurement. Therefore comparing dipoles may serve as a first test of the accuracy of the different models. For MQ the geometry obtained with the PBE0[b] level of theory was chosen as the reference geometry. It was optimized without constraints and verified to be a minimum by a frequency calculation. For this geometry, vertical excitation energies and ground and excited state dipole moments were calculated. The excitation energies are compared to EOM-CCSD/6-311G** reference values and a CASSCF/cc-pVTZ[41] calculation taken from the literature. The excitation energy was also computed on the EOM-CCSD/cc-pVTZ level of theory without frozen cores, yielding a deviation of only 0.01 eV from the frozen core/Pople basis set results. For the TD-DFT and CIS results the first ten excited states were calculated. Generally the first excited state with $f > 0.01$ was chosen as the reference state for the excitation energy. For PBE0[b], CIS[b], BLYP[a] and EOM-CCSD the HOMO/LUMO transition had the largest contribution to the excited state. Using BLYP we found the lowest excitation to have zero oscillator strength. The BLYP[a] dark S_1 state is a pure HOMO-1/LUMO transition and lies at 1.40 eV.

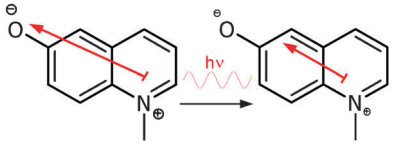

Fig. 1 Schematic illustration of the reduction of the dipole moment of *N*-methyl-6-quinolone: the effect of electronic excitation on the dipole moment.

When using the larger cc-pVTZ basis set as well as a 6-31G* basis the S_1 state stays dark. Therefore data are given for the S_2 excited state. For the other methods, the S_1 state is the state of interest. As the S_1 state is largely the result of a HOMO/LUMO transition, more empirical DFT approaches were also considered. For reasons of computational efficiency we used the BLYP functional for these. We calculated the relevant properties for the BLYP-LSD triplet state (T_1), which we expect to behave similarly to the S_1 state. The same assumption is already contained implicitly in the successful singlet excited state ROKS model.[49] We do not expect to obtain accurate excitation energies using the T_1 or the ROKS model, for these cases our focus will be on the more important excited state dipole moment.

The calculated excitation energies in Table 1 are redshifted in comparison with the experimental value of 3.04 eV (measured in H_2O).[80] This is not surprising since due to its zwitterionic nature MQ is known to show strong negative solvatochromism, so that in dry pyridine the absorption maximum is at 2.34 eV—far closer to gas phase benchmark values.[80] The results for the gas phase calculations of ground state dipole moments are in good agreement for all methods, with the unsurprising exception of HF theory. However in the excited state, the DFT based methods predict a smaller decrease in dipole moment than the wavefunction based methods. The DFT results are consistent; the comparatively smaller change in dipole moment is not specific to TD-DFT, but also affects ROKS and the T_1 approximation. While the agreement is far from perfect, the DFT dipole moments are actually higher than the benchmark values. This is exactly the opposite of what one would expect to observe in the case of an overdelocalization issue.

The excitation energy obtained with the PBE0 functional is between the two benchmark values, so there is no indication of a general TD-DFT failure. There is also a significant difference in the CASSCF(12,11) *vs.* the EOM-CCSD benchmark excitation energies. We note that EOM-CCSD energies were shown to be in good agreement with the CASPT2 energies in a benchmark study,[81] whereas CASSCF excitation energies are not as accurate. Another practical advantage of the EOM-CCSD method is the inherent size consistency, which is not guaranteed for MRCI or even CASPT2.[82]

3.1.2 Population analysis. In order to gain further insights into the nature of the excited state, we did a population analysis with Mulliken charges on the ground- and excited state relaxed densities. The results are shown in Table 2. In the ground state we find a positive partial charge of 1.2 e in the pyridinium part of the MQ system (ring B), with a corresponding negative partial charge in the phenyl ring (ring A). Both formal charges of the zwitterion are therefore delocalized.

Table 2 Mulliken charges for ground and excited states in elementary charges

Partial Charge	MQ-O	Ring A	Ring B	MQ-N
BLYP[a] q GS	−0.35	−0.84	1.18	0.26
TD-BLYP[a] Δq S_2	0.08	0.04	−0.13	0.01
BLYP[a] Δq T_1	0.10	0.06	−0.15	−0.01
PBE0[a] q GS	−0.38	−0.88	1.27	0.35
TD-PBE0[b] Δq S_1	0.09	−0.05	−0.03	−0.08

In all models we find that a negative partial charge of around 0.1 e is transferred from the MQ-oxygen upon excitation, and the net charge is transferred to the pyridinium part of the MQ π-system. We also find that when using the BLYP[a] level of theory, another major source of electron donation (0.7 e) is a C atom at the *ortho* position of the MQ-oxygen (see Fig. 2). In this case, excitation leads to a net positive polarization of the phenyl ring of the MQ system. Overall we find little charge transfer with density functional methods, with the total moved charge being less than half an electron. There are differences in the partial charges inside the π-system, depending on the applied partitioning scheme, *i.e.* Mulliken analysis consistently assigns partial charges of absolute value greater than one to the bridging atoms, which could not be reproduced by either NPA[83] or Löwdin analysis. Also, the partial charge transfer to the MQ-N atom varies between +0.01e (Mulliken TD-BLYP[a] ES) to −0.9 e (NPA BLYP[a] T_1). By summing up partial charges on the aromatic rings and distributing the partial charge of the bridging atoms equally we are able to maintain a consistent picture across partitioning schemes.

3.1.3 Relaxed geometries of MQ in the ground and excited states. To check whether the good agreement of DFT dipole moments really corresponds to a similar description of the electronic structure, the geometry of MQ was optimized in the ground state and in the target excited state. This allows us to compare the change of the π system in the excited state and look for large structural differences between models. Table 3 contains selected bond lengths and angles.

We find that all DFT based excited state models lead to a qualitatively similar change in the MQ bonding pattern. In particular the ROKS S_1 and the triplet state are in close mutual agreement. However, the methods differ in the quantitative distribution of charge among bonds inside the π system. It is remarkable that the $C_{[6]}$–$O_{[11]}$ bond is slightly elongated in the excited state by all the tested DFT-based methods in the gas phase. This directly contradicts the idea of a charge transfer/delocalization of an oxygen lone pair into the π system. It is noteworthy that the admixture of exact exchange (PBE0) also confirms this conclusion.

Table 1 MQ vertical excitation energies in eV and dipole moments in Debye

Level of theory Method ES	BLYP[a] TD-DFT	BLYP[a] T_1 (LSD)	BLYP[c] ROKS	PBE0[b] TD-DFT	HF[a] CIS	CASSCF[41] CASSCF	CCSD EOM
Excitation energy	1.83	1.34	1.74	2.11	2.96	2.0	2.37
Dipole moment GS	10.2	10.2	10.0	10.8	12.3	10.5	10.3
Dipole moment ES	7.4	6.8	6.8	7.3	7.6	5.8	5.1[a]

Here full linear response TD-DFT results are reported for BLYP, later we use TDA.[a] EOM-CCSD/6-31G*.

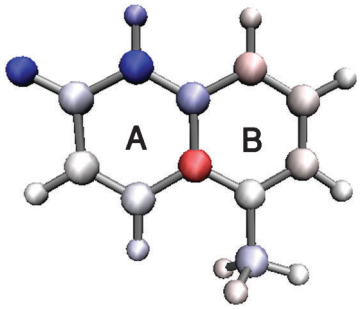

Fig. 2 Change in partial charges when going from the BLYP[a] ground state to the triplet state negative charges Δq (red) and positive charges (blue).

3.1.4 Calculation of the Stokes shift in the gas phase. Having obtained the relaxed structures in the ground and in the excited state, we can calculate the energy difference between the ground state geometry and the relaxed geometry, using the excited state PES in both cases. This intramolecular relaxation energy serves to compare different excited state hypersurfaces. From the geometries, we have seen that the different DFT-based approaches result in minima at similar structures. We would like to know whether they are also consistent in their energetics. From the difference in vertical excitation energy at the ground state geometry and the excited state geometry we can also calculate a gas phase stationary Stokes shift. This in turn allows us to see how far the excited state geometry is away from the minimum on the ground state PES. The experimental value for the difference between absorption[80] and fluorescence maximum[39] is 1.0 eV in H_2O. The stationary Stokes shift due to solvation was given as 0.38 eV.[39] This value is obtained by monitoring the emission maximum of the S_1 state in solution over time, and then extrapolating it to $t = 0$. As a first estimate of intramolecular relaxation in the excited state one may therefore expect a gas phase Stokes Shift of about 0.6 eV. This implies the drastic assumption of a fast, uncoupled, intramolecular vibrational relaxation unaffected by the solvent, followed by slow intermolecular solvent relaxation.

We find that the gas phase Stokes shifts in Table 4 are around 0.4–0.7 eV, which is twice the computed intramolecular relaxation energy in the excited state (0.2–0.3 eV). Thus, the intramolecular relaxation in the excited state after an $S_0 \rightarrow S_1$ transition from an optimized geometry is comparable to the relaxation in the ground state after an $S_1 \rightarrow S_0$ transition (from the relaxed ES geometry). The TD-DFT and CIS values for the Stokes shift of about 0.6 eV for intramolecular relaxation agree well with the first estimate from experimental data. However, for the T_1 state and ROKS they are about 0.2 eV lower which might lead to different intramolecular relaxation behavior.

3.2 Dissociation of the MQ water cluster in the ground and excited states

Our actual goal is the description of solvent dynamics around an excited MQ. In order to achieve a reliable simulation of the excited state molecular solvation dynamics, ground and excited state potential energy surfaces (PES) for the solvent molecules around MQ have to be described correctly. We start with the simplest model, an MQ·1H_2O cluster, for which we calculated the dissociation curve. For this purpose, an MQ·1H_2O complex was optimized (see Fig. 3) and the geometry was verified to be a minimum by the absence of negative PES curvature. The $O_{[MQ]}$–$H_{[H_2O]}$ distance then was varied in steps of 0.05 Å between 1.95 Å and 4.00 Å. Counterpoise corrected PBE0[b] calculations were done to check whether the basis set superposition error (BSSE) would strongly affect the dissociation curve. This was not the case, and we therefore compare non-counterpoise corrected values. At the end points of the plotted dissociation curve, single point energies were calculated with CCSD(T). We added EOM-CCSD excitation energies to the CCSD(T) ground state energy to calculate the total excited state energies. Energies given are relative to the energy for the O–H distance of 1.95 Å.

3.2.1 Performance of TD-DFT and the effect of dispersion correction. The potential energy curves for dissociating a MQ·H_2O cluster using several levels of theory are shown in Fig. 4. Both ground and excited states are considered. In the ground state we find a very good agreement of the benchmark calculations with the PBE0[b] results. Dispersion uncorrected BLYP[a] on the other hand clearly predicts a weaker hydrogen bond. However, this problem can be alleviated by adding the empirical Grimme dispersion corrections. The potential energy surfaces of BLYP-D[a] and PBE0[b] then closely agree. For the excited state, the TD-BLYP[a] results give the correct trend of a weakened intermolecular interaction. The PBE0[b] results agree better with the EOM-CCSD reference calculations. In addition to the DFT dissociation curves depicted in Fig. 4, we calculated dissociation curves using HF[a], CIS[a] and semi-empirical methods (data not shown). The results illustrate again the need for dispersion correction, and confirm the finding of a lower hydrogen bond dissociation energy in the excited state. The lowered dissociation energy corresponds to a decrease in excitation energy with increasing r(O–H) distance.

Table 3 MQ Selected geometric parameters of MQ in its optimized ground and excited states. Bond lengths in Angström and angles in degree

State Level of theory	GS BLYP-D[a]	ES(TD-DFT) BLYP-D[a]	ES(T_1, LSD) BLYP-D[a]	ES (ROKS) BLYP-D[c]	GS PBE0[b]	ES(TD-DFT) PBE0[b]
r(C[6]–O[11])	1.257	1.285	1.269	1.264	1.238	1.252
r(C[6]–C[7])	1.481	1.481	1.452	1.455	1.466	1.451
r(C[9]–C[10])	1.466	1.409	1.451	1.434	1.445	1.398
r(C[3]–C[2])	1.406	1.377	1.377	1.369	1.392	1.360
r(C[2]–N[1])	1.367	1.371	1.408	1.399	1.343	1.369
r(C[9]–N[1])	1.383	1.450	1.409	1.412	1.364	1.414
∠(C[5]–C[6]–C[7])	114.3	116.7	116.6	116.8	114.1	116.4
∠(C[2]–N[1]–C[9])	122.6	119.4	120.8	120.5	122.6	119.5

Table 4 Calculations on the Stokes shift for several levels of theory/excited state methods in eV

Level of theory Method ES	BLYP-D[a] TD-DFT[a]	BLYP-D[a] T_1 (LSD)	BLYP-D[c] ROKS[c]	PBE0[b] TD-DFT	PBE0[b] (PCM) TD-DFT	HF[b] CIS[b]
Vertical excitation from GS geometry	2.00	1.26	1.68	2.11	2.54	3.03
Intramol. relaxation in ES	0.35	0.16	0.19	0.31	0.28	0.29
Vertical excitation from ES geometry	1.27	0.95	1.30	1.48	2.04	2.43
Stokes shift	0.73	0.32	0.38	0.63	0.50	0.60

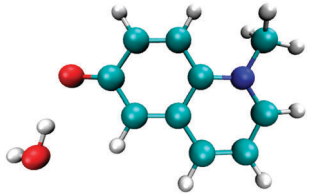

Fig. 3 Relaxed PBE0[b] structure of an MQ·1H_2O complex.

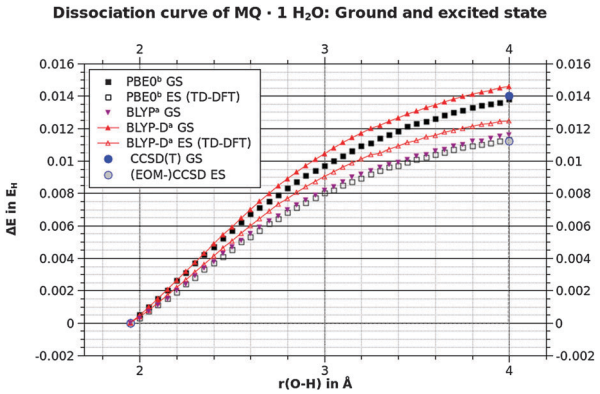

Fig. 4 Comparison of MQ·1H_2O dissociation with benchmark calculations: ground state (GS) and excited state (ES) using TD-DFT.

Weakened hydrogen bonding to the MQ oxygen in full solution is therefore expected to contribute to the total Stokes shift.

In conclusion, the PBE0[b] functional gives an accurate description of both the ground and excited states. While the computationally efficient BLYP-D method gives a good description of the ground state surface, its TD-DFT performance in the excited state is disappointing.

3.2.2 Description of the excitated state dissociation by the triplet state. For further evaluation of the excited state description by a pure density functional, we therefore return to the more heuristic approach of the T_1 state (see Fig. 5). We find that the dissociation curve of MQ·1H_2O in the T_1 state is in very good agreement with the benchmark for the excited state: the deviation from the reference is only 0.5×10^{-3} E_H, and smaller than for the BLYP TD-DFT approach. The ability of a triplet to approximate intermolecular interactions in the excited state was also verified by comparison to the PM6-DH2[84] triplet level of theory as well as with ROKS[c] (as in the case of isolated MQ the ROKS results are very similar to the T_1 state).

The energies were calculated at the BLYP-D[c] level. This allows us to qualitatively examine basis set effects, as the use of a plane wave basis set (c) eliminates the basis set superposition error (BSSE). While the effect of the basis set is visible (see

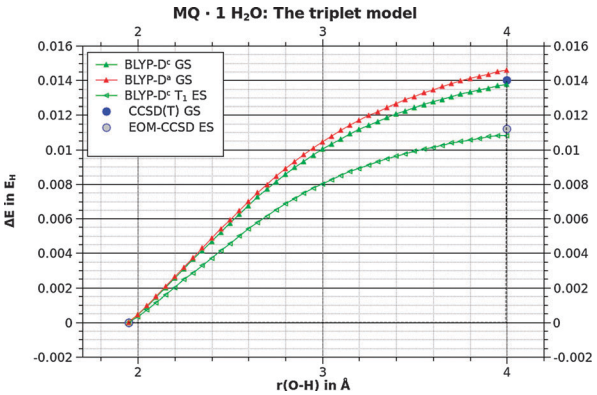

Fig. 5 Comparison of MQ·1H_2O dissociation curves with benchmark calculations; illustrating the performance of the triplet model and basis set effects.

Fig. 5), it does not change the good agreement with our reference calculations. The simulation of the excited state by the triplet state opens up a computationally efficient way of calculating the solvent relaxation—if it is transferable to the full system.

3.3 Ground and excited state dissociation of MQ·4H_2O

To estimate the consequences arising from the use of a triplet instead of the true S_1 state, we devised a more sensitive test. We cut out a structure of MQ bound to four H_2O from the BLYP molecular dynamics run (see Fig. 6). This results in an unrelaxed geometry with a highly screened MQ oxygen and a partial network of hydrogen bonds. The coordinate of the water molecule closest to the MQ oxygen was varied over $O_{[MQ]}$–$H_{[H_2O]}$ distances between 1.45 Å and 3.45 Å. As for MQ·1H_2O, the obtained dissociation curves were compared with coupled cluster calculations. The energies plotted are referenced to r(O–H) = 1.9 Å.

The dissociation energy obtained by DFT methods is lower than the benchmark CCSD(T) value (see Fig. 7). MP2 and

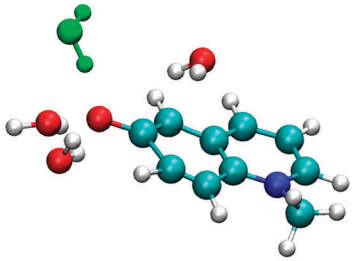

Fig. 6 MQ·4H_2O cluster cut out of BLYP-MD of MQ and the four closest lying H_2O molecules, unrelaxed structure. The distance of the H_2O (green) to the MQ oxygen was varied.

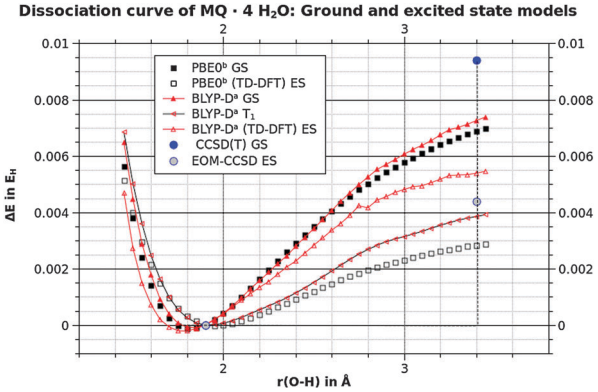

Fig. 7 Comparison of MQ water dissociation curves in the ground state (GS) and the excited state (ES) to benchmark, using the TD-DFT and T_1 models for excitation.

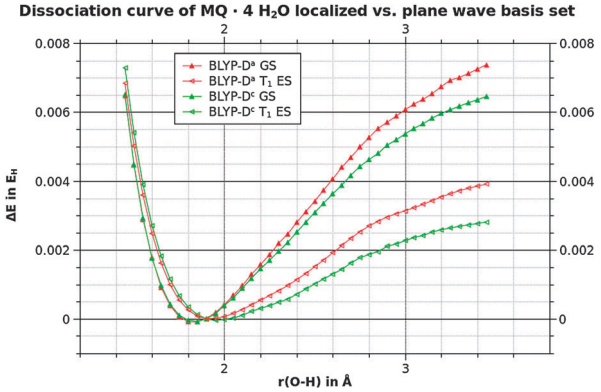

Fig. 8 Comparison of MQ water dissociation curves in the ground state (GS) and the excited state (ES) to benchmark, using localized (red) and plane-wave basis sets (green).

Table 5 MQ·4H_2O dissociation energies in 10^{-3} E_H

Level of theory Method ES	BLYP-D[a] TD-DFT	BLYP-D[a] T_1 (LSD)	PBE0[b] TD-DFT	CCSD EOM
GS	7.3	7.3	6.9	9.4
ES	5.4	3.9	2.8	4.4
Δ(GS-ES)	1.9	3.4	4.0	5.0

CCSD calculations also confirmed this apparent underbonding of the DFT methods in the ground state.

The dissociation energies in Table 5 show that the BLYP-D result is closest to the CCSD(T) energy, and the BLYP-D T_1 model is closest to the EOM-CCSD energy. In order to judge the performance of these methods, one also has to look at the change in dissociation energy between the ground and excited states (ΔGS-ES, Table 5). The decrease in dissociation energy for TD-BLYP-D[a] is less than half of the effect found in the benchmark calculations. In addition to this relatively poor performance of the TD-BLYP-D surface scan, it was necessary to switch between excited states ES5 for r(O–H) < 2.8 and ES4 for r(O–H) 2.8–3.45, as following the oscillator strength the lower excited states were dark. The T_1 model again shows better agreement with benchmark calculations than the TD-DFT approach when using the BLYP functional; however, for Δ(GS-ES) the TD-PBE0[b] value agrees best with the reference calculation.

As in the case of MQ·1H_2O we compare the results obtained using localized basis sets to those obtained with the plane-wave pseudopotential method (see Fig. 8). This is intended to give a qualitative estimate of the errors due to basis set incompleteness. Note that the reference calculations were also done with localized basis sets and are therefore subject to the BSSE.

As the dissociation energy is smaller than in the case of an unscreened MQ (compare Fig. 4), the relative effect of the basis set, *i.e.* the BSSE is larger. However, the change in hydrogen bond dissociation energy when going from the ground to the excited state is almost the same, leading us to the conclusion that the change in intermolecular interactions upon excitation is less affected by basis set effects. From the cluster benchmarks, the T_1 model to the excited state is confirmed to be a reasonably accurate approximation.

3.4 Fully solvated MQ in its excited state

Having examined the dissociation curves of MQ–H_2O complexes, we switch to a fully solvated MQ + 130 H_2O and periodic boundary conditions. Under these conditions, no one-dimensional hydrogen bond dissociation curve can be calculated. Instead, we used MD to generate a series of representative geometries from the phase space. Starting from these, we first examine excitation energies in solution and then compare the change in intermolecular forces upon PES change. From the last 1.2 ps of the dispersion corrected BLYP trajectory frames were selected to calculate the ground state (GS), the T_1 and the TD-DFT S_1 excited state. For these calculations, we used the BLYP[c] level of theory. Only frames in which the oscillator strength for the first excited state exceeded those of the other states (the first three were calculated) and was above 0.01 were used. Force calculations and excitation energies are based on the same ten sampled frames that fulfill these criteria. In addition, we calculated Mulliken charges of these snapshots in the ground and the triplet state, using the GAPW approach with an Ahlrichs-pTZV all electron basis set.[85,86]

3.4.1 Excitation energies of fully solvated MQ. For some of our TD-DFT calculations, the second excited state was found to have the highest oscillator strength. This issue has already been discussed in the context of a dark apparent S_1 state and switching between low lying excited states in the calculation of the dissociation curve of MQ·4H_2O. Averaging ten $S_1 \leftarrow S_0$ excitation energies results in an excitation energy of 2.64 eV, which is still red shifted from the experimental value of 3.04 eV.

From the gas-phase excitation energy of 2.0 eV (Table 4), we calculate a solvatochromic blue shift of 0.64 eV. Adding this blue shift to the gas-phase EOM-CCSD excitation energy yields a value of 3.01 eV, which differs only by 0.03 eV from the experimental excitation energy. This confirms that intermolecular interactions are very well represented by DFT.

3.4.2 Population analysis of fully solvated MQ. Mulliken charge analysis on the heavy atoms indicates a transfer of negative charge of 0.1 e from the oxygen atom and delocalization

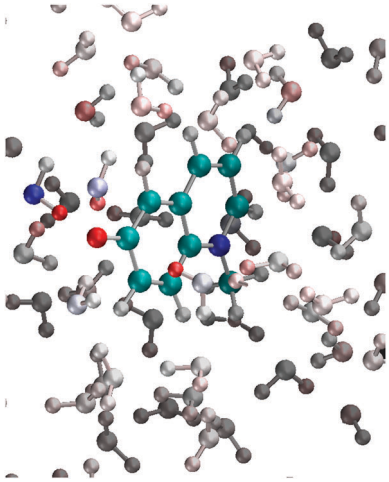

Fig. 9 Change in partial charge in the solvent upon changing from S_0 to T_1, negative charge in red and positive charge in blue.

into the pyridinium ring. This is consistent with the change in partial charges obtained from the gas phase (see Table 2). Solute–solvent charge transfer was small, with the solute gaining 0.03 e in partial charge on average.

We find that the change in partial charges is largest near the MQ-Oxygen (see Fig. 9). The gain in electronic charge of the solute is most likely due to transfer of electron density from the hydrogen bonds around MQ into the solute.

3.4.3 Change in the resulting forces on water molecules upon electronic excitation. The Mulliken charges can give a first idea of charge reorganization. The MQ-oxygen is a hydrogen bonding donor and the pyridinium ring is screened by the methyl group. One expects the change in force upon electronic excitation to be strongest around the MQ-oxygen, where hydrogen bonding will be significantly weakened. However to accurately predict the behavior of the solvation network we explicitly calculated intermolecular forces. The triplet model has already been shown to agree somewhat better with the reference calculations on MQ·xH$_2$O clusters than TD-BLYP[a], while the same trend of weakened hydrogen bonding in the excited state was found with both approaches. TD-BLYP may therefore be used as a qualitative check to see if the excited state models qualitatively agree in a realistic system and to make sure that no important effects were overlooked: the water cluster benchmarks were limited to hydrogen bonds of H$_2$O molecules around the MQ oxygen. Aqueous solvation naturally also affects the positive side of the zwitterionic dipole, the formally cationic nitrogen atom. In order to quantify the representation of all intermolecular forces in the excited solvated MQ, we computed effective intermolecular forces $\vec{f}_{int}$ on the water molecules by the sum of the forces on each atom of a given H$_2$O molecule according to eqn (1).

$$\vec{f}_{\mathrm{int}} = \vec{f}_{\mathrm{O}} + \vec{f}_{\mathrm{H}_1} + \vec{f}_{\mathrm{H}_2} \qquad (1)$$

The forces inside and on the MQ molecule itself were ignored, as the focus of interest is the dipolar relaxation of the solvation shell and later its influence on the Stokes shift. The difference in intermolecular force when switching the PES can also be calculated for any given molecule by computing the difference of the respective vectors $\vec{f}_{\mathrm{int}}$. For comparison between two PES (A and B), the norm of the difference of the effective forces was averaged over all H$_2$O molecules for all ten frames according to

$$\Delta F_{\mathrm{inter}} = \langle \| \vec{f}_{\mathrm{intB}} - \vec{f}_{\mathrm{intA}} \| \rangle \qquad (2)$$

$\Delta F_{\mathrm{inter}}$ is the average change of the intermolecular force on a water molecule in solution when switching from PES A to PES B. It also serves as a measure of how the dynamics will change upon putting the system in an excited state. If $\Delta F_{\mathrm{inter}}$ is calculated only for water molecules close to certain positions local information can also be extracted from the forces. The MQ-oxygen and formally cationic nitrogen atoms were chosen as centers as they are the places where the effect of excitation is expected to be the largest. All water molecules that have any atom closer than 3.6 Å to the chosen center were averaged for the entire system as in eqn (2). In addition, we have also calculated the norm of the single largest $\Delta\vec{f}_{\mathrm{int}AB}$ encountered.

The results are shown in Fig. 10. We compare the average change in the effective force $\Delta F_{\mathrm{inter}}$ (and its maximum single-molecular contribution) for vertical excitations using the PES pairs (GS, T_1) and (GS, S_1/TDDFT), but also between the two excited states (S_1, T_1). Upon excitation (GS, ES), the average of the effective intermolecular forces for the water molecules around the N and O centers of MQ changes by 0.4 or about 1.3 mE$_{\mathrm{H}}$ Å^{-1} respectively (1 mE$_{\mathrm{H}}$ Å^{-1} = 43.6 pN). The maximum change of the force is two to three times larger than the average change over all water molecules in the first solvation shell. The average change of the force is 6–7 times higher near the MQ-oxygen than in the whole solution and the maximum change is found at the oxygen (this is valid for each individual frame as well). There exists one exception for the difference between triplet and singlet excited states, where the maximum change is elevated by one single large deviation in a

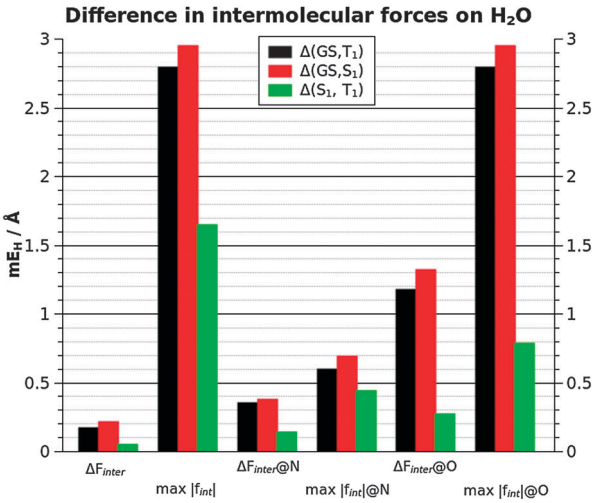

Fig. 10 Comparison of average intermolecular force and maximum $\|\Delta_{AB}\vec{f}_{\mathrm{int}}\|$ around MQ for all H$_2$O, at the nitrogen $\Delta F_{\mathrm{inter}}$@N and oxygen atom $\Delta F_{\mathrm{inter}}$@O of MQ, comparing the ground state (GS) with TD-DFT S_1 and the triplet model of the excited state.

H_2O not close to MQ. In addition to this the change in force near the nitrogen center (Fig. 10, $\Delta F_{\text{inter}}@N$) is also significant but its absolute is on average only 29% of $\Delta F_{\text{inter}}@O$. Comparing maximum forces shows an even larger difference. Also there are on average only 3 molecules within the cutoff radius on the nitrogen atom, while there are 6 near the oxygen atom. Therefore, limiting our post-HF benchmarks to water molecules close to the MQ-oxygen was justified. Furthermore all differences between the excited state models are smaller than the differences between ground and excited states. The effect is especially strong near the crucial oxygen atom, where the difference is 0.27 mE_H $Å^{-1}$ on average or 20% of the effect of TD-DFT excitation. Contrary to the effect measured for the water clusters, the difference between the ground and excited states is actually larger for the TD-DFT forces.

3.5 Relative computational cost

The relative cost of a spin unrestricted DFT calculation is twice the cost of a restricted singlet calculation per SCF step. In contrast to this, TD-DFT in the current implementations requires the diagonalization of a large matrix in addition to a restricted singlet ground state calculation. In the case of full solvation this added an order of magnitude to the computational cost. Furthermore, it is not currently possible to use CPMD-like propagation schemes for the TD-DFT excited state, which adds another order of magnitude to the relative cost in an MD run.

4 Conclusion

As an initial step, we have calculated gas phase excitation energies, geometries and dipole moments of *N*-methyl-6-quinolone comparing different levels of theory. Apart from a slight overestimation of the excited state dipole moment by DFT methods we find reasonable agreement with benchmark post-HF calculations and a surprisingly good agreement of different DFT based approaches to the excited state. All methods predict a significant decrease in the dipole moment upon excitation. We also calculated intramolecular reorganization energies, finding good agreement between TD-DFT methods and CIS.

Our actual aim was to investigate the structural and dynamic response of the hydrogen bond network of MQ in aqueous solution. Specifically we are interested in the accuracy to which the change of the hydrogen bond network due to electronic excitation can be reproduced with DFT. Using high quality reference methods, we find that upon excitation MQ hydrogen bonding is considerably weakened. The BLYP T_1 state and hybrid TD-DFT (PBE0) reasonably reproduce this effect.

The central result of this study is the applicability of the triplet description for the simulation of the excited-state dynamics of a fully solvated MQ. Such a description is necessary for the adequate representation of the experimentally accessible time-dependent Stokes shift. In particular, we found that the triplet state also qualitatively agrees with TD-DFT forces in the full system. Excitation predominantly affects the solvation around the electronegative oxygen of MQ. Through the agreement between S_1 and T_1 states (calculated with LSD) the computational cost of simulating solvent relaxation is greatly reduced. This enables the direct simulation of femtosecond spectroscopic experiments in large disordered systems that require considerable phase space sampling for convergence, such as terahertz spectra.

Acknowledgements

This work has been supported by the German Research Foundation (DFG) under grants SE 1008/5 and SE 1008/6. Computing infrastructure was provided by the Northern German Supercomputing Alliance (HLRN) under grant HLRN/bec00061.

References

1 G. E. Walrafen, *Water. A Comprehensive Treatise*, ed. F. Franks, Plenum Press, New York, 1972, Vol. 1.
2 F. H. Stillinger, *Science*, 1980, **209**, 451.
3 D. Eisenberg and W. Kauzmann, *The Structure and Properties of Water*, Clarendon, Oxford, 1969.
4 H. J. Bakker and J. L. Skinner, *Chem. Rev.*, 2010, **110**, 1498–1517.
5 H. J. Bakker and H.-K. Nienhuys, *Science*, 2002, **297**(5581), 587–590.
6 R. N. Butler and A. G. Coyne, *Chem. Rev.*, 2010, **110**(10), 6302–6337.
7 R. Bukowski, K. Szalewicz, G. C. Groenenboom and A. van der Avoird, *Science*, 2007, **315**, 1249–1252.
8 G. Hura, J. M. Sorenson, R. M. Glaeser and T. Head-Gordon, *J. Chem. Phys.*, 2000, **113**, 9140–9148.
9 T. D. Kühne, M. Krack and M. Parrinello, *J. Chem. Theor. Comput.*, 2009, **5**, 235–241.
10 A. Katrusiak, *Phys. Rev. Lett.*, 1996, **77**, 4366.
11 K. Laasonen, M. Sprik, M. Parrinello and R. Car, *J. Chem. Phys.*, 1993, **99**, 9080–9089.
12 M. Vogel, *Eur. Phys. J. Spec. Top.*, 2010, **189**, 47–64.
13 M. Fayer and N. E. Levinger, *Annu. Rev. Anal. Chem.*, 2010, **3**, 89–107.
14 J. C. Rasaiah, S. Garde and G. Hummer, *Annu. Rev. Phys. Chem.*, 2008, **59**, 713–740.
15 P. Ball, *ChemPhysChem*, 2008, **9**, 2677–2685.
16 S. K. Pal and A. H. Zewail, *Chem. Rev.*, 2004, **104**, 2099–2124.
17 U. F. Rohrig and D. Sebastiani, *J. Phys. Chem. B*, 2008, **112**, 1267–1274.
18 S. Komin, C. Gossens, I. Tavernelli, U. Röthlisberger and D. Sebastiani, *J. Phys. Chem. B*, 2007, **111**, 5225–5232.
19 Y. Levy and J. N. Onuchic, *Annu. Rev. Biophys. Biomol. Struct.*, 2006, **35**, 389–415.
20 Y. H. P. Auffinger, *Curr. Opin. Struct. Biol.*, 2007, **17**, 325–333.
21 D. Sebastiani and M. Parrinello, *ChemPhysChem*, 2002, **3**, 675.
22 J. Heller, H. Elgabarty, B. Zhuang, D. Sebastiani and D. Hinderberger, *J. Phys. Chem. B*, 2010, **114**, 7429–7438.
23 T. Murakhtina, L. Delle Site and D. Sebastiani, *ChemPhysChem*, 2006, **7**, 1215–1219.
24 R. Iftimie and M. E. Tuckerman, *J. Chem. Phys.*, 2005, **122**, 214508.
25 M. P. Ljungberg, A. P. Lyubartsev, A. Nilsson and L. G. M. Pettersson, *J. Chem. Phys.*, 2009, **131**, 034501.
26 T. Murakhtina, J. Heuft, J.-E. Meijer and D. Sebastiani, *ChemPhysChem*, 2006, **7**, 2578–2584.
27 G. A. Ludueña, T. D. Kühne and D. Sebastiani, *Chem. Mater.*, 2011, **23**, 1424–1429.
28 A. Hoffmann, D. Sebastiani, E. Sugiono, K. S. Kim, H. W. Spiess and I. Schnell, *Chem. Phys. Lett.*, 2004, **388**, 164–169.
29 P. Wernet, D. Nordlund, U. Bergmann, M. Cavalleri, M. Odelius, H. Ogasawara, L. Naslund, T. Hirsch, L. Ojamae, P. Glatzel, L. G. M. Pettersson and A. Nilsson, *Science*, 2004, **304**, 995–999.
30 J. D. Smith, C. D. Cappa, K. R. Wilson, B. M. Messer, R. C. Cohen and R. J. Saykally, *Science*, 2004, **306**, 851–853.
31 A. Nilsson, P. Wernet, D. Nordlund, U. Bergmann, M. Cavalleri, M. Odelius, M. Cavalleri, M. Odelius, H. Ogasawara, L.-Å. Naslund, T. K. Hirsch, L. Ojamae, P. Glatzel and L. G. M. Pettersson, *Science*, 2005, **308**, 793a.
32 J. D. Smith, C. D. Cappa, K. R. Wilson, B. M. Messer, R. C. Cohen and R. J. Saykally, *Science*, 2005, **308**, 793b.

33 T. Pennanen, J. Vaara, P. Lantto, A. Sillanpaa, K. Laasonen and J. Jokisaari, *JACS*, 2004, **126**, 11093–11102.
34 U. Heugen, G. Schwaab, E. Bründermann, M. Heyden, X. Yu, D. M. Leitner and M. Havenith, *Proc. Natl. Acad. Sci. U. S. A.*, 2006, **103**, 12301–12306.
35 M. Heyden, J. Sun, S. Funkner, G. Mathias, H. Forbert, M. Havenith and D. Marx, *Proc. Natl. Acad. Sci. U. S. A.*, 2010, **107**, 12068–12073.
36 M. L. Horng, J. A. Gardecki, A. Papazyan and M. Maroncelli, *J. Phys. Chem.*, 1995, **99**, 17311.
37 G. Haran, W.-D. Sun, K. Wynne and R. M. Hochstrasser, *Chem. Phys. Lett.*, 1997, **274**, 365.
38 A. Dallmann, M. Pfaffe, C. Mügge, R. Mahrwald, S. A. Kovalenko and N. P. Ernsting, *J. Phys. Chem. B*, 2009, **113**, 15619–15628.
39 J. L. Pérez-Lustres, M. Mosquera, T. Senyushkina, S. A. Kovalenko, W. Flasche and N. P. Ernsting, *Angew. Chem., Int. Ed.*, 2005, **44**, 5635–5639.
40 J. L. Pérez-Lustres, F. Rodriguez-Prieto, M. Mosquera, T. A. Senyushkina, N. P. Ernsting and S. A. Kovalenko, *J. Am. Chem. Soc.*, 2007, **129**, 5408–5418.
41 M. Sajadi, Y. Ajaj, I. Ioffe, H. Weingärtner and N. P. Ernsting, *Angew. Chem., Int. Ed.*, 2010, **49**(2), 454–457.
42 J. Schmidt, J. VandeVondele, I.-F. Kuo, D. Sebastiani, J. Siepmann, J. Hutter and C. J. Mundy:, *J. Phys. Chem. B*, 2009, **113**, 11959–11964.
43 M. Boero, T. Ikeshoji and K. Terakura, *ChemPhysChem*, 2005, **6**, 1775–1779.
44 B. Chen, I. Ivanov, M. L. Klein and M. Parrinello, *Phys. Rev. Lett.*, 2003, **91**, 215503.
45 H. Chen, G. A. Voth and N. Agmon, *J. Phys. Chem. B*, 2010, **114**, 333–339.
46 D. Banyai, T. Murakhtina and D. Sebastiani, *Magn. Reson. Chem.*, 2010, **48**, S56–S60.
47 P. L. Geissler, C. Dellago, D. Chandler, J. Hutter and M. Parrinello, *Science*, 2001, **291**, 2121–2124.
48 E. Runge and E. K. U. Gross, *Phys. Rev. Lett.*, 1984, **52**, 997.
49 I. Frank, J. Hutter, D. Marx and M. Parrinello, *J. Chem. Phys.*, 1998, **108**, 4060–4069.
50 J. Gräfenstein, E. Kraka and D. Cremer, *Chem. Phys. Lett.*, 1998, **288**, 593–602.
51 G. Granucci, M. Persico and A. Toniolo, *J. Chem. Phys.*, 2001, **114**, 10608.
52 A. Dreuw and M. Head-Gordon, *Chem. Rev.*, 2005, **105**, 4009–4037.
53 L. Bernasconi, M. Sprik and J. Hutter, *J. Chem. Phys.*, 2003, **119**, 12417–12431.
54 J. Hutter, *J. Chem. Phys.*, 2003, **118**, 3928–3934.
55 M. Odelius, D. Laikov and J. Hutter, *J. Mol. Struct. (THEOCHEM)*, 2003, **630**, 163–175.
56 A. Dreuw and M. Head-Gordon, *J. Am. Chem. Soc.*, 2004, **126**, 4007–4016.
57 L. Bernasconi, J. Blumberger, M. Sprik and R. Vuilleumier, *J. Chem. Phys.*, 2004, **121**, 11885–11899.
58 L. Bernasconi, M. Sprik and J. Hutter, *Chem. Phys. Lett.*, 2004, **394**, 141–146.
59 G. Worth, M. Robb and B. Lasorne, *Mol. Phys.*, 2008, **106**, 2077–2091.
60 M. Nest, T. Klamroth and P. Saalfrank, *J. Chem. Phys.*, 2005, **122**, 124104.
61 A. D. Becke, *Phys. Rev. A*, 1988, **38**, 3098.
62 C. Lee, W. Yang and R. G. Parr, *Phys. Rev. B: Condens. Matter*, 1988, **37**, 785–789.
63 S. Grimme, *J. Comput. Chem.*, 2006, **27**(15), 1787–1799.
64 J. Perdew, K. Burke and M. Ernzerhof, *J. Phys. Chem.*, 1996, **105**, 9982–9985.
65 P. Barczyński, M. Ratajczak-Sitarz, A. Katrusiak and M. Szafran, *J. Mol. Struct.*, 2010, **976**, 87–96.
66 D. Jacquemin, V. Wathelet, E. A. Perpète and C. Adamo, *J. Chem. Theor. Comput.*, 2009, **5**, 2420–2435.
67 J. F. Stanton and R. J. Bartlett, *J. Chem. Phys.*, 1993, **98**, 7029–7039.
68 R. Krishnan, J. Binkley, R. Seeger and J. Pople, *J. Chem. Phys.*, 1980, **72**, 650.
69 S. Goedecker and C. J. Umrigar, *Phys. Rev. A*, 1997, **55**, 1765–1771.
70 S. Grimm, C. Nonnenberg and I. Frank, *J. Chem. Phys.*, 2003, **119**, 11574.
71 N. Troullier and J. L. Martins, *Phys. Rev. B: Condens. Matter*, 1991, **43**, 1993–2006.
72 M. J. Frisch, G. W. Trucks, H. B. Schlegel, G. E. Scuseria, M. A. Robb, J. R. Cheeseman, G. Scalmani, V. Barone, B. Mennucci, G. A. Petersson, H. Nakatsuji, M. Caricato, X. Li, H. P. Hratchian, A. F. Izmaylov, J. Bloino, G. Zheng, J. L. Sonnenberg, M. Hada, M. Ehara, K. Toyota, R. Fukuda, J. Hasegawa, M. Ishida, T. Nakajima, Y. Honda, O. Kitao, H. Nakai, T. Vreven, J. A. Montgomery, Jr., J. E. Peralta, F. Ogliaro, M. Bearpark, J. J. Heyd, E. Brothers, K. N. Kudin, V. N. Staroverov, R. Kobayashi, J. Normand, K. Raghavachari, A. Rendell, J. C. Burant, S. S. Iyengar, J. Tomasi, M. Cossi, N. Rega, J. M. Millam, M. Klene, J. E. Knox, J. B. Cross, V. Bakken, C. Adamo, J. Jaramillo, R. Gomperts, R. E. Stratmann, O. Yazyev, A. J. Austin, R. Cammi, C. Pomelli, J. W. Ochterski, R. L. Martin, K. Morokuma, V. G. Zakrzewski, G. A. Voth, P. Salvador, J. J. Dannenberg, S. Dapprich, A. D. Daniels, O. Farkas, J. B. Foresman, J. V. Ortiz, J. Cioslowski and D. J. Fox, Gaussian 09 Revision A.02.
73 M. J. Frisch et al., Gaussian 03, Revision E.01.
74 M. Valiev, E. Bylaska, N. Govind, K. Kowalski, T. Straatsma, H. van Dam, D. Wang, J. Nieplocha, E. Apra, T. Windus and W. de Jong, *Comput. Phys. Commun.*, 2010, **181**, 1477.
75 J. Hutter, D. Marx, P. Focher, M. Tuckerman, W. Andreoni, A. Curioni, E. Fois, U. Rothlisberger, P. Giannozzi, T. Deutsch, A. Alavi, D. Sebastiani, A. Laio, J. VandeVondele, A. Seitsonen, S. Billeter and M. Parrinello, *Computer code CPMD, version 3.13*, 2011.
76 CP2K 2.1.375. C. J. Mundy, F. Mohamed, F. Schiffman, G. Tabacchi, H. Forbert, W. Kuo, J. Hutter, M. Krack, M. Iannuzzi, M. McGrath, M. Guidon, T. D. Kuehne, T. Laino, J. VandeVondele and V. Weber 2010.
77 Mopac2009. J. J. P. Stewart, *Stewart Computational Chemistry*, Colorado Springs, CO, 2008.
78 H. J. Werner, P. J. Knowles, R. Lindh, F. R. Manby, M. Schütz, P. Celani, T. Korona, G. Rauhut, R. D. Amos, A. Bernhardsson, A. Berning, D. L. Cooper, M. J. O. Deegan, A. J. Dobbyn, F. Eckert, C. Hampel Lloyd, S. J. McNicholas, W. Meyer, M. E. Mura, A. Nicklass, P. Palmieri, R. Pitzer, U. Schumann, H. Stoll, A. J. Stone, R. Tarroni and T. Thorsteinsson, *Molpro 2006.1, a package of ab initio programs.*, 2006.
79 F. Neese, *ORCA—an ab initio, Density Functional and Semiempirical program package version 2.7.0.*, University of Bonn, 2009.
80 E. Bardez, A. Chatelain, B. Larrey and B. Valeur, *J. Chem. Phys.*, 1994, **98**, 2357–2366.
81 M. Schreiber, M. Silva-Junior, S. Sauer and W. Thiel, *J. Chem. Phys.*, 2008, **138**, 134110.
82 J. M. Rintelman, I. Adamovic, S. Varganov and M. S. Gordon, *J. Chem. Phys.*, 2005, **122**, 044105.
83 A. E. Reed and F. Weinhold, *J. Phys. Chem.*, 1983, **78**, 4066–4073.
84 J. Rezác, J. Fanfrlik, D. Salahub and P. Hobza, *J. Chem. Theor. Comput.*, 2009, **5**, 1749–1760.
85 A. Schäfer, C. Huber and R. Ahlrichs, *J. Chem. Phys.*, 1994, **100**, 5829–5835.
86 G. Lippert, J. Hutter and M. Parrinello, *Theor. Chem. Acc.*, 1999, **103**, 124–140.

5.2 Paper II

Reproduced from (2)
Zeitschrift für Physikalische Chemie International journal of research in physical chemistry and chemical physics. Volume 226, Issue 11-12, Pages 14151424, ISSN (Print) 0942-9352, DOI: 10.1524/zpch.2012.0290, October 2012
with permission from Walter de Gruyter GmbH, Berlin.

Z. Phys. Chem. **226** (2012) 1415–1424 / **DOI** 10.1524/zpch.2012.0290

First Principles Calculations of NMR Chemical Shifts of Liquid Water at an Amorphous Silica Interface

By Xiang Yang Guo[1], Tobias Watermann[1], Shane Keane[1], Christoph Allolio[1], and Daniel Sebastiani[1,2,*]

[1] Physics Department, Freie Universität Berlin, Arnimalle 14, 14195 Germany
[2] Institute of Chemistry, Martin-Luther-Universität Halle Wittenberg, Kurt-Mothes-Strasse 2, 06120 Halle, Germany

Dedicated to Professor Hans Wolfgang Spiess on the occasion of his 70th birthday

(Received June 4, 2012; accepted in revised form September 21, 2012)
(Published online October 29, 2012)

Car-Parrinello Molecular Dynamics Simulations / DFT / NMR Chemical Shift Calculations / MCM-41 / Liquid Water Structure / Confinement

We investigate the anomalous structure and hydrogen bond network of water molecules confined inside a silica nanopore (MCM-41 type). In addition to geometric data, we use proton NMR chemical shifts as a measure for the strength of the H-bonding network. We compute the ^{1}H NMR shifts of confined water based on a first principle approach in the framework of density functional perturbation theory under periodic boundary conditions. The hydrophilic character of the silica is well manifested in the water density profile. Our calculations illustrate both the modifications of the ^{1}H NMR chemical shifts of the water with respect to bulk water and a considerable slowing down of water diffusion. In the vicinity of silanols, weakly hydrogen bonded liquid water is observed, while at the center region of the pore, the hydrogen bonding network is enhanced with respect to bulk water.

1. Introduction

Periodically structured porous materials have evoked wide interest for various applications in recent years. Their micro-structure is observed to be composed of orderly arranged pores with uniform size [1]. MCM-41, as one of the most studied type, is characterized by pores less than 40 Å in diameter, within which liquids can be confined. Experimental studies regarding MCM-41 and the properties of liquids confined within it have been performed at length. Techniques such as quasi-elastic and deep elastic neutron scattering [2–4], neutron diffraction with isotopic substitution [5], x-ray spectroscopy [6], sum frequency vibration spectroscopy [7], adsorption calorimetry [8],

* Corresponding author. E-mail: daniel.sebastiani@fu-berlin.de

and NMR spectroscopy [9–11] have provided a lot of experimental data which may be compared to simulation data.

The silanol groups on the silica surface play a special role for its ability of supplying hydrogen bonding sites for the confined solvent [14]. With respect to their density on the MCM-41 silica surface [9,10,13], the consensus seems to be about 2 to 3 nm^{-2}, meaning these groups cannot form hydrogen bonds with each other as they are too far apart. Since the average distance between them is about 5.8 Å, one water molecule cannot be simultaneously hydrogen bonded to two silanol groups [1]. Up to three water molecules, however, may be hydrogen bonded to a single silanol group [14]. The nature of water differed from bulk water when it is hydrogen bonded to the hydroxyl groups on the silica surface. Recent neutron scattering evidence suggests that the hydrogen bond formed between a water molecule and a silanol in mesoporous silica is stronger than the hydrogen bonds between water molecules [4].

Many simulations have been conducted focusing on the water silica interface. Since the structure of MCM-41 is not fully known, many varying models have been proposed to simulate its surface. For example, Shirono *et al.* [15] and Kleestorfer *et al.* [16] used a block of alpha-quartz out of which they cut circular pores of various sizes. In cases where there remained oxygens attached to only one silicon atom, hydrogen atoms were added to create the silanol groups characteristic of the surface of MCM-41. Gallo *et al.* [12] used beta-cristobalite which was melted and equilibrated at 1000 K. It was then quenched and a cylindrical pore 15 Å in diameter was carved into it. Again, oxygens left attached to only one silicon atom were capped with hydrogen atoms. Sherendovich *et al.* [9] use different experimentally derived criteria to recommend a model of MCM-41 based on the structure of tridymite. The model they proposed was not in fact tridymite, but a fictitious structure created from pieces of it stuck together in different configurations. With respect to the silica-water interface, Sulpizi *et al.* [29] conducted *ab initio* Molecular Dynamics (AIMD) on the hydroxilated (0001) α-quartz surface system. Two types of silanol groups were addressed in their results, so called out-of-plane silanols with a strong acidic character and in-plane silanols with weaker acidity.

In this work, a simplified surface model is constructed which has the virtue of containing the same density of silanol groups as MCM-41. We obtain the density and translational mobility profiles of water confined in this model by applying first principle density functional theory based molecular dynamics (AIMD) simulation. Then we compute ensemble averages of Nuclear Magnetic Resonance (NMR) calculations on the confined water molecules and compare the results with bulk water. Furthermore we analyze the distribution of the water NMR shifts along the pore axis and the impact of the geometric confinement on the bound water NMR shifts so as to increase our understanding of the influence of spatial confinement on the structure and dynamics of water.

2. Computional details

The water-silica interface is represented by a simplified yet realistic surface model which demonstrates the experimentally known structure of the MCM-41 pore. Figure 1

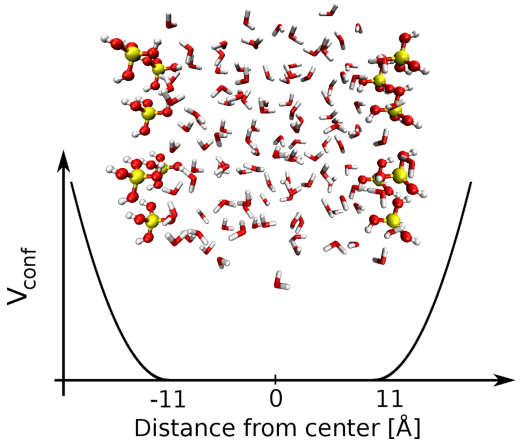

Fig. 1. Two silica-water unit cells from a snapshot of the MD simulation (*xz* side view). The three-dimensional periodic cell contains six silicic acid groups at the walls and 59 water molecules in between. Si, O and H atoms are represented in yellow, red and white respectively. The silica surface is represented by three isolated $Si(OH)_4$ tetrahedrons.

shows a snapshot of the model. Silicic acid $Si(OH)_4$ is used to model the silanol groups with the three outer hydroxy groups fixed.

Following the experimental results from the NMR spectroscopy [9,10] on the structure of MCM-41, the density of the silanol groups is taken to be $3\,nm^{-2}$. The possible hydrogen bonding between Si-O-Si bridge and water is missing in this model. We assume it is only of minor influence since the highly concentrated silanol groups on the surface hamper sterically the formation of this type of hydrogen bonds. In the next more sophisticated model, the actual amorphous pore will be considered.

The diffusion of water into the surface is prevented by a harmonic potential (Fig. 1). The potential only acts on the water molecules to allow free Si−OH vibrations. The simulation is carried out in a fully periodic box with a size of $28 \times 10 \times 10$ Å, two flat silanol walls are placed 22 Å apart, 6 Å space is left at either end of the potential to reduce periodic effects in the *x* direction. 59 water molecules are placed between the two walls. In order to employ a timestep of 1 fs, we choose heavy water instead of H_2O to double the calculation speed.

We run DFT based molecular dynamics simulations in the CP2K package [30]. The BLYP [31] exchange-correlation functional was used, as well as the TZVP basis sets and GTH pseudopotentials [32]. The DFT-D2 Grimme [33] dispersion correction was also used. In total, the simulation ran for over 45 ps.

The system was first equilibrated for 10 ps using the canonical ensemble, employing a Nosé–Hoover thermostat. The temperature was set to be 320 K. The simulation was then switched to the microcanonical ensemble for the remaining time.

The NMR chemical shifts are computed as ensemble averages from ab initio nuclear shielding calculations within the CP2K package [30]. A random set of 15 snapshots from the NVE trajectory was sampled, and chemical shifts of all atoms were calculated. For the referencing of the nuclear shielding tensors to chemical shifts, we utilized the method applied in Ref. [23] The NMR simulation used a Gaussian aug-

mented plane wave approach with GAPW plane wave cutoff 320 Ry, the BLYP-DFT exchange-correlation functional and the TZV2PX-MOLOPT-GTH basis set were employed [34].

It should be noted that we do not compute the quantum propagation of the nuclear spin state which occurs on a timescale of millisecond in a typical NMR experiment, but instead we compute directly the energy difference of the 2 states. Hence the simulation duration on a picosecond level is adequate to achieve the necessary sampling for the averaged instantaneous chemical shifts [35–40].

3. Results and discussion

3.1 Translational dynamical properties

One of the most salient properties of water confined in MCM-41, discovered by experiments and MD simulations [12,15,17,18] is a slower translational dynamics with respect to bulk water. The translational dynamics of our system were measured by calculating the diffusion coefficient of the system. The ratio of the diffusion coefficient of water confined in MCM-41 to that of bulk water

$$q = \frac{D_{D_2O}^{Confined}}{D_{D_2O}^{Bulk}}$$

has been ascertained experimentally and *via* simulation. Values of q range quite widely from 0.23 to 0.64 [15,17,18,24], with the consensus showing a much slower diffusion of water within MCM-41 pores. In this work, the reference self diffusion coefficient value for bulk heavy water is taken to be 0.187 Å^2/ps from Ref. [28]. In order to obtain the value of q for our system, we calculated the diffusion coefficient D for our confined water according to Einstein's relation

$$D = \frac{\mathrm{MSD}}{2dt} = \left\langle \frac{(R_{D_2O}(t) - R_{D_2O}(0))^2}{2dt} \right\rangle_{D_2O}$$

with the numerator representing the mean-square displacement (MSD), t the time, and d the number of dimensions in which the quantity is measured. For the simulation of confined water, only diffusion in the two periodic directions (in our case the y and z dimensions) is taken into account in order to reduce possible distortion due to the presence of the walls [18].

The mean-square displacement (MSD) of water molecules over time in the confined cases is presented in Fig. 2. From this graph, the diffusion coefficient for confined water is calculated to be 0.05 Å^2/ps. As 0.187 Å^2/ps for bulk water, the resulting ratio q is about 0.27 which falls into the range we obtained from literature.

As pointed out in several studies [11,12], however, taking the diffusion coefficient of the whole system all at once fails to take adequate consideration of different effects of the confinement at different position within the pore.

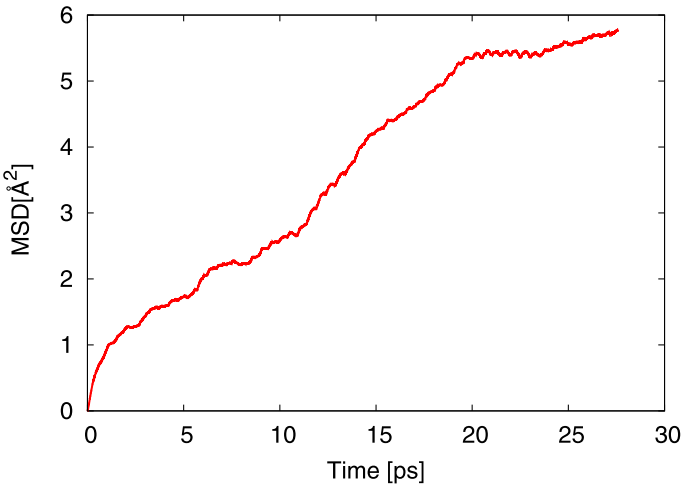

Fig. 2. Global MSD of the oxygen atoms of confined water at $T = 320$ K.

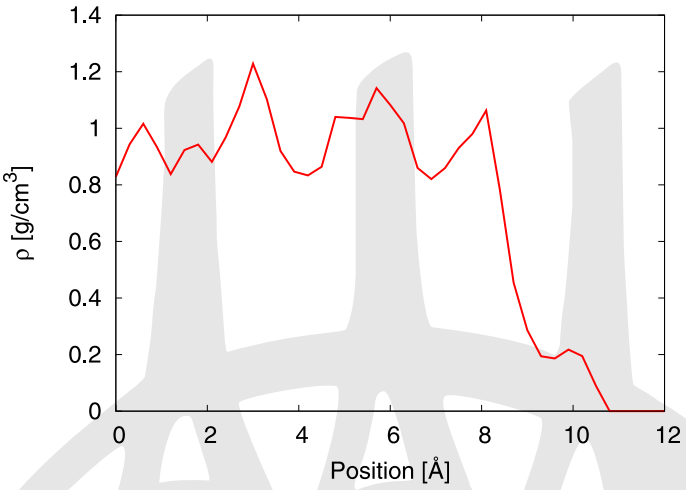

Fig. 3. Density Profile of Water confined between two silica slabs. The origin $x = 0$ Å corresponds to the center of the pore.

3.2 Density profile

The water density profile can demonstrate the configuration of confined water and the hydrophilic character of the silica surfaces. In the earlier empirical structure refinement simulations by R. Mancinelli *et al.* [5,27], the density of confined water in a MCM-41 pore is found to be higher in the vicinity of the silanol walls; at 300 K in the interfacial region the density was observed to be about 3 times as large as the density in the middle. This phenomenon stems from a so-called cohesive failure between water molecules. *I. e.* when water is confined between hydrophilic surfaces, voids occur in the middle of the water layer which leads to cohesive failure [26]. As to the present experimental results, Kocherbitov *et al.* [8] measured the apparent density of water in the MCM-41 pores at 298 K to be 0.88 g/cm^3 using H_2O and N_2 sorption method.

In our simulation, the density profile of water was constructed by creating a histogram of the spatial locations of all atoms across the pore with bins 0.3 Å wide and averaging over the entire NVE trajectory, as shown in Fig. 3. The position represents

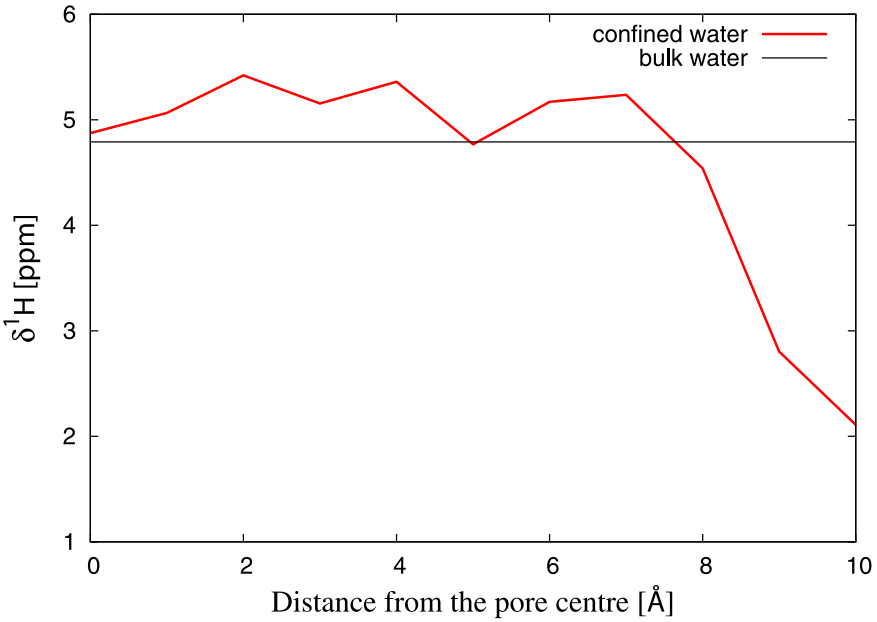

Fig. 4. Calculated ^{1}H NMR chemical shifts of water confined between silica slabs compared with bulk water, the distribution has been symmetrized with respect to the center ($x = 0$ Å), the value of ^{1}H NMR shifts are averaged in the x direction over the length of the model and the NVE trajectory of the system. The graph is drawn up to where the atoms in $Si(OH)_4$ start to appear.

the distance of the oxygen atoms from the center along the pore axis perpendicular to the silica surface. At the core region of the cell (0 Å to 2 Å) a lower density appears in our result, and at the outer edge (7 Å to 9 Å) as well, then it gradually decays to zero at the silica wall. Notable density oscillations are observed from Fig. 3, which reveals that the spatial layering occurred in confined water due to the hydrophilic character of the substrate [21]. For example, we see 2 density peaks near the silica substrate, which indicates that there are 2 separate layers of water in this region. However in several other simulations, the produced density profile showed either one [5,18] or two [12,24,25] peaks in the interfacial region and lower density in the core region. The small bump in the density profile near the very edge of the pore is also present in other results [12,18]. One possible reason for the minimum appearing here is the presence of the silanol groups oxygen atoms in that area taking up space.

3.3 ^{1}H NMR chemical shift calculations

Lately the *ab initio* calculation of nuclear chemical shifts has become one of the most powerful methods for structure determination on the molecular level. Not merely can the calculation interpret the spectra returned by the experiments [23], but also it can produce instantaneous results that are beyond experimental capability. Particularly the instantaneous ^{1}H NMR shifts can provide significant probe for the hydrogen bonding network of specific chemical environments [41,42].

The NMR shifts profile we obtained, as shown in Fig. 4, substantially indicates the configuration of water confined between the 2 silica slabs. The experimental ^{1}H NMR chemical shift $\delta = 4.79$ ppm for bulk water is taken from the value given in Ref. [22]. Figure 4 displays that in the major part of the cell, within 7.6 Å away from the center,

stronger H-bonded water appears with δ varying from 4.7 ppm to 5.4 ppm. The largest $\delta = 5.4$ ppm is reached at $x = 2$ Å. At the core of the pore ($x = 0$ Å), $\delta = 4.86$ ppm. Due to the confining effects of silica slabs, the NMR shifts are greater than those of bulk water. But at the core of the pore, the calculated shift approximates that of the bulk water, reflecting the hydrogen bonding in this region resembles bulk water H-bond network. While the shifts drop to upper-field as approaching the wall, in the vicinity of silanol walls (from $x = 7.6$ Å to $x = 10$ Å), water molecules are found to form weaker hydrogen bonds with each other or with silanols, the minimum value 2.1 ppm is found at $x = 10$ Å. As discussed before, the density profile shows layering effect took place in our cell. According to Gallo *et al.* [21], the interactions of the substrate atoms and thin water layers causes a strong distortion of the H-bond network. This explains why we see a decline of the shifts near the wall, even though it has been experimentally proven that the single silanol-water H-bond is stronger than the water-water H-bond [4].

We analogize the water filling process inside the pore by calculating the running average of ^{1}H chemical shifts up to a certain distance from the wall using equation

$$\delta_{\mathrm{Avg}}{}^1\mathrm{H}(x) = \frac{1}{N_{\mathrm{H}}} \sum_{x'=x_{\mathrm{wall}}}^{x} \delta^1\mathrm{H}(x)$$

$\delta_{\mathrm{Avg}}{}^1\mathrm{H}(x)$ represents the average δ value of a fictitious water film with thickness x. For each value of $\delta_{\mathrm{Avg}}{}^1\mathrm{H}(x)$, we sampled from the wall to the plane at corresponding distance and calculated all the shifts of water between the 2 planes. Taking the limitation of sampling into account, we leave out the first averaged value from $x = 0$ Å to 0.5 Å. The range of averaged NMR shifts along the x direction over the length of the cell covers from 2 to 4.9 ppm which is in good agreement with the experimental value from 1.74 to 4.7 ppm achieved in Buntkowsky's group [1]. Grünberg *et al.* obtained the chemical shift spectra of confined water at varying hydration level using ^{1}H solid-state NMR. In their results for the fully hydrated pore, one single signal appears at 4.7 ppm, and with very small water content ($\leq 2.7\%$), one dominating peak locates at 1.74 ppm which is ascribed to the shift of silanol groups.

Figure 5 shows that the behavior of water in our model resembles the water filling process described in Ref. [1]. Comparing our data with the experimental findings, we observe the same varying tendency in the chemical shifts. The minimum value of δ in Fig. 5 was obtained by computing the shifts of water locating within 0.5 Å to the silica substrate, so as to correspond the very low water filling factor in the experiments. In the interfacial region,the experimental NMR shift is an approximation to the shift of silanol groups. Therefore, it is believed that all water molecules at this region were hydrogen bonded to the silanols. With increased water content, additional water molecules start to form hydrogen bonds with each other which gives rise to ascending chemical shifts. This phenomenon is also reflected in Fig. 5, but increasing distance from the wall plays the role instead of increasing water filling factor. When the water content goes up to 3.2%, a notable peak at 2.5 ppm arises beside a weakened line at 1.74 ppm, which indicates the coexistence of 2 different types of hydrogen bonds. The NMR peak shifts consistently towards down-field upon further increasing hydration level. When there is 23% of water, the line at 2.5 ppm is broadened and shifts to 3.4 ppm. When the pore is completely filled, a single shift appears at 4.7 ppm.

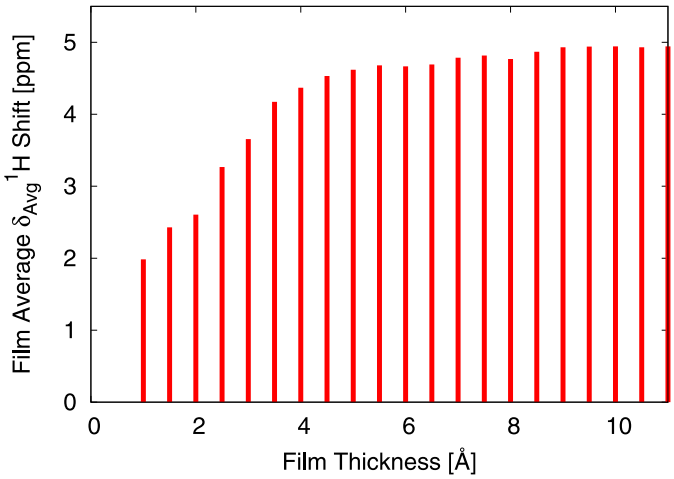

Fig. 5. Average of the ^{1}H NMR chemical shift values of those water molecules residing within a film of given thickness from the wall. The film thickness axis 0 Å and 11 Å are corresponding to the wall and the cell center respectively.

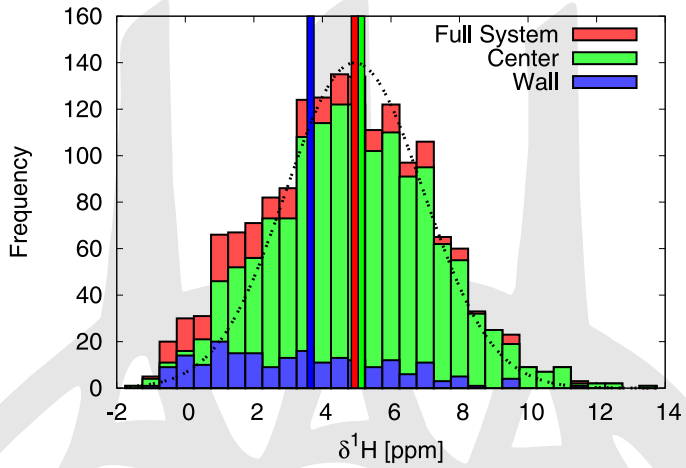

Fig. 6. Calculated ^{1}H NMR shift distribution of confined water. The ordinate is the occurence of the shifts for various δ values. $\delta = 3.65$ ppm is the averaged value for the water within 3 Å proximity to the walls (blue), $\delta = 4.94$ ppm is the global average of the whole system (red), and $\delta = 5.13$ ppm is the average shift of the water at the center of the pore (green). The dashed curve represents a gaussian centered at $\delta = 4.94$ ppm (black).

Our averaged NMR shifts imitate this process (as shown in Fig. 5) in such a way that the δ value continually goes up from 2 ppm to 5.5 ppm as increasing thickness of the film which starts from the wall (0 Å). This denotes that the bonding between water and the silanols becomes less and less dominating which leads to the the growing of the shifts until $x = 5.5$ Å. A plateau arises at 5.5 Å $< x <$ 11 Å reflecting the water molecules at the center region are mostly bounded to each other and not influenced by the walls.

Figure 6 illustrates the spacial distribution of the ^{1}H NMR shifts inside the cell. Those water molecules situated within 3 Å proximity to the silica wall are denoted as wall water, and the rest are considered to be center water. In this way, the confined water is divided into 3 layers, silanol-water interface (wall water), water-water (center

water) and water-silanol interface (wall water). The computed global average value of the ^{1}H chemical shift for all the water inside this cell is 4.94 ppm, the averaged water shift in the close region of walls is 3.65 ppm, and that for the water in the core area is 5.13 ppm. Comparing the whole distribution with a Gaussian centered at the global average δ value 4.94 ppm, we can easily see that more water molecules fall into the up field in the proximity of silanols. Most wall water resides at the left half of the graph with $\delta \leq 4.94$ ppm. The overall average shift of the system moves towards lower δ (upper field) under the effects of silica walls. This gives further evidence that the silanol groups play a twisting role for the water-water hydrogen bonding network in the interfacial region [21].

4. Conclusion

In this paper, DFT based molecular dynamics simulations and first principles NMR chemical shift calculations are applied on a simplified surface model based on the structural properties of the MCM-41 pore. Our calculations demonstrate the strong influence of spatial confinement on the structure and dynamical properties of water.

On the structural level, we see a strong influence on the ^{1}H chemical shifts of the confined water. While at the center of the pore a 0.5 ppm increased chemical shift compared to bulk water is found, the chemical shift gradually decreases when approaching the wall, until it reaches a value 3 ppm below bulk water reference. This implies an enhanced hydrogen bonding network for the water at the center, and a strongly weakened network close to the silica-water interface. In the density profile, distinctive peaks appear next to the wall, indicating a structuring of the water by the wall geometry. By calculating average chemical shifts for fictitious water films at the wall, we can see a change from low chemical shifts for thin films towards bulk water like chemical shifts for a film thickness above 4 Å. This is in good agreement with a previous experimental model on the gradual filling of nanopores.

With respect to the dynamical behavior, we see a decrease in the diffusion rate by a factor of 4 when comparing to bulk water values.

Acknowledgement

This work has been supported by the German Research Foundation (DFG) under grants SE 1008/5 and 1008/8. Computing infrastructure was provided by the Northern German Supercomputing Alliance (HLRN) under grant HLRN/bec00073 and ZEDAT high-performance cluster in Freie Universität Berlin. We thank the German academic exchange service (DAAD) for a RISE internship.

References

1. B. Grünberg, T. Emmler, E. Gedat, I. Shenderovich, G. H. Findenegg, H. H. Limbach, and G. Buntkowsky, Chem. Eur. J. **10** (2004) 5689.
2. A. Faraone, L. Liu, C. Mou, P. Shih, J. Copley, and S. Chen, J. Chem. Phys. **7** (2003) 3963.
3. F. Mansour, R. M. Dimeo, and H. Peemoeller, Phys. Rev. E **66** (2002) 041307.

4. C. Pantalei, R. Senesi, C. Andreani, P. Sozzani, A. Comotti, S. Bracco, M. Beretta, Mario, P. Sokol, and G. Reiter, Phys. Chem. Chem. Phys. **13** (2011) 6022.
5. R. Mancinelli, S. Imberti, A. K. Soper, K. H. Liu, C. Y. Mou, F. Bruni, and M. A. Ricci, J. Phys. Chem. B **113** (2009) 16169.
6. P. Smirnov, T. Yamaguchi, S. Kittaka, S. Takahara, and Y. Kuroda, J. Phys. Chem. B **104** (2000) 5498.
7. V. Ostroverkhov, G. A. Waychunas, and Y. R. Shen, Phys. Rev. Lett. **94** (2005) 046102.
8. V. Kocherbitov and V. Alfredsson, J. Phys. Chem. B **112** (2007) 12906.
9. I. G. Shenderovich, D. Mauder, D. Akcakayiran, G. Buntkowsky, H. H. Limbach, and G. Findenegg, J. Chem. Phys. B **111** (2007) 12088.
10. X. S. Zhao, G. Q. Lu, A. K. Whittaker, G. J. Millar, H. Y. Zhu, J. Chem. Phys. B **101** (1997) 6525.
11. D. W. Hwang, A. K. Sinha, C. Y. Cheng, T. Y. Yu, and L. P. Hwang, J. Phys. Chem. B **105** (2001) 5713.
12. P. Gallo, M. Rovere, and S. H. Chen, J. Phys.: Condens. Matter **24** (2012) 064109.
13. S. Pizzanelli, S. Kababya, V. Frydman, M. Landau, and S. Vega, J. Phys. Chem. B **109** (2005) 8029.
14. E. P. Ng and S. Mintova, Micropor. Mesopor. Mat. **14** (2008) 1.
15. K. Shirono and H. Daiguji, J. Phys. Chem. B **111** (2007) 7938.
16. K. Kleestorfer, H. Vinek, and A. Jentys, J. Mol. Catal. A: Chem. **166** (2001) 53.
17. S. Takahara, N. Sumiyama, S. Kittaka, T. Yamaguchi, B. Funel, and M. Claire, Adsorption **109** (2005) 5814.
18. A. Lerbret, G. Lelong, P. Mason, M. L. Saboungi, and J. Brady, Food Biophys. **6** (2011) 233.
19. M. E. Tuckerman, *Statistical Mechanics: Theory and Molecular Simulation*, Oxford Graduate Texts, Oxford University Press Inc., New York (2010).
20. A. R. Bizzarriand and S. Cannistraro, J. Phys. Chem. B **106** (2002) 6617.
21. P. Gallo, M. Rapinesi, and M. Rovere, J. Chem. Phys. **117** (2002) 7.
22. H. E. Gottlieb, V. Kotlyar, and N. Abraham, J. Org. Chem. **62** (1997) 7512.
23. D. R. Banyai, T. Murakhtina, and D. Sebastiani, Magn. Reson. Chem. **48** (2010) S56.
24. P. A. Bonnaud, B. Coasne, and R. J-M. Pellenq, J. Phys.-Condens. Mat. **22** (2010) 284110.
25. A. A. Milischuk and B. M. Ladanyi, J. Chem. Phys. **135** (2011) 174709.
26. T. G. Lombardo, N. Giovambattista, and P. G. Debenedetti, Faraday Discuss. **141** (2009) 359.
27. R. Mancinelli, F. Bruni, and M. A. Ricci, J. Phys. Chem. Lett. **1** (2010) 1277.
28. R. Mills, J. Phys. Chem. **77** (1973) 685.
29. M. Sulpizi, M. Gaigeot, and M. Sprik, J. Chem. Theory **8** (2012) 1037.
30. Computer code CP2K, available from www: www.cp2k.org/.
31. A. D. Becke, Phys. Rev. A **38** (1988) 3098.
32. S. Goedecker, M. Teter, and J. Hutter, Phys. Rev. B **54** (1996) 1703.
33. S. Grimme, J. Comput. Chem. **27** (2006) 1787.
34. J. VandeVondele and J. Hutter, J. Chem. Phys. **127** (2007) 114105.
35. D. Sebastiani and M. Parrinello, Chem. Phys. Chem. **3** (2002) 675
36. J. Schmidt, J. VandeVondele, I. F. Kuo, D. Sebastiani, J. I. Siepmann, J. Hutter, and C. J. Mundy, J. Phys. Chem. B **113** (2009) 11959.
37. J. Schmidt, A. Hoffmann, H. W. Spiess, and D. Sebastiani, J. Phys. Chem. B **110** (2006) 23204.
38. T. Murakhtina, J. Heuft, J. E. Meijer, and D. Sebastiani, Chem. Phys. Chem. **7** (2006) 2578.
39. Y. J. Lee, T. Murakhtina, D. Sebastiani, and H. W. Spiess, J. Am. Chem. Soc. **129** (2007) 12406.
40. A. Hoffmann, D. Sebastiani, E. Sugiono, K. S. Kim, H. W. Spiess, and I. Schnell, Chin. Phys. Lett. **388** (2004) 164.
41. K. Münnemann and H. W. Spiess, Nature Phys. **7** (2011) 522.
42. T. Metzroth, A. Hoffmann, R. Martín-Rapún, M. M. J. Smulders, K. Pieterse, A. R. A. Palmans, J. A. J. M. Vekemans, E. W. Meijer, H. W. Spiess, and J. Gauss, Chem. Sci. **2** (2011) 69.

5.3 Paper III

This paper is a review paper and contains no original scientific information. It is available online for free under `http://www.bunsen.de/bunsen_media/Downloads/BUNSEN_MAGAZIN/Erschienene+BM/BuMa_2013_01.pdf` or by request.

5.4 Paper IV

Reproduced from Angew. Chem. Int. Ed. 2013, 52, 1813−1816 (4) with permission from Wiley-VCH Verlag GmbH & Co. KGaA, Weinheim

Molecular Dynamics Simulations

DOI: 10.1002/anie.201204532

An Ab Initio Microscope: Molecular Contributions to the Femtosecond Time-Dependent Fluorescence Shift of a Reichardt-Type Dye**

*Christoph Allolio, Mohsen Sajadi, Nikolaus P. Ernsting, and Daniel Sebastiani**

Despite decades of effort, the properties of liquid water are not fully understood. In recent years it was found that geometric confinement has a strong effect on water, making it quite different from the bulk.[1] To understand protein functionality, agglomeration, and folding, as well as DNA stability, it appears to be essential to explicitly consider the presence of water.[2]

With current IR-based spectroscopic techniques, it is possible to monitor rapid photochemical reactions.[3] These techniques are, however, severely limited by strong absorption due to water, in addition to spectral crowding. To overcome these limitations, compounds with isotopically substituted carbonyl groups have been used.[4] IR spectroscopy observes the hydrogen-bond network indirectly by its coupling to the vibrational modes. Fluctuations of the hydrogen-bond network can be directly measured by THz spectroscopy which probes the dielectric bulk response.[5] Inside biomolecules or confinements, the absorption background of water can be entirely avoided when the fluorescence of a suitably placed chromophore is monitored. For this purpose, dyes are employed whose fluorescence depends strongly on solvent polarity.[6] In this context, the molecular probe *N*-methyl-6-oxyquinolinium betaine (MQ) is especially attractive because of its small size and water solubility, allowing insertion into DNA or proteins. Structurally, it resembles the polarity indicator dye introduced by Reichardt and coworkers.[7] The local THz spectrum, up to the far-IR intramolecular modes, can then be extracted almost quantitatively from the time-dependent Stokes shift (TDSS) of its fluorescence as measured by femtosecond spectroscopy. The connection between TDSS data of MQ and the THz spectrum of its surroundings has been established by simple dipolar continuum theory.[8] It should be noted that the Stokes shift of the chromophore represents only an indirect measurement of the water dynamics. In addition, the presence of the chromophore has the potential of affecting this very water dynamics to a certain extent.

However, the time-dependent dielectric response can be traced back to the structure and dynamics around the molecular probe in atomistic detail with the help of molecular dynamics simulations in combination with the experimentally observed evolution of the Stokes shift.

Published attempts at describing time-dependent solvation with molecular dynamics used either a quantum mechanics/molecular dynamics (QM/MM) approach, including only the solute and a few water molecules in a quantum mechanical treatment,[9] or a model potential derived from quantum mechanical calculations of the chromophore.[10] In our approach, we use density functional theory (DFT) for solute and solvent, which is known to yield an accurate picture of solvent effects and the dynamics of hydrogen-bond networks, also for excited-state solutes.[11] Instead of the dielectric linear response of the solvent or the time-dependent solvation energy, we compute the time-dependent fluorescence emission wavelength directly from nonequilibrium MD. This allows us to simulate the full TDSS experiment from first principles—without preadjusted parameters and assumptions about the solvent response, including full electronic polarization and all intramolecular degrees of freedom. We performed molecular dynamics simulations in the T_1 triplet state, providing an efficient approach for excited-state dynamics. In a previous paper we verified that the dipole moment and forces of the S_1 state of MQ are equally well described by both the T_1 state and time-dependent (TD-) DFT.[12] The Stokes shifts in turn were computed by TD-DFT in order to obtain more accurate excitation energies. For computational details see the Supporting Information.

MQ is formally a zwitterionic molecule with a large dipole moment (Figure 1). In agreement with previous static calculations the MD simulations performed here yield strong hydrogen bonds at the electron-rich MQ oxygen, which are weakened upon electronic excitation of the molecule.[12] The radial distribution functions show that the coordination number of 3 remains unaffected by this weakening (see the Supporting Information). When visually examining the trajectory, we find MQ to be inside a broad cavity in the solvent, generated by its hydrophobic planar π-system.

MQ shows a strong reduction of the molecular dipole moment upon electronic excitation (Figure 1). We previously computed this change of dipole moment to be from 10.2 D to 6.8 D in the gas phase.[12] In aqueous solution, we find a reduction from 22 D to 14 D (computed from Wannier centers, averaged over ten conformations in the corresponding relaxed trajectories.) As the large ground-state dipole moment induces a strong alignment of the solvent molecules

[*] C. Allolio, Prof. Dr. D. Sebastiani
Department of Chemistry
Martin-Luther Universität Halle-Wittenberg
von-Danckelmann-Platz 4, 06120 Halle/Saale (Germany)
E-mail: daniel.sebastiani@chemie.uni-halle.de
Dr. M. Sajadi, Prof. Dr. N. P. Ernsting
Department of Chemistry, Humboldt-Universität zu Berlin
Brook-Taylor-Strasse 2, 12489 Berlin (Germany)

[**] This work was supported by the German Research Foundation (DFG) under grant SE 1008/8. Computing infrastructure was provided by the Northern German Supercomputing Alliance (HLRN) under grant HLRN/bec00073.

Supporting information for this article is available on the WWW under http://dx.doi.org/10.1002/anie.201204532.

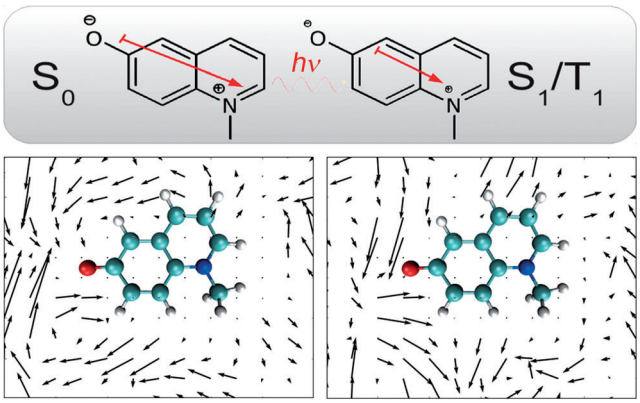

Figure 1. Schematic illustration of the change in the dipole moment upon electronic excitation of MQ (top, not to scale), averaged orientations of water molecules around solvated MQ in the ground (left) and in the excited state (right). The length of the arrows corresponds to a preferential orientation, obtained by ensemble averaging over the MD trajectory. For details see the Supporting Information.

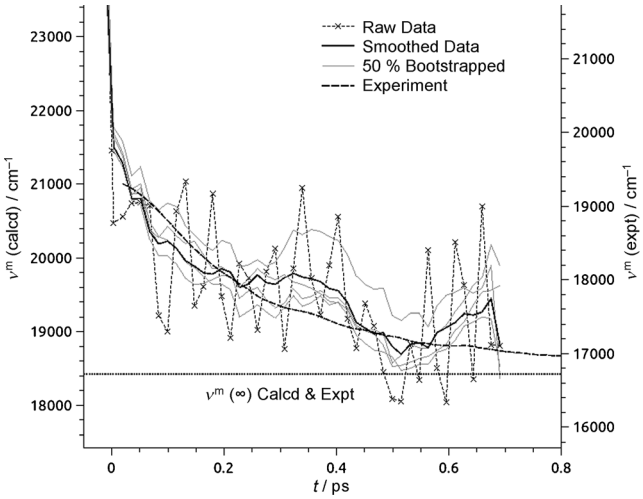

Figure 2. Dynamics of the Stokes shift as obtained by averaging ten trajectories and smoothing by 10 point moving-window averaging (black, left axis), Stokes shift after removal of five random trajectories (gray lines, left axis), experimental data[14] (dashed black line, right axis); data is referenced to $\nu(t{=}\infty)$ in both cases (dotted base line).

around the solute dipole, excitation of MQ reduces the statistical ordering for the water dipoles. This reduction of the ordering due to the weaker dipolar interaction is illustrated in Figure 1 by means of the average orientations of the water molecules around MQ. In the ground state (left) the distribution of water molecules is aligned with the field lines of the MQ dipole, with a reduced amplitude at the nitrogen site. In order to quantify the orientational response of the solvation structure to the excitation of MQ (right), we compute an order parameter λ, inspired by the dipole–dipole interaction energy.

$$\lambda = \left\langle \frac{\varepsilon \cdot \mathbf{p}_{H_2O}}{\|\varepsilon\| \cdot \|\mathbf{p}_{H_2O}\|} \right\rangle \qquad \varepsilon = -\nabla\left(\frac{1}{\|\mathbf{r}_N - \mathbf{r}\|} - \frac{1}{\|\mathbf{r}_O - \mathbf{r}\|}\right) \tag{1}$$

For simplicity, we use the geometric orientation of water molecules instead of the actual physical dipoles for $\mathbf{p}_{H_2O}$ and the electric field ε of point charges at the oxygen and nitrogen atoms. Our first-principles MD simulations yield $\lambda = 0.12$ in the ground state and $\lambda = 0.08$ upon excitation. We find the average vertical $S_0 \rightarrow S_1$ excitation energy to be 2.97 eV—close to the experimental value of 3.04 eV.[13] In the excited state the electronic excitation energy is found to be 2.29 eV, 0.2 eV higher than the experimentally observed value. We attribute this difference to the fact that in our triplet model, the chromophore moves on a slightly different energy surface than in the true S_1 state.

In our simulation, we switch from the ground state to the excited state and then follow the solvent relaxation by means of the vertical de-excitation energy $\nu(t)$. In order to increase ergodicity, we sample from ten independent trajectories started at different points of the equilibrated ground-state trajectory to yield an ensemble average for the evolution of the fluorescence wavenumber $\nu^m(t)$. To provide an estimate of the uncertainty inherent in the limited sampling, we have computed $\nu^m(t)$ based on half of the trajectories (gray lines in Figure 2, multiple random selection of trajectory subset). The time-dependent Stokes shift of our ab initio MD is shown in in Figure 2 (black line). When we correct for the different equilibrium de-excitation energy ν^m_∞ we find good agreement with experiment. The computed Stokes shift exhibits oscillations with a period of about 350 fs, which are not visible in experiment. We believe they may be due to finite size effects.

A complementary approach to characterize solvation dynamics is the relaxation from excited-state equilibrium to ground-state equilibrium. The shape and relaxation time of the reversed time-dependent Stokes shift, that is, an "anti-Stokes" shift, is virtually identical to the fluorescence stokes shift (see Figure S7 in the Supporting Information).

Having obtained a good reproduction of the experimental relaxation, we further decompose the total Stokes shift into several contributions. For the intramolecular part, we compute the Stokes shift using only the isolated MQ in geometries extracted from the (fully solvated) MD trajectory. We find that the de-excitation energy of isolated MQ does not decrease over time; instead it oscillates with a frequency of about 600 cm^{-1}, other modes being less discernible. Experimentally, the intramolecular vibrational modes obtained from the maxima of stimulated emission[8] also are present in this region: prominent peaks occur at 460 cm^{-1}, 520 cm^{-1}, and 600 cm^{-1} (see the Supporting Information).

Shifting from the chromophore to the solvent, the question arises which water molecules provide the largest contribution to the TDSS. The solvation energy difference $\Delta E_{Solv}(t)$ for a cluster of MQ with surrounding water molecules is just the difference between the $S_1 \rightarrow S_0$ transition energies of the isolated MQ molecule and the cluster; therefore intramolecular oscillations of MQ are mapped out.

We compute $\Delta E_{Solv}(t)$ of solvent clusters extracted from our trajectories, partitioning the solvating water molecules into three groups (Figure 3): group a: water molecules that are located in a torus 10 Å in diameter centered at the N–O axis of MQ (for details see the Supporting Information);

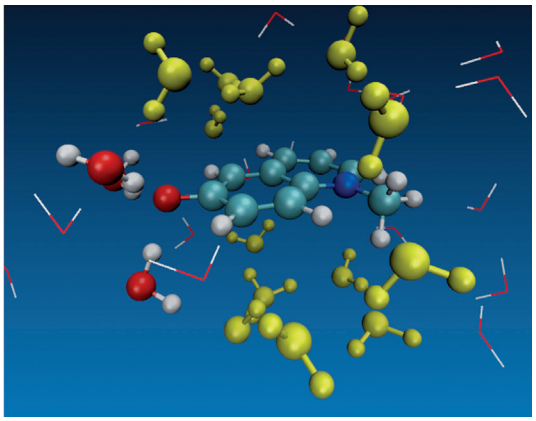

Figure 3. The first solvation shell of MQ and its components: Water molecules in a torus around the N—O axis of MQ (yellow balls, type a in Figure 4), H_2O molecules hydrogen-bonded to the MQ oxygen terminus (red and white balls, type b), and the entire first solvation shell (rods, type c).

group b: water molecules that are hydrogen-bonded to MQ; group c: the full first solvation shell of water. This partitioning of the first solvation shell is motivated by experimental results indicating that the Stokes shift is mostly caused by dipolar relaxation of water molecules.[8] Hence we choose the water molecules in the first solvation shell that are most affected by the change in the dipolar field of MQ.

We find that within the examined clusters, only the water molecules in group a shows considerable net relaxation behavior. The contribution of the water molecules to the Stokes shift amounts to about 0.3 eV, which represents a substantial part of the observed dynamic Stokes shift. For the water molecules in group b we find a strong contribution to the static ΔE_{Solv} (Figure 4, dashed gray line); this molecular solvatochromism is consistent with our previous results.[12] Instead of a relaxation, we find an increase in the solvation energy in first 0.1 ps. Finally, for water molecules in group c no net relaxation is visible after 0.7 ps, despite a strong initial response within the first 0.1 ps.

Summarizing the above, the dielectric effects of MQ solvation clearly extend beyond the first solvation shell, as the complete relaxation of ΔE_{Solv} is considerably larger than the contribution from the first solvation shell only. Extrapolating ΔE_{Solv} of the cluster decompositions, we estimate that the aqueous dielectric screening of the MQ probe extends roughly 8 Å into the solution. When examining the time evolution of the three hydrogen bonds connected to the MQ oxygen, we find that a rapid elongation of these bonds occurs (see the Supporting Information). The weakening of these hydrogen bonds occurs within 0.2 ps after the excitation; this local dynamics could in principle explain the initial Stokes relaxation. However, a direct causality between the geometric motif and the MQ excitation energy is not confirmed by the cluster decomposition (dashed gray line in Figure 4.) Only the full solution is capable of reproducing the experimental relaxation.

In conclusion, our ab initio molecular dynamics simulations in combination with TD-DFT calculations are able to explain the experimentally observed femtosecond time

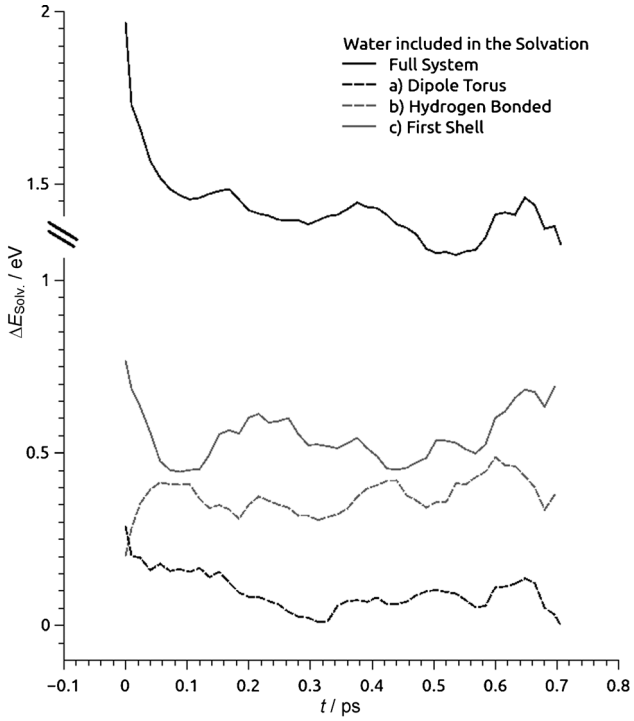

Figure 4. Computed time evolution of the solvation energy $\Delta E_{Solv}(t)$ for the three types of water molecules around MQ, for the subsystems extracted from the fully solvated MQ trajectory. For definitions of the subsystems see Figure 3 and the main text.

dependence of the fluorescence Stokes shift of solvated *N*-methyl-6-oxyquinolinium betaine at the molecular level. By decomposing the MD trajectories, we show that an important contribution to the time-dependent Stokes shift originates from a group of water molecules that strongly interact with MQ's molecular dipole (located inside a torus around the aromatic core of MQ). Our MD simulations give a molecular, first-principles justification to interpretations based on dipolar relaxation: Molecular excitation of MQ causes a loss of dipolar orientation that extends through the solution, which we describe by a suitable order parameter λ. For the relaxation of the ground state from the excited-state equilibrium, we predict a very similar behavior of the relaxation dynamics. As our method of calculating the time-dependent Stokes shift of MQ does not use any adjustable parameters, it can be readily transferred to more complex systems, in particular biomolecules.

Received: June 11, 2012
Revised: September 30, 2012
Published online: January 2, 2013

Keywords: density functional calculations · dielectric properties · emission spectroscopy · laser spectroscopy · molecular dynamics

[1] a) M. Fayer, N. E. Levinger, *Annu. Rev. Anal. Chem.* **2010**, *3*, 89; b) J. C. Rasaiah, S. Garde, G. Hummer, *Annu. Rev. Phys. Chem.* **2008**, *59*, 713.

[2] a) Y. Levy, J. N. Onuchic, *Annu. Rev. Biophys. Biomol. Struct.* **2006**, *35*, 389; b) D. Lucent, V. Vishal, V. S. Pande, *Proc. Natl. Acad. Sci. USA* **2007**, *104*, 10430; c) K. M. Ravikumar, W. Hwang, *J. Am. Chem. Soc.* **2011**, *133*, 11766; d) P. Ball, *ChemPhysChem* **2008**, *9*, 2677; e) S. K. Pal, A. H. Zewail, *Chem. Rev.* **2004**, *104*, 2099; f) Y. H. P. Auffinger, *Curr. Opin. Struct. Biol.* **2007**, *17*, 325; g) P. Ball, *Chem. Rev.* **2008**, *108*, 74.

[3] a) K. Ataka, T. Kottke, J. Heberle, *Angew. Chem.* **2010**, *122*, 5544; *Angew. Chem. Int. Ed.* **2010**, *49*, 5416; b) K. Adamczyk, M. Prémont-Schwarz, D. Pines, E. Pines, E. T. J. Nibbering, *Science* **2009**, *326*, 1690.

[4] M. Horch, L. Lauterbach, M. Saggu, P. Hildebrandt, F. Lendzian, R. Bittl, O. Lenz, I. Zebger, *Angew. Chem.* **2010**, *122*, 8200; *Angew. Chem. Int. Ed.* **2010**, *49*, 8026.

[5] a) U. Heugen, G. Schwaab, E. Bründermann, M. Heyden, X. Yu, D. M. Leitner, M. Havenith, *Proc. Natl. Acad. Sci. USA* **2006**, *103*, 12301; b) M. Heyden, J. Sun, S. Funkner, G. Mathias, H. Forbert, M. Havenith, D. Marx, *Proc. Natl. Acad. Sci. USA* **2010**, *107*, 12068; c) N. E. Levinger, *Science* **2002**, *298*, 1722.

[6] a) M. L. Horng, J. A. Gardecki, A. Papazyan, M. Maroncelli, *J. Phys. Chem.* **1995**, *99*, 17311; b) G. Haran, W.-D. Sun, K. Wynne, R. M. Hochstrasser, *Chem. Phys. Lett.* **1997**, *274*, 365; c) A. Dallmann, M. Pfaffe, C. Mügge, R. Mahrwald, S. A. Kovalenko, N. P. Ernsting, *J. Phys. Chem. B* **2009**, *113*, 15619.

[7] a) K. Dimroth, C. Reichardt, T. Siepmann, F. Bohlmann, *Justus Liebigs Ann. Chem.* **1963**, *661*, 1.

[8] a) J. L. Pérez Lustres, S. A. Kovalenko, M. Mosquera, T. Senyushkina, W. Flasche, N. P. Ernsting, *Angew. Chem.* **2005**, *117*, 5779; *Angew. Chem. Int. Ed.* **2005**, *44*, 5635; b) M. Sajadi, Y. Ajaj, I. Ioffe, H. Weingärtner, N. P. Ernsting, *Angew. Chem.* **2010**, *122*, 464; *Angew. Chem. Int. Ed.* **2010**, *49*, 454; c) J. L. Pérez-Lustres, F. Rodriguez-Prieto, M. Mosquera, T. A. Senyushkina, N. P. Ernsting, S. A. Kovalenko, *J. Am. Chem. Soc.* **2007**, *129*, 5408.

[9] a) V. Barone, J. Bloino, S. Monti, A. Pedone, G. Prampolini, *Phys. Chem. Chem. Phys.* **2011**, *13*, 2160; b) M. Wohlgemuth, V. Bonacić-Koutecky, R. Mitrić, *J. Chem. Phys.* **2011**, *135*, 054105; c) J. Grilj, E. N. Laricheva, M. Olivucci, E. Vauthey, *Angew. Chem.* **2011**, *123*, 4589; *Angew. Chem. Int. Ed.* **2011**, *50*, 4496.

[10] a) J. W. Park, H. W. Kim, C. ik Song, Y. M. Rhee, *J. Chem. Phys.* **2011**, *135*, 014107; b) R. Jimenez, G. R. Fleming, P. V. Kumar, M. Maroncelli, *Nature* **1994**, *369*, 471.

[11] a) M. Böckmann, N. L. Doltsinis, D. Marx, *J. Phys. Chem. A* **2010**, *114*, 745; b) I. Tavernelli, M.-P. Gaigeot, R. Vuilleumier, C. Stia, M.-A. Herv du Penhoat, M.-F. Politis, *ChemPhysChem* **2008**, *9*, 2099; c) P. R. L. Markwick, N. L. Doltsinis, *J. Chem. Phys.* **2007**, *126*, 175102; d) L. Bernasconi, M. Sprik, J. Hutter, *J. Chem. Phys.* **2003**, *119*, 12417; e) M. Iannuzzi, T. Chassaing, T. Wallman, J. Hutter, *Chimia* **2003**, *59*, 499.

[12] C. Allolio, D. Sebastiani, *Phys. Chem. Chem. Phys.* **2011**, *13*, 16395.

[13] E. Bardez, A. Chatelain, B. Larrey, B. Valeur, *J. Chem. Phys.* **1994**, *98*, 2357.

[14] M. Sajadi, M. Weinberger, H.-A. Wagenknecht, N. P. Ernsting, *Phys. Chem. Chem. Phys.* **2011**, *13*, 17768.

5.5 Paper V

Reprinted with permission from (5)
H-Bonding Competition and Clustering in Aqueous LiI
Christoph Allolio, Nora Salas-Illanes, Yogesh S. Desmukh, Michael Ryan Hansen, and Daniel Sebastiani
The Journal of Physical Chemistry B 2013 117 (34), 9939-9946

THE JOURNAL OF PHYSICAL CHEMISTRY B

Article

pubs.acs.org/JPCB

H-Bonding Competition and Clustering in Aqueous LiI

Christoph Allolio,[†] Nora Salas-Illanes,[†] Yogesh S. Desmukh,[‡,¶] Michael Ryan Hansen,[§,¶] and Daniel Sebastiani*[,†]

[†]Department of Chemistry, Martin-Luther Universität Halle-Wittenberg, von-Danckelmann-Platz 4, 06120 Halle/Saale, Germany

[‡]Department of Chemical Engineering and Chemistry, Eindhoven University of Technology, P.O. Box 513, Eindhoven, Netherlands

[¶]Dutch Polymer Institute (DPI), P.O. Box 902, 5600AX Eindhoven, The Netherlands

[§]Max Planck Institute for Polymer Research, Ackermannweg 10, 55128 Mainz, Germany

Supporting Information

ABSTRACT: We have characterized the structure and picosecond dynamics of the hydrogen bond network of solvated LiI by means of first-principles molecular dynamics simulations at ambient temperature. Our calculations reveal the qualitative differences of the network between low (1 M) and high (9 M) salt concentrations. In particular, we find the presence of fused Li^+ solvation shells at 9 M, meaning that a single water molecule is coordinated to two different Li^+ ions. This results in the formation of $(Li^+{\cdot}H_2O)_n$ chains, dominating over conventional ion pairing. We report experimental and simulated NMR chemical shifts, which indicate a weakening of the hydrogen bond network, mainly within the first solvation shell of the I^- ions. In line with this finding, the local dynamics of this network reveal a competition between the chaotropic effects of I^- and the kosmotropic properties of Li^+ ions at an intermediate range. We find that the chaotropic effect of I^- reaches across several H-bonds into the solution, whereas the kosmotropic effect of Li^+ is more short ranged.

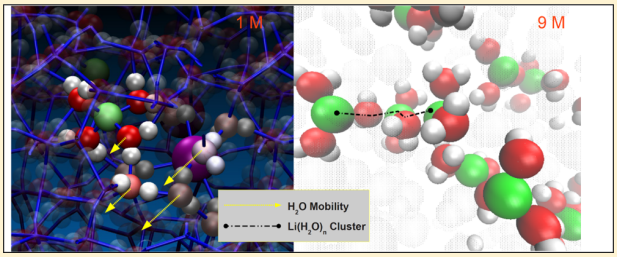

1. INTRODUCTION

The interaction of molecular and ionic solutes with water is one of the evergreens of structural chemistry and biochemistry. Increasing attention is currently focused on cooperative effects in this context, in particular, the influence of cosolvents on the solvation of a larger solute molecule. Historically, this is known as the Hofmeister effect, which was originally observed as the specific effect of different ions on the precipitation and dissolution of egg protein.[1] This effect has turned out to be of universal relevance to protein science[2] and is intrinsically related to the broader issue of the properties of water at interfaces and under confinement. Apart from biomolecules,[3−5] the dissolution of synthetic polymers is also strongly affected by the addition of salts.[6] Protein precipitation necessitates exclusion of a large part of water confined at the interface of the macromolecule.[7,8] Understanding modifications of the (local) hydrogen bond network by ions is therefore key to understanding Hofmeister effects. To improve our quantitative understanding, a variety of spectroscopic signatures of the hydrogen bond network under the influence of ions may be assembled to form a coherent atomistic and thermodynamic picture. At present, this picture is far from complete, as evidenced by the still ongoing controversy on how far the influence of the ions themselves on the bulk solution reaches.[3,9] However, valuable insights have been gained from (ultrafast) infrared spectroscopy[10−12] as well as NMR,[4,13,14] and THz[15] and neutron scattering.[16,17] Simple aqueous solutions of monovalent ions have undergone extensive research in the past.[18−23] Despite the considerable shortcomings of classical force fields for high concentrations of salts,[24,25] studies of concentrated aqueous salt solutions using ab initio molecular dynamics are still rare in the literature, the main focus of reasearch having been studies of the isolated ions or halide acids.[26−37] While the problems associated with long-range electrostatic interactions in periodic systems make this partially understandable, we think that important insight can be gained from the interplay of ions in such systems, especially at high concentrations. This is particularly true in the case of LiI because it combines a kosmotropic, that is, a H-bond network reinforcing cation with a chaotropic anion having the opposite effect, making it a reference in the search for cooperative effects,[38] as well as specific phenomena caused by overlapping solvation structures. In addition, LiI has recently been found to facilitate polyamide processing when used in high concentrations,[39] so that the question arises by what mechanism a highly concentrated LiI solution dissolves the polymer. ^{1}H NMR chemical shifts of aqueous solutions of chaotropic and kosmotropic ions are a sensitive measure of an ion's effect on hydrogen bonding. We here present a combined theoretical and experimental study of the solvation of LiI, focusing on the structure and dynamics of the hydrogen bond network. We begin by describing the structure of the ionic solvation shells

Received: April 4, 2013
Revised: August 2, 2013
Published: August 2, 2013

   dx.doi.org/10.1021/jp4033468 | J. Phys. Chem. B 2013, 117, 9939−9946

and their supramolecular organization. Next, we examine the hydrogen bond network itself, using the trends in experimental and simulated ^{1}H NMR chemical shifts as a guide for our description. Finally, we examine the dynamic interactions of the solvated ions with the hydrogen bond network and their competing effects on its stability.

2. THEORETICAL METHODS

Initially, we carried out classical MD simulations on three boxes of side length 11.84 Å containing 55 water molecules, 53 water molecules and one ion pair, and 37 water molecules and 9 ion pairs. The densities of the boxes were set to 0.99, 1.09, and 1.87 g/cm^3 according to an empirical polynomial fit from literature values for LiI at 25 °C[40] and adjusting the baseline for the equilibrium density of BLYP-D water at 0.991 g/cm^3.[41] In a first step, we pre-equilibrated the systems using a Kirkwood–Buff-type force field, which is tuned for highly concentrated aqueous solutions of monovalent ions.[42−44] For water, we used the SPC/E model.[45] Subsequently, ab initio simulations of 5 ps were carried out for each box, employing a DZVP-MOLOPT[46] basis set with GTH[47,48] pseudopotentials and the GAPW[49] method using a 320 Ry cutoff and a time step of 0.5 fs (Method I). In a third step, MD simulations of each system were done from 17 to 18 ps for 1 M LiI and H_2O to 29 ps for 9 M LiI, employing the GPW[50,51] method, with the BLYP-D dispersion-corrected[52] density functional[53,54] with a cutoff of 600 Ry. The basis set employed was a triple-ζ augmented basis for hydrogen and oxygen (TZV2PX) and a quadruple-ζ (QZV2P) basis set for the cation and DZVP-MOLOPT for anions[46] (Method II).

The system was kept at constant volume and at 350 K by means of a CSVR thermostat[55] with a time constant of 100 fs to compensate for overstructuring of water.[36,56] We ran the simulations with deuterated water and used a 1 fs MD time step.

The NMR chemical shift calculations were carried out using Method I[57] by averaging over 20−30 randomly sampled snapshots from the last several picoseconds of the (Method II) MD trajectories. For each concentration, the average is computed over more than 2000 instantaneous ^{1}H chemical shifts. The use of deuterated water affects only the dynamic of the MD but no structural aspects, in particular, neither the magnetic perturbation Hamiltonian nor the electronic ground state, thereby yielding identical chemical shifts to that of protons.[36] All computations were done using the CP2K software package.[58] We used Method I as the PSP of hydrogen has no nonlocal part and the method has previously been employed successfully for proton shifts.[59] Results are easily comparable to PW/PSP results, yielding especially a good convergence for the polarization due to the plane wave description of the diffuse "soft" part of the density.

3. RESULTS AND DISCUSSION

3.1. Ion Coordination. To compare the solvation shell structures with available experimental X-ray data, we compute radial distribution functions (RDFs) for the two concentrations. We find good agreement with previous X-ray diffraction and molecular dynamics studies regarding the position of the first peaks in the RDF (see the Supporting Information). Inspection of the trajectory reveals that many of the O−H bonds of neighboring H_2O do not point toward the iodide ion. This results in the first shell I−H coodination number (CN) being about 2 lower than the I−O CN at 1 M concentration. We therefore only consider protons in the first I−H shell to be H-bonded to I$^-$. Nevertheless, we count all water in the first I−O shell as coordinated. The weak H-bonding to iodide is also reflected by the large fluctuations in the number of coordinated waters (see Figure 1).

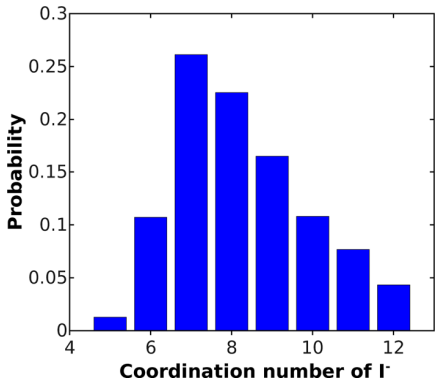

Figure 1. Distribution of the oxygen CNs of iodide in the 1 M LiI solution throughtout the trajectory. The distribution yields an average of 8.3; the equivalent distribution for Li$^+$ yields 91% of four-fold coordination and 9% of five-fold coordination.

The weak hydration of iodide is well-known and can be explained by its low net charge density owing to its large ionic radius.[9,60−62] Remarkably, the I−O CN actually increases with concentration. The solvation structure of iodide has already been studied using ab initio MD.[27,63,64] Good agreement with EXAFS and PES data was observed, and details including the asymmetry of the solvation shell and ion dipole moments have been discussed at length. These studies also have noted the weak H-bonding and the associated flexibility of the O−H angle (however finding a lower I−O CN for isolated I$^-$, possibly due to the aforementioned concentration effect). Therefore, we focus on the interplay between ions.

Although the water−ion ratio drops drastically from the 1 M solution (26.5) to the 9 M solution (2.0), the average Li−O CN of Li$^+$ remains 4. In addition, the average distance between Li$^+$ and the hydration water remains the same despite the increase in concentration (see the Supporting Information). The structure of the Li$^+$ coordination shells is found to be heavily influenced by ionic strength. It is tetrahedral at 1 M, consistent with other DFT studies.[28,29] However, it becomes deformed at 9 M concentration, with maxima at 90 and 180° angles (see Figure 2). We find this to be somewhat surprising as we had expected the change in shell geometry to go in step with a change in CN. While Li−I ion pairing is present, it is not sufficient to explain the deformation as it is found only in less than a third of the Li$^+$ ions.

The conservation of the four-fold coordination is achieved because most hydration polyhedra share one water molecule at some point in time. When lithium solvation shells are joined in this fashion, the oxygen of the shared water molecule will be facing both cations, forming what we call an oxygen bridge (see Figure 3, left). Oxygen bridges have been previously observed in both lithium iodide and lithium chloride.[65] As can be seen from the wide distribution of bridged Li$^+$ clusters (Figure 3, right), oxygen bridges connecting lithium ions are constantly formed and broken (the same is also true in the 1 M case, where we observed H_2O exchange). Half of the lithium ions in the sample share an oxygen with another lithium only for a few

dx.doi.org/10.1021/jp4033468 | J. Phys. Chem. B 2013, 117, 9939−9946

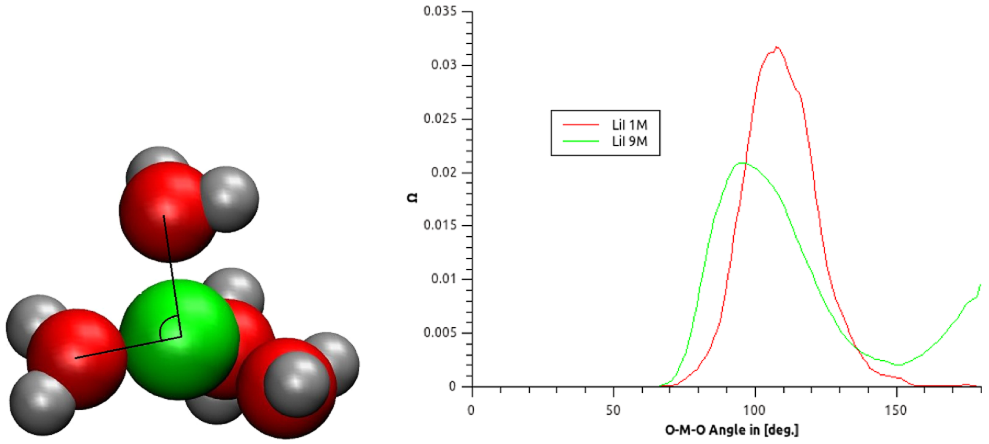

Figure 2. Angular distribution of the oxygen−metal−oxygen angle in the Li^+ coordination shell.

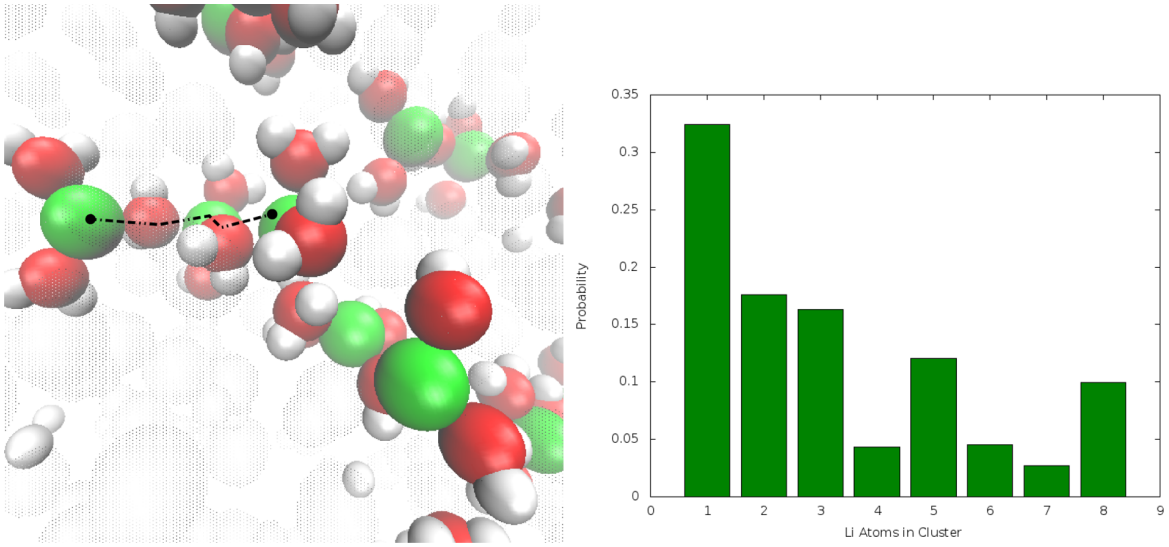

Figure 3. (Left) Cluster of five linked Li^+ ions at 9 M LiI. (Right) Probability for a Li^+ to be in a cluster of a given size; Li−O cutoff = 2.85 Å.

picoseconds before migrating to the next neighboring solvation shell.

This leads to fluctuations between 3 and 6 in the Li−O CN of the single Li^+ cations. The distribution of cluster sizes suggests the existence of preferred geometries with "magic numbers" of five or eight. Because the box size and sampling time are very restricted, we cannot distinguish this phenomenon with certainty from potential finite size effects. However, the observed condensation of Li^+ shells is plausible as it is also present in the structure of the $LiI{\cdot}3H_2O$ crystal.[66] In the $LiI{\cdot}3H_2O$ crystal, the lithium ion is at the center of a regular octahedron of oxygens with a Li−O distance of 2.14 Å. Each of the six oxygens in the coordination shell forms an oxygen bridge to the next ion. Thus, the water molecules in the $LiI{\cdot}3H_2O$ crystal are coordinated to two lithium cations and to two iodides via hydrogen bonds. The hydrogen bonding structure has been verified by solid-state IR.[67] The iodide in the crystal is surrounded by 12 oxygens at a distance between 3.70 and 3.75 Å.[66] In the crystal structure, the distance between Li^+ and iodide is 4.5 Å, close to the peak at 4.7 Å in the RDF_{Li-I} of our trajectory (see the Supporting Information). In the crystal, the I^- ions also form a chain parallel to the Li−O "polymer". We find both of these structural motifs in our simulation but in a disordered and transient form. An I^- chain is enforced already by the fact that the ion radius for I^- is about 2 Å. For a H_2O molecule to clearly separate the two ions, one would need a distance of about 7 Å of the I^- nuclei, or at least more than 5.5 Å, which puts just one atom's VdW radius in between. According to this definition, at 9 M concentration, all I^- are found to be in contact with other iodides. This pairing is merely due to spatial constraint and does not imply any favorable interaction. The crystal structure differs from our simulation in that it does not exhibit any cation−anion ion pairing. Another important difference is the Li−O CN of 4 found in our simulation as opposed to 6 in the crystal. As most of the water molecules in the 9 M solution are part of the Li^+ solvation clusters and the iodide ions move very slowly due to their large mass, the structure can be thought of as a dynamic intermediate between the crystal and liquid phases. For the water molecules not bound to Li^+, the ions hence represent a geometric confinement in the form of a hydrophilic matrix.

3.2. Hydrogen Bond Network: Concentration and Confinement. *3.2.1. Structure.* The hydrogen bonding network (HBN) of the LiI solutions represents our main

dx.doi.org/10.1021/jp4033468 | J. Phys. Chem. B 2013, 117, 9939−9946

interest as its modifications are thought to be responsible for the effects on protein precipitation and polymer dissolution. The RDF_{O-H} in Figure 4 for the 1 M LiI solution shows only

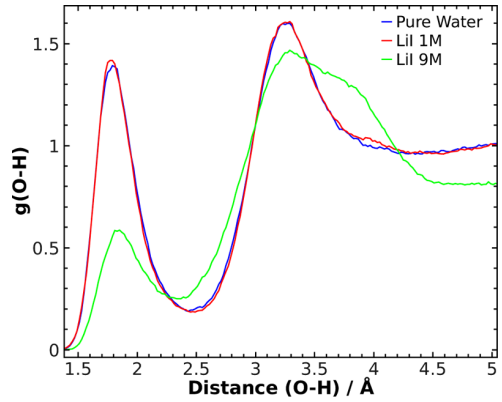

Figure 4. RDF_{O-H} for pure water, a 1 M LiI solution, and a 9 M LiI solution.

small deviations from pure water. In the 9 M LiI solution however, there is a significant weakening of H-bonding between water molecules, as evidenced by the far-smaller O−H coordination peak. The O−H CN for H-bonded water is 0.6 for water in the 9 M LiI solution, whereas for the 1 M LiI solution and pure water, the integral yields 2. This was also observed in LiCl solutions,[17,68] revealing a breakdown of the HBN at high concentrations as water molecules increasingly bond to ions.

One major reason for the weakening of the H-bond network at 9 M concentration has already been identified; most of the water oxygen atoms (>85%) become involved in Li^+ coordination and bridging; thus, fewer H-bonds between water molecules exist. It should be noted however that H-bonding between Li^+ coordinated oxygens and protons from other solvation shells is possible. In order to explore the possibilities of H-bonding, we have dissected the H-bonding topology (taking the H-bond definition from RDFs; see the Supporting Information). The three-dimensional HBN may be represented by a directed graph, where the nodes (H_2O molecules and ions) are connected by arrows. A small excerpt of the large complete graph for a given MD snapshot is depicted in Figure 5

As expected, the graph shows that the HBN is dominated by Li^+ solvation shell water molecules; these are interacting with each other. In the case of clusters not linked by oxygen bridges, the water molecules form H-bonds between Li^+ solvation shells. Even intrashell H-bonding is observed (see Figure 5, top). The I^- ions have a large number of H-bonds due to their large surface, so that the majority of water molecules are hydrogen-bonded to them (see Figure 5, bottom). The hydrogen bond network in the 9 M LiI solution can best be understood as a fusing "glue" between solvation shells.

3.2.2. NMR Chemical Shifts. We have performed experimental NMR measurements on aqueous solutions of a number of alkali halide salts at different concentrations (see Figure 6). These show that halide and alkali metal ions have a distinct effect on ^1H NMR chemical shifts that is in agreement with the Hofmeister series. Iodide is known to have a strong chaotropic behavior, and Li^+ is a more kosmotropic ion than Na^+. The strength of H-bonds can be measured by NMR chemical shifts,

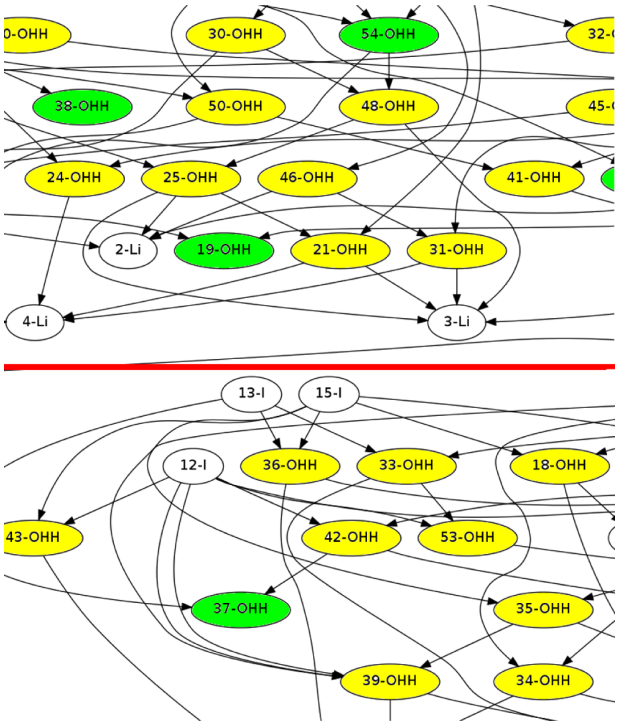

Figure 5. Patterns in the hydrogen bond network topology in a 9 M LiI solution. Water molecules in Li^+ solvation shells are colored yellow, "free" water molecules are colored green, and arrows are pointing from an electron pair donor (H-bond acceptor) to a H-bond donor in the style of dipolar bonding.

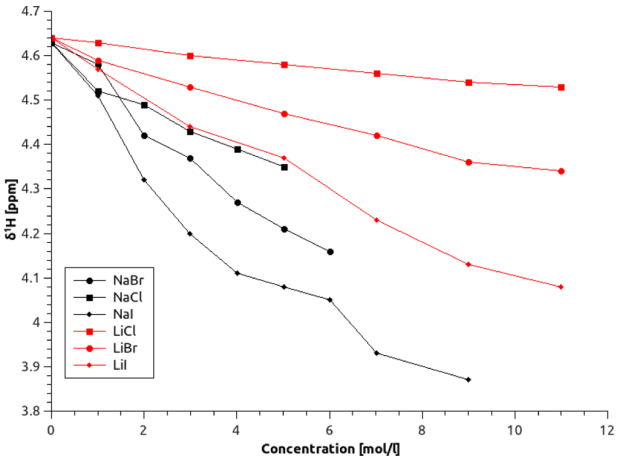

Figure 6. Experimental ^1H chemical shifts for different salt aqueous solutions of monovalent ions at concentrations from 1 to 12 mol/L in ppm. Full lines are meant as guides to the eye.

which exhibit a downfield shift proportional to the strength of the H-bond.[36,69−71] Thus, the NMR shifts give a direct confirmation of the Hofmeister effect in terms of hydrogen bonding.

The complex structural phenomena found at high concentrations of LiI, the general absence of a noticeable effect on ions at 1 M concentration, and the experimental linear dependence of the ppm shift on the concentration strongly suggest that the concentration effect on ^1H chemical shifts (and thus the H-bonding structure) is extremely short ranged. This means that

dx.doi.org/10.1021/jp4033468 | J. Phys. Chem. B 2013, 117, 9939−9946

the bulk water will not show a pervasive change in hydrogen bonding at all. Instead, it just disappears as more and more volume is being taken up by the ions. Figure 7 shows direct

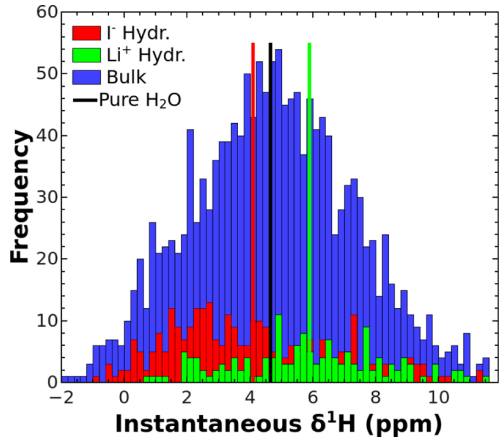

Figure 7. ^{1}H chemical shift distribution for hydrating water and bulk water in the 1 M LiI solution. The average for pure water is marked with a black line, while the chemical shift averages of lithium and iodide hydration water are marked with the green and red lines, respectively. We have used ion-oxygen cutoffs from the RDF.

support for this hypothesis as the water ^{1}H NMR shift average (and distribution) of protons beyond the first solvation shell is virtually identical to that of bulk water. Besides NMR shifts, other (far)-infrared spectroscopical data suggest the same conclusion.[9,15]

As reported in Table 1, the average chemical shift for all hydrogens in the 1 M LiI solution does not deviate strongly

Table 1. NMR Proton Chemical Shift (δ ^{1}H) Results for 1 and 9 M LiI and Pure Water[a]

δ ^{1}H/ppm	1 M LiI	9 M LiI
ab initio MD	4.72	3.62
experiment	4.55	4.16

[a]Computed NMR shifts are referenced to the H_2O trajectory, which in turn is set to the experimental shift of 4.65 ppm.

from that for pure water. Although ions have an important effect on the chemical shift of their direct hydration water (defined by the ion-oxygen RDF's first peak), the effects of Li^+ and iodide largely cancel out in the 1 M solution. Results are in good agreement with experiment in this case. The small deviation originates from an overly kosmotropic effect of Li^+ in the simulation, which is not observed in experiment. The small effect on NMR shifts indicates that the hydrogen bond network in the solution is not strongly perturbed, which is consistent with the RDF data seen before as well as topological analysis of the HBN. Thus, there is no indication of a long-range influence on the H-bond structure.

As in the 1 M solution, in the 9 M LiI solution, the upfield shift should originate from the water molecules directly involved in I^- hydration. Actually, we observe a collective effect of several iodides on a single water molecule (see Figure 8). Due to the large I^- solvation shell (see the Supporting Information), about 94% of the water molecules in the sample are coordinated to two or more I^- at the same time. Very few H_2O are coordinated to only one I^- (about 5%), and H_2O only

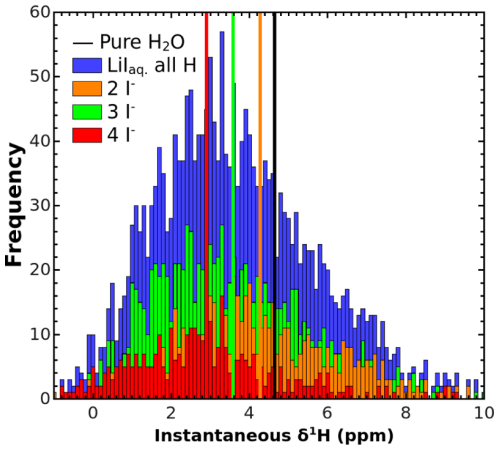

Figure 8. ^{1}H chemical shift distribution for all hydrogens in the 9 M LiI solution and for iodide hydration water, clasified by the number of iodides surrounding the water molecule (using the ion-oxygen first shell as a cutoff). The chemical shift of pure water is marked by a black line at 4.65 ppm.

coordinated to Li^+ is not observed in most frames. The most probable CNs are 2 (30%) and 3 (45%), with average ^{1}H chemical shifts of 4.2 and 3.6 ppm, respectively. The average chemical shift for the 9 M LiI solution given in Table 1 is 3.62 ppm, which is slightly lower than the experimental value, reflecting the very weak hydrogen bonding to iodide obtained by the DFT description. It might alternatively be an unintended side effect of the elevated temperature of the simulation. Nevertheless, the experimental trend is reproduced.

Structure and properties of the hydrogen bond network show a consistent weakening of the HBN at 9 M concentration, in agreement with experiment. A global chaotropic effect at the medium concentration of 1 M was not found. Structurally, H-bonding is drastically affected only in the first coordination shell of the ions; the global effect at the 9 M concentration originates from the absence of bulk water. No longer-ranged structural effect is observed in our first-principles calculations.

3.2.3. Dynamics. Dynamic properties are more sensitive to changes in hydrogen bonding than structural properties due to the exponential form of rate laws. We examine hydrogen bonding using the same definition as that used for the topological structure. To investigate the H-bond dynamics, we define a hydrogen bonding autocorrelation function, with a vector function $\zeta(t)$, which has the dimension of the number of possible H-bonds

$$C_{\mathrm{HB}}(t) = \frac{1}{\|\zeta(t_0)\|_1}\langle\zeta(t_0)|\zeta(t)\rangle \quad (1)$$

For all possible hydrogen bonding pairs k, as defined by H-bond donor (proton, lithium cation) and acceptor sites (oxygen, iodide), the hydrogen bond vector component $\zeta(t)_k$ is 1 if a hydrogen bond exists between bonding partners and 0 otherwise. Accordingly, the scalar product in eq 1 represents the number of conserved hydrogen bonds that are present at both the time t_0 and a time t. A hydrogen bonding pair existing only at time t_0 or t will not result in a contribution. The evolution of the autocorrelation function for pure water and both LiI solutions is shown in Figure 9.

We find the decay of the overall C_{HB} to be only slightly influenced by the presence of ions at 1 M concentration. For

dx.doi.org/10.1021/jp4033468 | J. Phys. Chem. B 2013, 117, 9939−9946

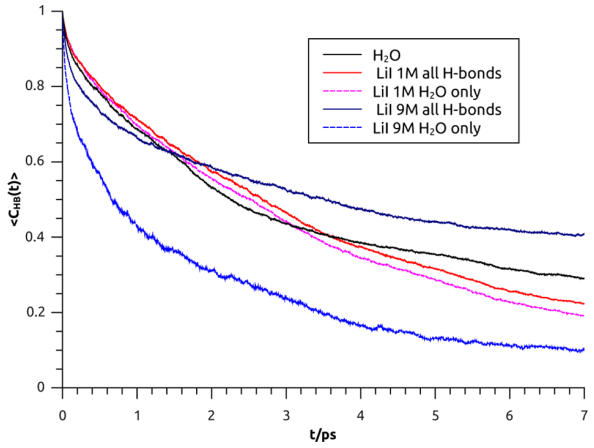

Figure 9. Decay of the hydrogen bond autocorrelation function, averaged over 100 random starting points, where the label "all H-bonds" includes coordination to the ions into the H-bond definition, whereas "H_2O only" includes only H-bonds between H_2O.

this, it is irrelevant whether ions are included in the H-bonding definition or not. However, the tail end of the relaxation is found to be slightly modified, with the LiI solution having a faster tail relaxation. This indicates a small chaotropic effect of the salt. The graph of the HBN present at $t = 0$ and 7 ps reveals that the maximum size connected component in the resulting HBN includes the Li^+ solvation shell and is smaller than the corresponding component in the bulk solution. The broken H-bonds unsurprisingly include the majority of H-bonds to iodide (for an example, see the Supporting Information). From this, we conclude that there is a dynamic structure-breaking effect of the iodide, which might extend over the first solvation shell and is stronger than the corresponding stabilizing effect of the lithium ion, in part due to the larger number of H-bonding partners for I^-. Another indication of this is the decay of C_{HB} for the 9 M solution. It is found to be slower when including Li^+ coordination, which reflects the kinetic stability of the Li^+ oxygen clusters discussed above. When only interwater hydrogen bonding is considered, without including the direct hydrogen bonding to iodide, a drastic weakening is observed. We take this to be further indication of an indirect chaotropic effect of iodide. In order to gather further support for this hypothesis, the decay function is decomposed on the graph spanned by the HBN; see Figure 10.

We define a distance in the HBN graph as the shortest path, that is, smallest number of edges (H-bonds) to connect two vertices (molecules) at t_0 (see Figure 10, left). For example, a water molecule directly coordinated to Li^+ will have graph distance of 1 to Li. If the same molecule is not hydrogen-bonded to iodide but has a H-bonding partner, its distance to iodide is 2 and so on. We directly plot the averaged $C_{HB}(t = 7$ ps) of water layers as a function of this distance to the Li^+ and I^- ions. Figure 10, right shows that at 1 M concentration the HBN is destabilized by iodide up to four H-bonds into the solution, depending on the presence of lithium cations. The competing, kosmoptropic effect on H-bonding is clearly visible only at maximally two H-bonds of distance to the Li^+ ion. As the Li−O coordination is also counted as H-bonds, this merely shows that the polarized water molecules in the Li^+ shell form stronger H-bonds. Inferring from the values of $C_{HB}(t)$ inside of the Li^+ solvation shell, one can see that water around lithium remains immobilized, which explains the slow decay in the case of the 9 M solution. The majority of water molecules are not hydrogen-bonded to either ion, and the maximum population is at (3;3). The picture obtained from dynamics is consistent with NMR chemical shifts as well as the overall structure of the solutions. From the instability of the H-bond network, as well as the fluctuations in the first solvation shell of iodide, we deduce that water in the first solvation shells around iodide is highly mobile due to weakened H-bonding. The water around I^- will easily diffuse into nonhydrophobic interfaces. This effect might play an important role in polymer dissolution and the salting-in effect on proteins.

4. CONCLUSION

We have characterized the structure and picosecond dynamics of the hydrogen bond network of solvated LiI at ambient temperature by means of first-principles molecular dynamics simulations. Our calculations reveal the significant qualitative differences of the network between low (1M) and high (9M) salt concentrations. In particular, we observe the presence of oxygen-bridged lithium ion clusters at 9 M concentration. The solution at this concentration shows characteristic motifs, which

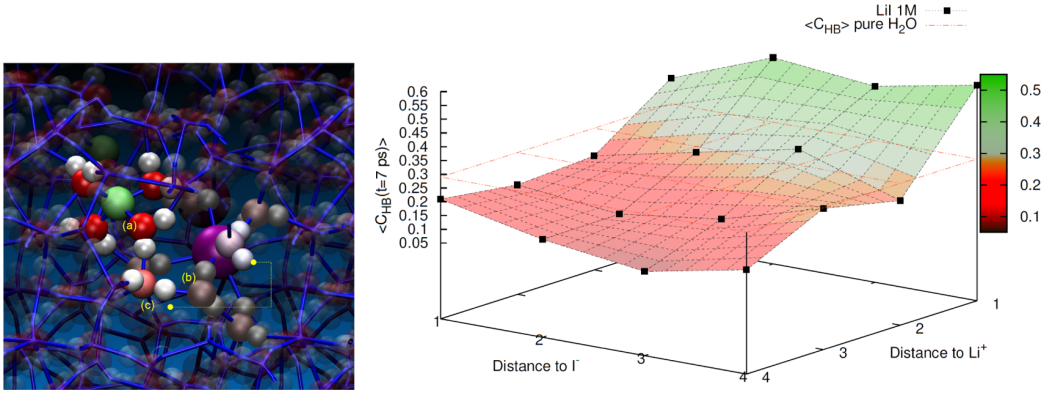

Figure 10. (Left) Visualization of the H-bond network, represented by the blue network of edges and its different components: (a, full color) is the direct Li^+ solvation shell with a minimal distance of $x = 1$ from the edges to lithium, and (b, metallic gray) is the water molecules H-bonded to I^-, with a distance of $y = 1$ from the edges to iodide. In the intermediate range, we find water molecules (c), with the left having a coordinate of (2;2) and the right a coordinate of (2;4), (Right) C_{HB} at $t = 7$ ps of the 1 M LiI solution at minimal distances in hydrogen bonds as present at t_0, averaged over 300 random starting points. The orange grid represents pure water.

dx.doi.org/10.1021/jp4033468 | J. Phys. Chem. B 2013, 117, 9939−9946

are also present in the trihydrate crystal. These motifs are best understood in terms of fused $Li(H_2O)_4$ shells linked by hydrogen bonds to iodide and between themselves. Closer study of the cooperative HBN reveals that iodide ions have only little structural influence but an indirect long-range chaotropic effect on the H-bond dynamics by increasing water mobility in their first shell. In contrast to this, the kosmotropic, that is, the structure-conserving effect of Li^+, does not reach more than one H-bond beyond the first solvation shell. Complementary measurements of a series of NMR shifts of a series of monovalent lithium and sodium halide salts reveal a weakening of hydrogen bonding by heavy halide ions. Our simulation results explain this general trend from coordination shell ion−water interactions. We have validated these findings by first-principles calculations of the ^1H NMR chemical shift lines of LiI at 1 and 9 M, which are in very good agreement with experiment.

■ ASSOCIATED CONTENT

Supporting Information

Experimental details, radial distribution functions of various species, a comparison to published data, H-bond definition and topology, validation of the dynamics, and further details about ion pairing. This material is available free of charge via the Internet at http://pubs.acs.org.

■ AUTHOR INFORMATION

Corresponding Author

*E-mail: daniel.sebastiani@chemie.uni-halle.de.

Notes

The authors declare no competing financial interest.

■ ACKNOWLEDGMENTS

The computing infrastructure was provided by the Northern German Supercomputing Alliance (HLRN) under Grant HLRN/bec00080. We acknowledge financial support from the Deutsche Forschungsgemeinschaft (DFG) under Grant Number INST 271/338-1. Part of this work has been performed under the framework of the Dutch Polymer Institute (DPI, Project Number 685). Y.S.D. and M.R.H. thank DPI for financial support and acknowledge Prof. Sanjay Rastogi and Dr. Robert Graf for continuous support.

■ REFERENCES

(1) Hofmeister, F. *Arch. Exp. Pathol. Pharmakol.* **1888**, *24*, 247−260.
(2) Lo Nostro, P.; Ninham, B. W. *Chem. Rev.* **2012**, *112*, 2286−2322.
(3) Paschek, D.; Ludwig, R. *Angew. Chem.* **2011**, *50*, 352−353.
(4) Rembert, K. B.; Paterová, J.; Heyda, J.; Hilty, C.; Jungwirth, P.; Cremer, P. S. *J. Am. Chem. Soc.* **2012**, *134*, 10039−10046.
(5) Calero, C.; Faraudo, J.; Bastos-González, D. *J. Am. Chem. Soc.* **2011**, *133*, 15025−15035.
(6) Zhang, Y.; Furyk, S.; Bergbreiter, D. E.; Cremer, P. S. *J. Am. Chem. Soc.* **2005**, *127*, 14505−14510.
(7) Lucent, D.; Vishal, V.; Pande, V. S. *Proc. Natl. Acad. Sci. U.S.A.* **2007**, *104*, 10430−10434.
(8) Rasaiah, J. C.; Garde, S.; Hummer, G. *Annu. Rev. Phys. Chem.* **2008**, *59*, 713−740.
(9) Omta, A. W.; Kropman, M. F.; Woutersen, S.; Bakker, H. J. *Science* **2003**, *301*, 347.
(10) Bakker, H. J.; Skinner, J. L. *Chem. Rev.* **2010**, *110*, 1498−1517.
(11) Fecko, C.; Eaves, J.; Loparo, J.; Tokmakoff, A.; Geissler, P. *Science* **2003**, *301*, 1698.
(12) Tielrooij, K. J.; van der Post, S. T.; Hunger, J.; Bonn, M.; Bakker, H. J. J. *J. Phys. Chem. B* **2011**, *115*, 12638−12647.
(13) Hallberg, F.; Furó, I.; Stilbs, P. *J. Am. Chem. Soc.* **2009**, *131*, 13900−13901.
(14) Bühl, M.; Kabrede, H.; Diss, R.; Wipff, G. *J. Am. Chem. Soc.* **2006**, *128*, 6357−6368.
(15) Funkner, S.; Niehues, G.; Schmidt, D. A.; Heyden, M.; Schwaab, G.; Callahan, K. M.; Tobias, D. J.; Havenith, M. *J. Am. Chem. Soc.* **2012**, *134*, 1030−1035.
(16) Enderby, J. E. *Annu. Rev. Phys. Chem.* **1983**, *34*, 155−185.
(17) Neilson, G.; Enderby, J. *J. Phys. Chem.* **1996**, *100*, 1317−1322.
(18) Gurau, M. C.; Lim, S. M.; Castellana, E. T.; Albertorio, F.; Kataoka, S.; Cremer, P. S. *J. Am. Chem. Soc.* **2004**, *126*, 1052−10523.
(19) Hribar, B.; Southall, N. T.; Vlachy, V.; Dill, K. A. *J. Am. Chem. Soc.* **2002**, *124*, 12302−12311.
(20) Zhang, Y.; Cremer, P. S. *Curr. Opin. Chem. Biol.* **2006**, *10*, 658−663.
(21) Zubay, G. *Biochemistry*, 3rd ed.; Brown: Dallas, TX, 1993.
(22) Payumo, A. Y.; Huijon, R. M.; Mansfield, D. D.; Belk, L. M.; Bui, A. K.; Knight, A. E.; Eggers, D. K. *J. Phys. Chem. B* **2011**, *115*, 14784−14788.
(23) Schneider, C.; Shukla, D.; Trout, B. *J. Phys. Chem. B* **2011**, *115*, 7447−7458.
(24) Chen, A. A.; Pappu, R. V. *J. Phys. Chem. B* **2007**, *111*, 11884−11887.
(25) Wernersson, E.; Jungwirth, P. *J. Chem. Theory Comput.* **2010**, *6*, 3233−3240.
(26) Baer, M. D.; Mundy, C. J. *Faraday Discuss.* **2013**, *160*, 89−101.
(27) Heuft, J. M.; Meijer, E. J. *J. Chem. Phys.* **2005**, *123*, 094506.
(28) Ikeda, T.; Boero, M.; Terakura, K. *J. Chem. Phys.* **2007**, *126*, 034501.
(29) Lyubartsev, A. P.; Laasonen, K.; Laaksonen, A. *J. Chem. Phys.* **2001**, *114*, 3120−3126.
(30) Kirchner, B. *Phys. Rep.* **2007**, *1−3*, 1−111.
(31) Raugei, S.; Klein, M. *J. Chem. Phys.* **2002**, *116*, 196−202.
(32) Sillanpaa, A. J.; Simon, C.; Klein, M. L.; Laasonen, K. *J. Phys. Chem. B* **2002**, *106*, 11315−11322.
(33) Simon, C.; Ciccotti, G.; Klein, M. L. *ChemPhysChem* **2007**, *8*, 2072−2076.
(34) Raugei, S. L.; Klein, M. L. *ChemPhysChem* **2004**, *5*, 1569−1576.
(35) Simon, C.; Klein, M. L. *ChemPhysChem* **2005**, *6*, 148−153.
(36) Murakhtina, T.; Heuft, J.; Meijer, J.-E.; Sebastiani, D. *ChemPhysChem* **2006**, *7*, 2578−2584.
(37) Vuilleumier, R.; Sprik, M. *J. Chem. Phys.* **2001**, *115*, 3454−3468.
(38) Tielrooij, K. J.; Garcia-Araez, N.; Bonn, M.; Bakker, H. J. *Science* **2010**, *328*, 1006−1009.
(39) Harings, J. A. W.; Deshmukh, Y. S.; Hansen, M. R.; Graf, R.; Rastogi, S. *Macromolecules* **2012**, *45*, 5789−5797.
(40) Novotny, P.; Sohnel, O. *J. Chem. Eng. Data* **1988**, *33*, 49−55.
(41) Schmidt, J.; VandeVondele, J.; Kuo, I.-F.; Sebastiani, D.; Siepmann, J.; Hutter, J.; Mundy, C. J. *J. Phys. Chem. B* **2009**, *113*, 11959−11964.
(42) Gee, M.; Cox, N.; Jiao, Y.; Bentenitis, N.; Weerasinghe, S.; Smith, P. *J. Chem. Theory Comput.* **2011**, *7*, 1369−1380.
(43) Bentenitis, N.; Cox, N.; Smith, P. *J. Phys. Chem.* **2009**, *113*, 12306−12315.
(44) Kang, M.; Smith, P. *J. Comput. Chem.* **2006**, *27*, 1477−1485.
(45) Berendsen, H. J. C.; Grigera, J. R.; Straatsma, T. P. *J. Phys. Chem.* **1987**, *91*, 6269−6271.
(46) VandeVondele, J.; Hutter, J. *J. Chem. Phys.* **2007**, *127*, 114105.
(47) Hartwigsen, C.; Goedecker, S.; Hutter, J. *Phys. Rev. B* **1998**, *58*, 3641.
(48) Goedecker, S.; Teter, M.; Hutter, J. *Phys. Rev. B* **1996**, *54*, 1703−1710.
(49) Lippert, G.; Hutter, J.; Parrinello, M. *Theor. Chem. Acc.* **1999**, *103*, 124−140.
(50) Lippert, G.; Hutter, J.; Parrinello, M. *Mol. Phys.* **1997**, *92*, 477−487.
(51) VandeVondele, J.; Krack, M.; Mohamed, F.; Parrinello, M.; Chassaing, T.; Hutter, J. *Comput. Phys. Commun.* **2005**, *167*, 103−128.
(52) Grimme, S. *J. Comput. Chem.* **2006**, *27*, 1787−1799.

(53) Becke, A. D. *Phys. Rev. A* **1988**, *38*, 3098.
(54) Lee, C.; Yang, W.; Parr, R. G. *Phys. Rev. B* **1988**, *37*, 785−789.
(55) Bussi, G.; Donadio, D.; Parrinello, M. *J. Chem. Phys.* **2007**, *126*, 014101.
(56) Banyai, D.; Murakhtina, T.; Sebastiani, D. *Magn. Reson. Chem.* **2010**, *48*, S56−S60.
(57) Weber, V.; Iannuzzi, M.; Giani, S.; Hutter, J.; Declerck, R.; Waroquier, M. *J. Chem. Phys.* **2009**, *131*, 014106.
(58) Hutter, J.; et al. *Computer code CP2K*; cp2k.berlios.de (2013).
(59) Guo, X. Y.; Watermann, T.; Keane, S.; Allolio, C.; Sebastiani, D. *Z. Phys. Chem.* **2012**, *226*, 1415−1424.
(60) Tanida, H.; Watanabe, I. *Bull. Chem. Soc. Jpn.* **2000**, *73*, 2747−2752.
(61) Bässmann, C.; Boesl, U.; Yang, D.; Drechsler, G.; Schlag, E. *Int. J. Mass Spectrom. Ion Processes* **1996**, *159*, 153−167.
(62) Lehr, L.; Zanni, M.; Frischkorn, C.; Weinkauf, R.; Neumark, D. *Science* **1999**, *284*, 635.
(63) Pham, V.; Tavernelli, I.; Milne, C.; van der Veen, R.; D'Angelo, P.; Bressler, C.; Chergui, M. *Chem. Phys.* **2010**, *371*, 24−29.
(64) Fulton, J. L.; Schenter, G. K.; Baer, M. D.; Mundy, C. J.; Dang, L. X.; Balasubramanian, M. *J. Phys. Chem. B* **2010**, *114*, 12926−12937.
(65) Strauss, M. Ph.D. Thesis, University of Cincinnati: Cincinnati, OH, 1960.
(66) West, C. *Z. Kristallog.* **1934**, *88*, 198.
(67) Brink, G.; Falk, M. *Can. J. Chem.* **1971**, *49*, 347−351.
(68) Tromp, R.; Neilson, G. W.; Soper, A. K. *J. Phys. Chem.* **1992**, *96*, 8460−8469.
(69) Limbach, H. H. *Magn. Reson. Chem.* **2001**, *39*, 1−2.
(70) Limbach, H.-H.; Tolstoy, P. M.; Perez-Hernandez, N.; Guo, J.; Shenderovich, I. G.; Denisov, G. S. *Isr. J. Chem.* **2009**, *49*, 199−216.
(71) Pfrommer, B.; Mauri, F.; Louie, S. *J. Am. Chem. Soc.* **2000**, *122*, 123−129.

Conclusion and Outlook

The results presented in this work show the versatility of the ab-initio molecular dynamics approach in the investigation of aqueous solvation. From ion specific effects, via confinement effects to femtosecond spectroscopy and nonequilibrium dynamics, this thesis also illustrates the range of phenomena, which are crucially dependent on hydrogen bonding. The sophisticated description of aqueous solvation inherent to the DFT method was exploited to give a quantitative description of the (non)equilibrium solvation dynamics as well as equilibrium structure. Combining the electronic structure with statistical information from molecular dynamics gives access to observables which are not available from either molecular dynamics or electronic structure alone. The most important observables computed in this work are based on density functional perturbation theory, applied to geometries obtained from molecular dynamics trajectories: The time-dependent Stokes shift of MQ in aqueous solution and the ^{1}H NMR chemical shifts of aqueous solutions of LiI and of water confined at a silica interface. A good agreement with experiment for these observables and a range of other properties was found. Furthermore, decompositions were introduced to help interpreting experimental results. These decompositions into local contributions have been applied to

- The time-dependent Stokes shift of MQ - revealing that the reach of the molecular probe goes beyond the first solvation shell and that dipolar interactions are crucial.

- ^{1}H NMR chemical shifts of aqeous solutions of LiI and of water at a silica interface. It was found that the structure of the hydrogen bond network is perturbed strongly only within the first solvation shell.

- The stability of the hydrogen bond network in a solution of LiI - allowing to quantify a competetive effect of Li^+ and I^- on the stability of the hydrogen bonds of waters in between them.

In order to make simulations computationally efficient, some approximations were introduced. The most important one is the treatment of the interactions of the chromophore MQ with H_2O in the S_1 state by the T_1 state. This approach has been carefully validated before application. Another simplification was the representation of an amorphous silicate by a quadratic potential and silicic acid groups. While the spirit of ab-initio molecular dynamics is to gradually let go of this type of system-specific solutions in favor of generality, a good approximation also yields insights into what effects are dominant in a system. It thus facilitates interpretation.

The outlook for this work is determined by the effort to extend and refine the description of the type of systems encountered here. Specifically, the approach to MQ solvation solvation dynamics introduced in this work now is being extended to treat photoacidity and the dynamics of water wires. Ion specific effects are also being investigated for dications, where a description by ab-initio molecular dynamics is expected to be even more crucial than for monocations. The same approach of simulating actual dissolved salts instead of single ions has been adopted, future projects should also include the treatment of peptides. The model confinement introduced in this work has been revised by the author to introduce full surface effects. Currently it is being used to model mixing and demixing phenomena. Another possibility for the future is to combine interactions, such as ion specific effects or local spectrosopy with e.g. the silica confinement. The fact that several of the projects started in this work are being successfully continued and taken further into different directions seems to the author as the best possible conclusion to his thesis.

References

[1] C. Allolio and D. Sebastiani, *Phys. Chem. Chem. Phys.*, 2011, **13**, 16395–16403.

[2] X. Y. Guo, T. Watermann, S. Keane, C. Allolio, and D. Sebastiani, *Z. Phys. Chem.*, 2012, **226**, 1415–1424.

[3] C. Allolio and D. Sebastiani, *Bunsenmagazin*, 2013, **15**, 4–11.

[4] C. Allolio, M. Sajadi, N. P. Ernsting, and D. Sebastiani, *Angew. Chem. Int. Ed. Engl.*, 2013, **52**, 1813–1816.

[5] C. Allolio, N. P. S. Illanes, Y. S. Desmukh, M. R. Hansen, and D. Sebastiani, *J. Phys. Chem. B*, 2013, **117**, 9939–9946.

[6] B. Kirchner, P. di Dio, and J. Hutter in *Multiscale Molecular Methods in Applied Chemistry*, ed. B. Kirchner and J. Vrabec, Vol. 307 of *Top. Curr. Chem.;* Springer, 2012; pp. 109–153.

[7] D. Sebastiani, *Nachr. Chemie*, 2009, **57**, 305.

[8] J. VandeVondele, U. Borštnik, and J. Hutter, *J. Chem. Theory Comput.*, 2012, **8**, 3565–3573.

[9] B. Chen, I. Ivanov, M. L. Klein, and M. Parrinello, *Phys. Rev. Lett.*, 2003, **91**, 215503.

[10] M. Tuckerman, D. Marx, M. L. Klein, and M. Parrinello, *Science*, 1997, **275**, 817–820.

[11] H. J. Bakker and J. L. Skinner, *Chem. Rev.*, 2010, **110**, 1498–1517.

[12] W. Thiel, *Chimia*, 2004, **58**, 276–280.

[13] A. Dreuw and M. Head-Gordon, *Chem. Rev.*, 2005, **105**, 4009–4037.

[14] S. P. Brown and H. W. Spiess, *Chem. Rev.*, 2001, **101**, 4125.

[15] T. Heine, C. Corminboeuf, and G. Seifert, *Chem. Rev.*, 2005, **105**, 3889–3910.

[16] T. Helgaker, M. Jaszunski, and K. Ruud, *Chem. Rev.*, 1999, **99**, 293.

[17] M. Boero, K. Terakura, T. Ikeshoji, C. C. Liew, and M. Parrinello, *Phys. Rev. Lett.*, 2000, **85**, 3245.

[18] M. Benoit, M. Bernasconi, and M. Parrinello, *Phys. Rev. Lett.*, 1996, **76**, 2934–2936.

[19] M. Heyden, J. Sun, S. Funkner, G. Mathias, H. Forbert, M. Havenith, and D. Marx, *Proc. Natl. Acad. Sci. USA*, 2010, **107**, 12068–12073.

[20] R. Iftimie and M. E. Tuckerman, *J. Chem. Phys.*, 2005, **122**, 214508.

[21] J. Schmidt, J. VandeVondele, I.-F. Kuo, D. Sebastiani, J. Siepmann, J. Hutter, and C. J. Mundy, *J. Phys. Chem. B*, 2009, **113**, 11959–11964.

[22] M. Valle, *Z. Kristallogr.*, 2005, **220**, 585–588.

[23] M. Takase, V. Enkelmann, D. Sebastiani, M. Baumgarten, and K. Müllen, *Angew. Chem. Intl. Ed. Engl.*, 2007, **46**, 5524–5527.

[24] D. Sebastiani and M. Parker, *Symmetry*, 2009, **1**, 226–239.

[25] O. Takahashi, Y. Kohno, and M. Nishio, *Chem. Rev.*, 2010, **110**, 6049–6076.

[26] C. Schiffmann and D. Sebastiani, *Phys. Status Solidi B*, 2012, **249**, 368–375.

[27] L. Bernasconi, M. Sprik, and J. Hutter, *J. Chem. Phys.*, 2003, **119**, 12417–12431.

[28] P. R. L. Markwick and N. L. Doltsinis, *J. Chem. Phys.*, 2007, **126**, 175102.

[29] S. Grimm, C. Nonnenberg, and I. Frank, *J. Chem. Phys.*, 2003, **119**, 11574.

[30] M. Odelius, D. Laikov, and J. Hutter, *J. Mol. Struct. THEOCHEM*, 2003, **630**, 163–175.

[31] M. Tuckerman, *Statistical Mechanics - Theory and Molecular Simulation*, Oxford University Press, 2010.

[32] L. Verlet, *Phys. Rev.*, 1967, **159**, 98–103.

[33] W. C. Swope, H. C. Andersen, P. H. Berens, and K. R. Wilson, *J. Chem. Phys.*, 1982, **76**, 637–649.

[34] S. Nosé, *Mol. Phys.*, 1984, **5**, 255.

[35] W. Hoover, *Phys. Rev. A*, 1985, **31**, 1695–1697.

[36] G. J. Martyna, M. L. Klein, and M. E. Tuckerman, *J. Chem. Phys.*, 1992, **97**.

[37] D. Marx and J. Hutter, *Ab Initio Molecular Dynamics: Basic Theory and Advanced Methods*, Cambridge University Press, 2009.

[38] R. J. Bartlett and J. F. Stanton, 2007; Vol. 5 of *Reviews in Computational Chemistry*, pp. 65–169.

[39] P. Knowles, M. Schütz, and H.-J. Werner Vol. 3 of *NIC Series;* John von Neumann Institute for Computing Jülich, 2000; pp. 97–179.

[40] A. J. Cohen, P. Mori-Sánchez, and W. Yang, *Chem. Rev.*, 2012, **112**, 289–320.

[41] T. Ziegler, *Chem. Rev.*, 1991, **91**, 651–667.

[42] F. Nogueira, M. A. L. Marques, and C. Fiolhais, *A primer in density functional theory*, Vol. 620 of *Lecture Notes in Physics*, Springer, 2003.

[43] K. Burke and L. O. Wagner, *Int. J. Quantum Chem.*, 2013, **113**, 96–101.

[44] R. G. Parr and W. Yang, *Density functional theory of atoms and molecules*, Oxford Science Publications, 1989.

[45] J. P. Perdew in *Electronic Structure of Solids*, ed. P. Ziesche and H. Eschrig; Akademie Verlag, Berlin, 1991; p. 11.

[46] A. Szabo and N. S. Ostlund, *Modern Quantum Chemistry*, Dover Publications Inc., 1996.

[47] E. Engel and R. M. Dreizler, *Density Functional Theory: An Advanced Course*, Springer, 2011.

[48] P. Hohenberg and W. Kohn, *Phys. Rev.*, 1964, **136**, B864.

[49] M. Levy, *Proc. Natl. Acad. Sci. USA*, 1979, **76**, 6062.

[50] E. Lieb, *Int. J. Quantum Chem.*, 1983, **24**, 243–277.

[51] W. Kohn and L. J. Sham, *Phys. Rev.*, 1965, **140**, A1133.

[52] L. H. Thomas, *Math. Proc. Cambridge*, 1927, **23**, 542–548.

[53] E. Fermi, *Rend. Accad. Naz. Lincei*, 1927, **6**, 602–607.

[54] P. A. M. Dirac, *Math. Proc. Cambridge*, 1930, **26**, 376–385.

[55] D. M. Ceperley and B. J. Alder, *Phys. Rev. Lett.*, 1980, **45**, 566.

[56] S. H. Vosko, L. Wilk, and M. Nusair, *Can. J. Phys.*, 1980, **58**, 1200.

[57] W. Koch and M. C. Holthausen, *A Chemist's Guide to Density Functional Theory*, Wiley-VCH, 2001.

[58] D. C. Langreth and M. J. Mehl, *Phys. Rev. B*, 1983, **28**, 1809–1834.

[59] A. D. Becke, *Phys. Rev. A*, 1988, **38**, 3098.

[60] C. Lee, W. Yang, and R. G. Parr, *Phys. Rev. B*, 1988, **37**, 785–789.

[61] J. Perdew, *Phys. Rev. B*, 1986, **33**, 8822–8824.

[62] J. Perdew, S. Kurth, A. Zupan, and P. Blaha, *Phys. Rev. Lett.*, 1999, **82**, 2544–2547.

[63] A. D. Becke, *J. Chem. Phys.*, 1993, **98**, 5648–5652.

[64] J. Perdew and A. Zunger, *Phys. Rev. B*, 1981, **23**, 5048.

[65] S. Grimme, *J. Comp. Chem.*, 2006, **27**, 1787–1799.

[66] A. von Lilienfeld-Toal, I. Tavernelli, U. Rothlisberger, and D. Sebastiani, *Phys. Rev. Lett.*, 2004, **93**, 153004.

[67] F. Bloch, *Z. Phys.*, 1929, **52**, 555–600.

[68] H. Hellmann, *J. Chem. Phys.*, 1935, **3**, 61.

[69] H. Hellmann, *J. Chem. Phys.*, 1936, **4**, 324.

[70] R. M. Martin, *Electronic Structure: Basic Theory and Practical Methods*, Cambridge University Press, 2004.

[71] G. B. Bachelet, D. R. Hamann, and M. Schluter, *Phys. Rev. B*, 1982, **26**, 4199.

[72] L. Kleinman and D. M. Bylander, *Phys. Rev. Lett.*, 1982, **48**, 1425.

[73] S. Goedecker, M. Teter, and J. Hutter, *Phys. Rev. B*, 1996, **54**, 1703.

[74] D. R. Hamann, M. Schluter, and C. Chiang, *Phys. Rev. Lett.*, 1979, **43**, 1494.

[75] N. Troullier and J. L. Martins, *Phys. Rev. B*, 1991, **43**, 1993–2006.

[76] G. Lippert, J. Hutter, and M. Parrinello, *Mol. Phys.*, 1997, **92**, 477–487.

[77] M. Feyereisen, G. Fitzgerald, and A. Komornicki, *Chem. Phys. Lett.*, 1993, **208**, 359 – 363.

[78] P. E. Blöchl, *Phys. Rev. B*, 1994, **50**, 17953–17979.

[79] G. Lippert, J. Hutter, and M. Parrinello, *Theor. Chem. Acc.*, 1999, **103**, 124–140.

[80] J. Hutter et al., Computer code CP2K.

[81] P. Pulay, *Chem. Phys. Lett.*, 1980, **73**, 393–398.

[82] T. Watermann, A. Scherrer, and D. Sebastiani, in *Many-Electron Approaches in Physics, Chemistry and Mathematics: A Multidisciplinary View*, ed. L. Delle Site, in press.

[83] X. Gonze, *Phys. Rev. A*, 1995, **52**, 1096–1114.

[84] A. Putrino, D. Sebastiani, and M. Parrinello, *J. Chem. Phys.*, 2000, **113**, 7102–7109.

[85] S. Baroni, S. de Gironcoli, A. del Corso, and P. Giannozzi, *Rev. Mod. Phys.*, 2001, **73**, 515.

[86] D. Sebastiani and M. Parrinello, *J. Phys. Chem. A*, 2001, **105**, 1951–1958.

[87] R. Ditchfield, *J. Chem. Phys.*, 1972, **56**, 5688.

[88] W. Kutzelnigg, *Isr. J. Chem.*, 1980, **19**, 193.

[89] T. A. Keith and R. F. W. Bader, *Chem. Phys. Lett.*, 1993, **210**, 223.

[90] V. Weber, M. Iannuzzi, S. Giani, J. Hutter, R. Declerck, and M. Waroquier, *J. Chem. Phys.*, 2009, **131**, 014106.

[91] T. A. Keith and R. W. F. Bader, *Chem. Phys. Lett.*, 1992, **194**, 1.

[92] E. K. U. Gross and N. T. Maitra In ed. M. A. L. Marques, N. T. Maitra, F. M. S. Nogueira, E. K. U. Gross, and A. Rubio, *Fundamentals of Time-Dependent Functional Theory*, Vol. 837 of *Lecture Notes in Physics*, p. 53, 2012.

[93] R. Gaudoin and K. Burke, *Phys. Rev. Lett.*, 2004, **93**, 173001.

[94] E. Runge and E. K. U. Gross, *Phys. Rev. Lett.*, 1984, **52**, 997–1000.

[95] M. Marques, C. Ullrich, F. Nogueira, A. Rubio, K. Burke, and E. Gross, *Time-Dependent Density Functional Theory*, Vol. 706 of *Lecture Notes in Physics*, Springer, 2006.

[96] M. Petersilka, U. J. Gossmann, and E. K. U. Gross, *Phys. Rev. Lett.*, 1996, **76**, 1212–1215.

[97] M. E. Casida, C. Jamorski, K. C. Casida, and D. R. Salahub, *J. Chem. Phys.*, 1998, **108**, 4439–4449.

[98] F. Cordova, L. J. Doriol, A. Ipatov, M. E. Casida, C. Filippi, and A. Vela, *J. Chem. Phys.*, 2007, **127**, 164111.

[99] R. Car and M. Parrinello, *Phys. Rev. Lett.*, 1985, **55**, 2471.

[100] J. VandeVondele and J. Hutter, *J. Chem. Phys.*, 2003, **118**, 4365–4369.

[101] J. Hutter, M. Parrinello, and S. Vogel, *J. Chem. Phys.*, 1994, **101**, 3862–3865.

[102] T. D. Kühne, M. Krack, F. R. Mohamed, and M. Parrinello, *Phys. Rev. Lett.*, 2007, **98**, 066401.

[103] J. Kolafa, *J. Chem. Phys.*, 2005, **122**, 164105.

[104] J. Hutter, John Wiley & Sons, Inc., 2012; Vol. 2 of *Wiley Interdisciplinary Reviews: Computational Molecular Science*, pp. 604–612.

[105] D. Eisenberg and W. Kauzmann, *The Structure and Properties of Water*, Clarendon, 1969.

[106] J. C. Rasaiah, S. Garde, and G. Hummer, *Annu. Rev. Phys. Chem.*, 2008, **59**, 713–740.

[107] N. E. Levinger, *Science*, 2002, **298**, 1722–1723.

[108] M. Fayer and N. E. Levinger, *Annu. Rev. Anal. Chem.*, 2010, **3**, 89–107.

[109] K. M. Ravikumar and W. Hwang, *J. Am. Chem. Soc.*, 2011, **133**, 11766–11773.

[110] P. Ball, *Chem. Rev.*, 2008, **108**, 74–108.

[111] P. Lo Nostro and B. W. Ninham, *Chem. Rev.*, 2012, **112**, 2286–2322.

[112] R. N. Butler and A. G. Coyne, *Chem. Rev.*, 2010, **110**, 6302–6337.

[113] M. L. Horng, J. A. Gardecki, A. Papazyan, and M. Maroncelli, *J. Phys. Chem.*, 1995, **99**, 17311.

[114] J. L. Pérez-Lustres, M. Mosquera, T. Senyushkina, S. A. Kovalenko, W. Flasche, and N. P. Ernsting, *Angew. Chem. Int. Ed. Engl.*, 2005, **44**, 5635–5639.

[115] A. Nitzan, *Chemical Dynamics in Condensed Phases: Relaxation, Transfer, and Reactions in Condensed Molecular Systems*, Oxford University Press, 2006.

[116] C.-P. Hsu, X. Song, and R. A. Marcus, *J. Phys. Chem. B*, 1997, **101**, 2546–2551.

[117] J. L. Pérez-Lustres, F. Rodriguez-Prieto, M. Mosquera, T. A. Senyushkina, N. P. Ernsting, and S. A. Kovalenko, *J. Am. Chem. Soc.*, 2007, **129**, 5408–5418.

[118] M. Sajadi, Y. Ajaj, I. Ioffe, H. Weingärtner, and N. P. Ernsting, *Angew. Chem. Int. Ed. Engl.*, 2010, **49**, 454–457.

[119] M. Sajadi, M. Weinberger, H.-A. Wagenknecht, and N. P. Ernsting, *Phys. Chem. Chem. Phys.*, 2011, **13**, 17768–17774.

[120] R. Jimenez, G. R. Fleming, P. V. Kumar, and M. Maroncelli, *Nature*, 1994, **369**, 471–473.

[121] R. Bukowski, K. Szalewicz, G. C. Groenenboom, and A. van der Avoird, *Science*, 2007, **315**, 1249–1252.

[122] P. L. Geissler, C. Dellago, D. Chandler, J. Hutter, and M. Parrinello, *Science*, 2001, **291**, 2121–2124.

[123] A. A. Chen and R. V. Pappu, *J. Phys. Chem. B*, 2007, **111**, 11884–11887.

[124] E. Wernersson and P. Jungwirth, *J. Chem. Theory Comput.*, 2010, **6**, 3233–3240.

[125] S. Funkner, G. Niehues, D. A. Schmidt, M. Heyden, G. Schwaab, K. M. Callahan, D. J. Tobias, and M. Havenith, *J. Am. Chem. Soc.*, 2012, **134**, 1030–1035.

[126] K. J. Tielrooij, N. Garcia-Araez, M. Bonn, and H. J. Bakker, *Science*, 2010, **328**, 1006–9.

[127] C. Fecko, J. Eaves, J. Loparo, A. Tokmakoff, and P. Geissler, *Science*, 2003, **301**, 1698.

[128] A. W. Omta, M. F. Kropman, S. Woutersen, and H. J. Bakker, *Science*, 2003, **301**, 347.

[129] P. Gallo, M. Rovere, and S.-H. Chen, *J. Phys.: Condens. Matter*, 2010, **22**, 284102.

[130] M. Vogel, *Eur. Phys. J. Spec. Top.*, 2010, **189**, 47–64.

[131] P. H. Poole, F. Sciortino, U. Essmann, and E. H. Stanley, *Nature*, 1992, **360**, 324–328.

[132] Y. Zhang, A. Faraone, W. A. Kamitakahara, K.-H. Liu, C.-Y. Mou, J. B. Leo, S. Chang, and S.-H. Chen, *Proc. Natl. Acad. Sci. USA*, 2011, **108**, 12206–12211.

[133] P. Gallo, M. Rovere, and S.-H. Chen, *J. Phys.: Condens. Matter*, 2012, **24**, 064109.

[134] J. Schmidt, J. Hutter, H. W. Spiess, and D. Sebastiani, *ChemPhysChem*, 2008, **9**, 2313–2316.

[135] Y. J. Lee, T. Murakhtina, D. Sebastiani, and H. Spiess, *J. Am. Chem. Soc.*, 2007, **129**, 12406–12407.

[136] Y. J. Lee, B. Bingöl, T. Murakhtina, D. Sebastiani, W. Meyer, G. Wegner, and H. Spiess, *J. Phys. Chem. B*, 2007, **111**, 9711–9721.

[137] A. Rapp, I. Schnell, D. Sebastiani, S. P. Brown, V. Percec, and H. W. Spiess, *J. Am. Chem. Soc.*, 2003, **125**, 13284–13297.

[138] D. Sebastiani, *Mod. Phys. Lett. B*, 2003, **17**, 1301–1319.

[139] M. Strauss *X-ray diffraction studies of some aqueous solutions of lithium iodide* PhD thesis, University of Cincinnati, 1960.

[140] C. West, *Zeitschr. Kristallog*, 1934, **88**, 198.

Declaration

I herewith declare that I have produced this paper without the prohibited assistance of third parties and without making use of aids other than those specified; notions taken over directly or indirectly from other sources have been identified as such. This paper has not previously been presented in identical or similar form to any other German or foreign examination board.

The thesis work was conducted under the supervision of Prof. Dr. Daniel Sebastiani at FU Berlin and MLU Halle-Wittenberg.

Halle, Saale - 20.12.2013 Christoph Allolio

CHRISTOPH ALLOLIO

PERSONAL INFORMATION

born in Germany (Köln), August 1, 1983

email christoph.allolio@chemie.uni-halle.de

phone +49 (0) 3455525854 · (M) +49 (0) 176 24278709

EDUCATION

2010-present **FU Berlin/MLU Halle-Wittenberg**

PhD Thesis

Topic: Ab-initio Molecular Dynamics of Hydrogen Bonded Systems
Advisor: Prof. Daniel Sebastiani · chair of *theoretical chemistry*

2007-2009 **Technische Universität, Dresden**

Diplomchemiker (eq. M. Sc.)

Final grade: 1.3 (A) · Thesis: Chelating Biscarbene Complexes as Catalysts of the Heck-reaction: Mechanistic Study and Synthesis
Thesis grade: 1.2 (A) · Advisor: Prof. Thomas Strassner · chair of *physical organic chemistry* · Courses in biochemistry, computational chemistry, inorganic chemistry.

2005-2007 **Ecole Européenne de Chimie de Polymères & Matériaux, Strasbourg**

Diplôme d'Ingiénieur

Grade: 15.89/20 (A) · Specialized in *organic chemistry*, ranking speciality: 3rd of 48, final year: 6th of 83. Visited courses in general chemistry, chemical engineering, quantum theory, statistical physics.

2003-2005 **Philipps Universität, Marburg**

Vordiplom der Chemie

Grade: 1.6 (A-) · Undergraduate studies in chemistry with introduction to chemistry, physics. Obtained a C++ certificate from the computer science department.

WORK EXPERIENCE

09/2010 – **Research Assistant, FU Berlin MLU Halle-Wittenberg**

MLU Halle-Wittenberg/FU Berlin

Ab-initio molecular dynamics of solvated molecules (e.g. fluorescent probes, dissociated ions) and water in confinement, work on grant applications · TA in physical chemistry in 2013, computational physics in 2010, 2011 · Assistance of master- and bachelor theses, DAAD RISE internship.

03/2009– 09/2010 **Research Assistant, TU Dresden**

TU Dresden

Theoretical investigation of reaction mechanisms, forcefield parametrization, linux cluster · TA in computational chemistry

INTERNSHIPS

07/2007- 09/2007 **Research Chemist, GlaxoSmithKline**

GlaxoSmithKline

Internship in the analgesics department. Synthesis of candidate compounds.

08/2006 **Intern, Vogel Medien AG — Würzburg**

Vogel Medien AG

Internship at Process magazine, development of the Groab database for chemical industry construction projects (www.groab.de)

PUBLICATIONS

7. C. Allolio, N. Illanes, Y. S. Deshmukh, M.R. Hansen, D. Sebastiani
Hydrogen Bonding in Highly Concentrated Salt Solutions: The Case of LiI., *J. Phys. Chem. B* 117, 34, 9939-9946, **2013**

6. C. Allolio, M. Sajadi, N. P. Ernsting, D. Sebastiani
An ab-initio microscope: water H-bonding and reorientational contributions to the femtosecond time-dependent fluorescence shift of a Reichardt-type dye, *Angew. Chem. Int. Ed.* 52, 6, 1813-1816, **2013**

5. C. Allolio, D. Sebastiani
From solvation to spectroscopy - electronic structure calculations as virtual experiments, *Bunsen Magazin* 15, 1, 4-11, **2013**

4. X. Guo, T. Watermann, S. Keane, C. Allolio , D. Sebastiani
First Principles Calculations of NMR chemical shifts of Liquid Water at an Amorphous Silica Interface *Z. Phys. Chem.* 226, 1415-1424, **2012**

3. D. Munz, C. Allolio, K. Döring, A. Poethig, T. Doert, H. Lang, T. Strassner
Methoxyaryl Substituted Palladium bis-NHC Complexes - Synthesis and Electronic Effects, *Inorg. Chim. Acta.* 392, 204-210, **2012**

2. C. Allolio and D. Sebastiani, Approaches to the solvation of the molecular probe N-methyl-6-quinolone in its excited state, *Phys. Chem. Chem. Phys.* 13, 16395- 16403, **2011**

1. T. Schulz, S. Ahrens, D. Meyer, C. Allolio, A. Peritz, T. Strassner, Electronic Effects of para-Substitution on the Melting Points of TAAILs, *Chem. Asian J.* 6, 863-867, **2011**

COMPUTER / PROGRAMMING SKILLS

Basic PERL, PYTHON, JAVA

Advanced C++, C, PHP

Software CP2K, CPMD, Gaussian, Orca, Gromacs, LaTeX, Linux shells, Office, Windows API, Qt, etc.

OTHER INFORMATION

Scholarships 2008 · Bourse Villes Jumelles Strasbourg

2005-2007 · Double Diploma with scholarship of DFH-UFA

Talks 2013 · Bunsentagung
2012 · CECAM Photochemistry Workshop Lyon
2009-2013 · Posters on several conferences, e.g. DPG, CPMD 2011 Barcelona, STC 2012, ISTCP 8 Budapest, CPMD 2013 Leipzig

Language Skills

GERMAN	·	native language
ENGLISH	·	fluent (speaking, reading, writing)
FRENCH	·	intermediate (speaking, reading, writing)

Hobbies Theater · Guitar · Chess · Cooking

December 19, 2013